

Department of Electrical and Computer Engineering

**Accurate location of high impedance and temporary  
faults in radial distribution networks using distributed  
travelling wave observers**

**Ali Tashakkori Jahromi**

This thesis is presented for the Degree of  
Doctor of Philosophy  
of  
Curtin University

**December 2020**

## **Declaration**

To the best of my knowledge and belief, this thesis contains no material previously published by any other person except where due acknowledgment has been made. This thesis contains no material which has been accepted for the award of any other degree or diploma in any university.

Signature: Ali Tashakkori Jahromi

Date: 24/12/2020

# Acknowledgments

I would like to express my sincere gratitude to my supervisor Dr Ahmed Abu-Siada; this thesis would not have been completed without his help, support and patience. I am deeply indebted to my supervisor Professor Syed Islam for giving me the opportunity to begin my PhD studies. I have been indescribably enlightened by his constant support, gentle guidance and warm encouragement. I also greatly appreciate Professor Peter Wolfs for his inspiring guidance and instruction in the development of this study. It is hard to find the words to express my appreciation for their support and guidance.

I gratefully acknowledge the scholarship and funding received for my studies from Western Power (network corporation) and the Australian Research Council's Linkage Program.

I would like to thank my beloved family, Mona and Kai, for their patience and unconditional support during my studies. Last but not least, I express my heartfelt gratitude to my dear parents, Ghodratollah and Mahnaz, for their enormous support and encouragement.

# Abstract

In recent years, the costs of wild bushfires caused by distribution networks have grown. This has increased the need for reliable and accurate high impedance and temporary fault location methods. Current fault location technologies are limited in heavily branched networks and cannot locate high impedance or temporary faults. Technology that could locate high impedance and temporary faults may enable faults to be cleared and reduce the risk of fires. For example, conductor clashes could be eliminated before the fire season begins each year.

This thesis addresses a novel method for fault location in radial distribution networks and provides a new vision for the optimal deployment of synchronised voltage travelling wave (TW) observers in distribution networks. The proposed method can locate high impedance and temporary faults.

A novel methodology for fault location in radial distribution networks is introduced. It uses the voltage TWs that propagate from fault locations throughout distribution networks. The algorithm is based on the TW arrival time recorded at multiple locations within a distribution network. This thesis then investigates the effects of power system components on the propagation of voltage TWs. A transformer high-frequency model was developed based on frequency response analysis measurements to study distribution transformers. The delay effect of transformers is demonstrated by theory and laboratory tests. A new method to eliminate the transformer's effect on the accuracy of the fault location algorithm is presented. Finally, the optimal deployment strategy for TW observers is proposed to maximise the length of feeders; these are allocated as observable and locatable for a given number of observers.

# Statement of contribution to publications

This thesis includes the technical materials and the results of the experiments that have been published in international journals and conferences. These publications are listed below.

- **International Peer Review Journal Publications.**

1. Tashakkori, P. J. Wolfs, S. Islam and A. Abu-Siada, "Fault Location on Radial Distribution Networks via Distributed Synchronized Traveling Wave Detectors," in IEEE Transactions on Power Delivery, vol. 35, no. 3, pp. 1553-1562, June 2020, doi: 10.1109/TPWRD.2019.2948174.
2. A. Tashakkori, A. Abu-Siada, P. J. Wolfs, S. Islam, " Optimal Placement of Synchronized Voltage Travelling Wave Sensors in a Radial Distribution Network", Accepted by IEEE Access on April 2021.

- *The main contribution of the candidate to journal papers 1-2:*

Generating the concept and design, acquiring the data and inputs, data manipulation and statistical analysis, modelling and generating of results, interpretation and discussion, manuscripts preparation, the final approval of the manuscripts and replying to reviewer comments.

- *The main contribution of the co-authors to the journal paper 1-2:*

Reviewing of results, verifying a contribution and novelty, discussion, assessing the quality of the experimental results and reviewing and rectifying the manuscript.

Name	Author: Ali Tashakkori Jahromi	Supervisor: Ahmed Abu-Siada
Signature		

- **Conference Publications.**

3. T. Jahromi, P. Wolfs and S. Islam, "Travelling wave fault location in rural radial distribution networks to reduce wildfire risk," 2015 Australasian Universities Power Engineering Conference (AUPEC), Wollongong, NSW, 2015, pp. 1-6, doi: 10.1109/AUPEC.2015.7324833.
4. A. T. Jahromi, P. Wolfs and S. Islam, "A travelling wave detector based fault location device and data recorder for medium voltage distribution systems," 2016 Australasian Universities Power Engineering Conference (AUPEC), Brisbane, QLD, 2016, pp. 1-5, doi: 10.1109/AUPEC.2016.7749307.

- *The main contribution of the candidate to journal papers 3-4:*

Generating the concept and design, acquiring the data and inputs, data manipulation and statistical analysis, modelling and generating of results, interpretation and discussion, manuscripts preparation, the final approval of the manuscripts and replying to reviewer comments.

- *The main contribution of the co-authors to the journal paper 1-2:*

Reviewing of results, verifying a contribution and novelty, discussion, assessing the quality of the experimental results and reviewing and rectifying the manuscript.

Name	Author: Ali Tashakkori Jahromi	Supervisor: Ahmed Abu-Siada
Signature		

# Contents

<b>Acknowledgments .....</b>	<b>III</b>
<b>Abstract.....</b>	<b>IV</b>
<b>Statement of contribution to publications.....</b>	<b>V</b>
<b>List of Figures.....</b>	<b>XI</b>
<b>List of Tables .....</b>	<b>XVI</b>
<b>List of Abbreviations .....</b>	<b>XVII</b>
<b>Chapter 1 Introduction.....</b>	<b>1</b>
1.1. Motivations for the study .....	2
1.2. Contributions of the thesis .....	3
1.2.1. Travelling wave-based fault location for radial distribution networks .....	4
1.2.2. Optimal sensor deployment for fault location.....	4
1.2.3. Development of a simplified transformer model .....	4
1.2.4. Eliminating the effects of power system components.....	5
1.2.5. Travelling wave observer prototype.....	5
<b>Chapter 2 Fault location in distribution networks.....</b>	<b>6</b>
2.1. Introduction.....	6
2.2. Division of fault location techniques .....	7
2.2.1. Power-frequency-based methods .....	7
2.2.2. High-frequency travelling wave arrival time method .....	9
2.2.3. Knowledge-based methods .....	11
2.3. High impedance and temporary fault location in distribution networks.....	11
2.4. Key features of the proposed fault location algorithm.....	15
2.5. Summary .....	15
<b>Chapter 3 Travelling waves in distribution networks .....</b>	<b>17</b>

3.1. Introduction.....	17
3.2. The travelling wave theory .....	18
3.2.1. Telegrapher’s Equations.....	20
3.2.2. The lossless line .....	22
3.3. Reflection and refraction of travelling waves .....	23
3.3.1. Reflection and refraction coefficients at line bifurcations .....	25
3.3.2. Reflection and refraction coefficients at the junctions of power lines and capacitors.....	26
3.3.3. Reflection and refraction coefficients at the junctions of power lines and inductance .....	27
3.4. The behaviour of travelling waves at junctions .....	28
3.4.1. Model 1: unit step function travelling wave .....	29
3.4.2. Model 2: constant rising ramp travelling wave.....	29
3.5. Summary .....	32
<b>Chapter 4 Parameter determination for modelling transformer behaviour under transient conditions.....</b>	<b>33</b>
4.1. Introduction.....	33
4.2. Travelling wave behaviour at the transformer terminals .....	35
4.2.1. Admittance matrix terminal model .....	36
4.2.2. Experimental measurements .....	39
4.3. Creation of the model.....	42
4.4. Simplified transformer model .....	47
4.4.1. Transformer load’s effects .....	49
4.4.2. Verification of model .....	51
4.4.3. Distribution transformer models .....	52
4.5. Summary .....	57
<b>Chapter 5 High impedance faults .....</b>	<b>59</b>
5.1. Introduction.....	59
5.2. High impedance fault models .....	61
5.3. Suggested high impedance fault model .....	64
5.4. Summary .....	66
<b>Chapter 6 Travelling wave arrival time detection techniques .....</b>	<b>67</b>
6.1. Introduction.....	67
6.2. Signal processing techniques .....	68



6.2.1. Differences and approximate derivatives.....	68
6.2.2. Discrete wavelet transformed spectral energy .....	69
6.2.3. Boundary wavelet transform .....	71
6.3. Dealing with multiphase lines.....	72
6.3.1. Clarke’s transformation.....	72
6.3.2. Park’s transformation .....	73
6.4. Detection criteria.....	74
6.5. Thresholding .....	75
6.6. Arrival time detection procedures.....	76
6.7. Summary .....	79
<b>Chapter 7 Travelling wave-based fault location for radial distribution networks 80</b>	
7.1. Introduction.....	80
7.2. Proposed fault location method .....	81
7.3. Monte Carlo uncertainty analysis .....	83
7.4. Summary .....	90
<b>Chapter 8 Accuracy enhancements for the proposed fault location algorithm 91</b>	
8.1. Introduction.....	91
8.2. The effects of parasitic capacitance .....	92
8.3. The effects of a transformer .....	93
8.4. Validation and experimental setup.....	94
8.5. Travelling time considering the transformer’s effects .....	99
8.6. Simulation results.....	99
8.7. Summary .....	101
<b>Chapter 9 Optimal deployment of synchronised voltage travelling wave sensors 102</b>	
9.1. Introduction.....	102
9.1.1. Fault observability analysis.....	103
9.1.2. Fault locatability analysis.....	105
9.2. Travelling wave detector placement model .....	106
9.2.1. Optimisation objectives.....	106
9.2.2. Constraint handling .....	107
9.2.3. Optimisation model.....	107

9.3. Simulation results and analysis .....	107
9.3.1. Test network.....	107
9.3.2. Optimisation parameter setting .....	108
9.4. Summary .....	111
<b>Chapter 10 Travelling wave detector hardware .....</b>	<b>112</b>
10.1.Introduction.....	112
10.2.Prototype hardware .....	113
10.2.1. External antenna and front-end filters.....	114
10.3.High voltage laboratory testing.....	120
10.4.Field trial .....	121
10.5.Summary .....	126
<b>Chapter 11 Concluding remarks and further study.....</b>	<b>127</b>
11.1.Concluding remarks .....	127
11.1.1. Travelling wave-based high impedance fault location in radial distribution networks .....	127
11.1.2. Enhancement of the proposed fault location algorithm's accuracy .....	128
11.1.3. Optimal development of synchronised voltage travelling wave sensors	128
11.2.Further study .....	128
11.2.1. Investigate novel online travelling wave arrival detection methods .....	128
11.2.2. Investigate novel transient classification algorithms .....	129
11.2.3. Field trial and simulation of various fault types.....	129
11.2.4. Hardware improvements .....	129
11.2.5. Fault location on medium direct current distribution network.....	129
11.2.6. Fault location using re-closure generated travelling wave.....	130
11.2.7. Compensating for line length error due to ambient temperature changes	
	130
<b>References .....</b>	<b>131</b>
<b>Appendix A Frequency-dependent branch device .....</b>	<b>149</b>
<b>Appendix B List of Publications .....</b>	<b>154</b>

# List of Figures

Figure 1.1. Aerial view of the burned ruins of some houses in Marysville, north of Melbourne, during 2009 [6].	2
Figure 2.1. Block diagram of the travelling wave fault location method.	9
Figure 2.2. Single-line diagram of the SVY 517 distribution network in Mundaring, West Australia, owned by Western Power.	12
Figure 3.1. The origin of power system electrical transients and most common associated wavelength ranges.	18
Figure 3.2. The voltage source for (a) a two-wire transmission line; and (b) a ‘lumpy’ representation of a two-wire line [58].	19
Figure 3.3. A small segment of a transmission line (Heaviside’s model).	21
Figure 3.4. The junctions between lines with characteristic impedance $Z_A$ , $Z_B$ and $Z_C$ .	24
Figure 3.5. The junction between lines with the characteristic impedance of $Z_A$ and $Z_B$ .	26
Figure 3.6. The junction of the line and capacitor.	27
Figure 3.7. The junction of a line and the inductance.	28
Figure 4.1. A typical transformer response to the sudden suppression of a direct current, showing a power transformer (left) a [58] (right) Single-phase 25 kVA distribution transformer (right).	35
Figure 4.2. A simplified winding cross-section through turns.	35
Figure 4.3. A simplified representation of a detailed equivalent network [58].	36
Figure 4.4. The voltage and current of a two-port network.	37
Figure 4.5. The voltage and current of a two-port network when one port is a short circuit.	37
Figure 4.6. A single-line diagram of a multi-terminal $\pi$ -equivalent circuit [62].	38
Figure 4.7. The generic structure of a resistor, inductor, and capacitor branch.	39
Figure 4.8. Connection diagrams for measuring: (a) the diagonal elements of $Y_s$ ; and (b) the off-diagonal elements of $Y_s$ .	40
Figure 4.9. A comprehensive model of a transformer.	42
Figure 4.10. A 25 kVA single-wire earth-return transformer and its nameplate information.	43

Figure 4.11. A 25 kVA single-wire earth-return transformer measured voltage transform function showing: (a) the magnitude; and (b) the phase angle.....	44
Figure 4.12. Comparison of the frequency characteristics of a 25 kVA single-wire earth-return transformer high voltage terminal self-admittance (Y11) between the measured and resistor, inductor and capacitor fitted equivalent, showing: (a) the admittance magnitude; and (b) the admittance phase angle.....	45
Figure 4.13. Comparison in the transmission impedance admittance (Y12) frequency characteristics of a 25 kVA single-wire earth-return transformer between the measured and resistor, inductor and capacitor fitted equivalent showing: (a) the admittance magnitude; and (b) the admittance phase angle.....	45
Figure 4.14. Comparison in the low voltage terminal self-admittance (Y22) frequency characteristics of a 25 kVA single-wire earth-return transformer between the measured and RLC fitted equivalent, showing: (a) the admittance magnitude; and (b) the admittance phase angle.....	46
Figure 4.15. A circuit model of a 25 kVA single-wire earth-return transformer.....	46
Figure 4.16. Comparison between the simulation model and the measured voltage transfer function of a 25 kVA single-wire earth-return transformer.....	47
Figure 4.17. The high voltage winding admittance magnitude of a 12.7/0.250 kV, 25 kVA single-phase single-wire earth-return transformer. ....	47
Figure 4.18. A simplified model of a single-phase transformer. ....	48
Figure 4.19. A typical admittance versus frequency graph of distribution transformers.....	49
Figure 4.20. The frequency response of a single-phase 2 kVA, 250/120 V transformer under different load conditions.....	50
Figure 4.21. The simple model used to simulate the sweep frequency response analyser test.....	51
Figure 4.22. Frequency response results from the simulation and measurements under (a) the short circuit; (b) 100% of the nominal load condition; and (c) 50% of the nominal load condition.....	53
Figure 4.23. The simulation model was verified: (a) the setup of the laboratory; (b) the schematic diagram for the test; and (c) the simulation circuit. ....	54
Figure 4.24. Comparisons of the simulation and laboratory test results: (a) the recorded and simulated voltage across the termination impedance; and (b) close-up of the rising edge.....	55

Figure 4.25. Results from the measured sweep frequency response analysis of common distribution transformers in the Western Australian network: (a) 25 kVA, 12.7/0.240 kV single-wire earth-return transformer; and (b) 25 kVA 19/0.240 kV single-wire earth-return transformer. ....	56
Figure 4.26. A simplified model of a three-phase transformer in a delta configuration. ....	57
Figure 5.1. Contact events showing: (a) a down conductor ejecting molten particles; and (b) a vegetation-initiated arc [68]. ....	60
Figure 5.2. Diagrams showing: (a) the Emanuel model; and (b) the modified Emanuel model. ....	61
Figure 5.3. A high impedance fault model using multiple Emanuel arc models [76]. ....	62
Figure 5.4. A high impedance fault model based on arc features [78]. ....	62
Figure 5.5. A high impedance fault model considering the ignition instants [80]. ....	63
Figure 5.6. The high impedance fault model proposed by Sharat et al. [74]. ....	64
Figure 6.1. The structure of the one-level discrete wavelet transform. ....	70
Figure 6.2. The structure of the one-level maximal overlap discrete wavelet transform. ....	71
Figure 6.3. The computational stages of a travelling wave arrival time-stamp. ....	77
Figure 6.4. The expected waveform from each step, showing: (a) the samples phase voltages; (b) the calculated aerial mode voltages; and (c) the wavelet energy coefficient. ....	78
Figure 7.1. The propagation delay: $T_l$ , $T_l, n_1$ and $T_l, n_2$ . ....	81
Figure 7.2. A diagram of the Monte Carlo uncertainty simulation. ....	86
Figure 7.3. A modified single-line diagram of the IEEE 34-bus test distribution network. ....	87
Figure 7.4. Histograms representing the probability distribution function for the fault location: (a) line numbers ( $L_f$ ); and (b) the location of the fault at the $L_f$ with respect to the line's origin as a percentage of the line's length ( $\alpha$ ). ....	88
Figure 7.5. The output probability distribution of the first scenario. ....	89
Figure 7.6. The output probability distribution of the second and third scenarios. ...	89
Figure 8.1. Simplified models for the: (a) single-phase or single-wire earth-return transformer; and (b) three-phase transformer. ....	93
Figure 8.2. A schematic diagram of the first experimental setup. ....	95

Figure 8.3. The 25 kVA single-wire earth-return transformer that was used for the test, showing: (a) the transformer; and (b) the transformer's nameplate. ....	96
Figure 8.4. The first recorded waveforms at the cable end. ....	97
Figure 8.5. The experimental setup, demonstrating the multiple transformers' cumulative error. ....	98
Figure 8.6. Graphs showing: (a) the voltages measured across the termination impedance; and (b) the wavelet energy coefficient for the recorded voltage. ....	98
Figure 8.7. A modified single-line diagram of the IEEE 34-bus test distribution network. ....	100
Figure 9.1. A single-line diagram of a typical radial network. ....	104
Figure 9.2. The optimum placement of travelling wave observers for $\beta = 0.5$ . The red lines are observable and locatable. The travelling wave observers were placed at the buses shown in red. ....	109
Figure 9.3. The optimum placement of travelling wave observers for $\beta = 0.3$ . The red lines are observable and locatable. The travelling wave observers were placed at the buses shown in red. ....	110
Figure 9.4. The cost per length of fault-detectable and observable lines versus the number of observers. ....	110
Figure 10.1. A diagram of the hardware block. ....	114
Figure 10.2. The placement of antennas and the phase conductor configurations on a typical 22 kV distribution pole. ....	115
Figure 10.3. The lumped capacitors between the overhead conductors, antennas, and ground (A, B and C are the phase conductors, and D, E and F are the antennas). ..	116
Figure 10.4. An input channel equivalent circuit. ....	116
Figure 10.5. An equivalent electrical circuit model between phase A and the antennas. ....	117
Figure 10.6. A simplified equivalent circuit between phase A and the antennas. ...	117
Figure 10.7. The bode diagram of $HADj\omega$ ( $ZAD = 1$ pF). ....	118
Figure 10.8. An overview of the overall system. ....	119
Figure 10.9. The equipment under test at the Western Power high voltage laboratory. ....	120
Figure 10.10. The recorded voltages when: (a) the A conductor was energised; (b) the B conductor was energised; and (c) the C conductor was energised. ....	122

Figure 10.11. The antenna voltages when the 22 kV three-phase was connected to the overhead conductors..... 123

Figure 10.12. The travelling wave detector prototype installed on the medium voltage distribution network. .... 123

Figure 10.13. The captured waveforms during the field trial, showing: (a) a possible line-to-line fault; (b) a high-frequency component that might have been caused by an arc; and (c) a lower-frequency transient caused by the two-phase load or capacitor switching. .... 125

# List of Tables

Table 2.1. Summary of the limitations and capabilities of fault location methods....	14
Table 3.1. The behaviour of step voltage travelling waves for different junction types .....	30
Table 3.2. The behaviour of ramp voltage travelling waves for different junction types .....	31
Table 4.1. Transformer modelling guidelines .....	34
Table 4.2. Model parameters for a 2 kVA, 250/120 VAC transformer in different loading conditions .....	51
Table 4.3. Simplified model parameter of single-phase single-wire earth-return transformers.....	52
Table 7.1. IEEE 34-bus distribution line lengths and propagation times.....	87
Table 7.2. The Monte Carlo simulation parameters.....	87
Table 7.3. Summary of the results for all scenarios .....	90
Table 8.1. Transformer models' parameters .....	100
Table 8.2. Travelling wave arrival times for the fault on line 027–028 .....	101
Table 8.3. Fault location results .....	101
Table 9.1. Parameters of binary particle swarm optimisation.....	108



# List of Abbreviations

AC	Alternating current
AI	Artificial intelligence
BPSO	Binary particle swarm optimisation
CAIDI	Customer Average Interruption Duration Index
CVT	Capacitive voltage transformer
DC	Direct current
DWT	Discrete wavelet transform
EMTP	Electromagnetic transient program
FDBFIT	Frequency-dependent branch-fitting
GPS	Global positioning system
HFTWAT	High-frequency travelling wave arrival time
HIF	High impedance fault
HV	High voltage
KBM	Knowledge-based method
MODWT	Maximal overlap discrete wavelet transform
MV	Medium voltage
PFB	Power-frequency-based
RLC	Resistor, inductor and capacitor
SAIDI	System Average Interruption Duration Index
SFRA	Sweep frequency response analyser
SWER	Single-wire earth returns
TW	Travelling wave
VBRC	Victorian Bushfires Royal Commission
VNA	Vector network analyser
VTF	Voltage transfer function

# Chapter 1

## Introduction

Modern society's dependency on electricity has increased demands for highly reliable power systems. Power system continuity indices, such as the System Average Interruption Duration Index (SAIDI) and the Customer Average Interruption Duration Index (CAIDI), summarise the number and duration of interruptions in distribution systems. These indices are often difficult to maintain within the prescribed limits [1]. Despite the importance of fault location techniques for maintaining the SAIDI and CAIDI in distribution networks, the reliability and accuracy of current technologies are limited in medium voltage (MV) distribution networks. In distribution systems, faults are often located by physically inspecting the faulted feeders. A maintenance crew commonly inspects and locates the faulted section, following notification by the system operator [2]. This conventional fault location method cannot easily locate momentary, temporary and high impedance faults (HIFs). Undetected developing faults reduce a system's reliability and threaten human safety.

Arcs and heat produced by a fault can ignite nearby combustible material. Rural MV overhead distribution lines have ignited several bushfires and wildfires that have caused significant property damage and loss of life. Downed conductors, vegetation contacting conductors, sparks from clashing conductors and apparatus failures are the common sources of ignition. In 2019, equipment owned by the Pacific Gas and Electric Company was found to have started the Camp Fire in Paradise California, which killed 85 people. The Pacific Gas and Electric Company has been blamed for 1,500 fires since 2014 and recently filed for bankruptcy [3].

During February 2009, a series of bushfires in Victoria, Australia, burned 4,500 km<sup>2</sup> of land, which resulted in 3,500 destroyed structures, 173 deaths and

A\$4 billion in property damage [4]. Figure 1.1 shows an aerial view of a burned area north of Melbourne. The Victorian Bushfires Royal Commission (VBRC) investigated the wildfire and determined that electrical overhead distribution faults caused five of the 11 bushfires. One fault, at Kilmore East, resulted in 119 deaths [5].

Modern and reliable fault location technologies are needed for MV distribution networks. These are required especially for locating temporary and developing faults, which often remain undetected by conventional protection systems, and might cause bushfires and threaten human safety in remote rural networks.



**Figure 1.1. Aerial view of the burned ruins of some houses in Marysville, north of Melbourne, during 2009 [6].**

### **1.1. Motivations for the study**

A power system fault will cause unnecessary damage to networks and private assets if it is not detected or cleared shortly after its inception. The effect of such faults may escalate through the operation of secondary protection and will pose risks to network personnel and the general public. Although protection schemes for distribution systems are well designed for the detection and isolation of solid permanent faults, reliable fault location remains a key challenge, particularly in rural distribution networks.

The growth of network penetration in rural and sparsely populated areas has revealed the importance of corrective measures for counteracting the consequences of

aging infrastructure and the underlying challenges in reliably analysing the increasing number of disturbance events. Therefore, the development of resilient, reliable, and efficient fault location schemes constitutes an integral part of reliable distribution protection systems in aging distribution networks.

Arcing faults caused by conductors clashing at the mid-span will generate showers of sparks and molten metal or HIFs, with currents in the range of 10 A, which may result from conductors falling onto dry soils or contacting vegetation. The West Australian Office of Energy Safety has documented many instances where clashing has ignited grass or stubble and caused significant fires (e.g., the Toodyay fire) [7]. Instances of fire ignition are well-documented, such as in the Parkerville fire, which was caused by a tree contact [8]. The existing fault location schemes in distribution networks are unable to locate intermittent faults and HIFs, such as conductors clashing or vegetation contact.

Rural power networks often date to the 1970s and 1980s. Historically, these utilities used simple wooden pole lines with steel and aluminium conductors protected by fuses. Rural distribution networks are not profitable, and many systems need major capital investments that cannot be justified on economic grounds alone. The VBRC found that the inability to identify and repair aging assets prone to failure was a latent cause of five fires due to electrical faults during 7 February 2009 [4]. Western Power currently faces a A\$2 billion backlog of maintenance work for its aging population of 600,000 wooden poles. Several of the VBRC recommendations specifically related to the improvement of network asset maintenance procedures. Technology that could locate intermittent faults and HIFs would reduce the risk of catastrophic failures and wildfires. Widespread and cost-efficient deployment of synchronised measurements on feeders, would allow the development of distributed travelling wave (TW) observers that can time-stamp TW arrival times with reasonable accuracy and precisely locate any faults.

## **1.2. Contributions of the thesis**

The main aim of this thesis is to contribute into wildfire reduction by proposing a fault location scheme that can identify the location of high impedance and intermittent faults. The secondary aim of this research is to assess the performance of the developed prototype on field trials. The main contribution of the research is

elaborated below. Detailed description of each part will be given within the body of the thesis.

### ***1.2.1. Travelling wave-based fault location for radial distribution networks***

A novel analytical and computational approach to fault location in radial distribution networks has been developed. The proposed method uses multiple TW observers throughout a distribution network. Multiple measurements lead to over-determined systems of equations that can be solved to estimate a fault's location. This method directly estimates the locations of faults by measuring TW arrival times at the locations of synchronised observers. The procedure captures the phase voltage waveforms to determine the arrival times of fault-initiated TWs and uses these to identify the location of faults. The method is applicable to intermittent faults and HIFs. The main advantages of this method are:

- the distributed observers increase the chance of detecting weak TWs initiated by HIFs
- it only utilises the initial TW arrival times, not the subsequent reflection to locate the intermittent faults
- it uses voltage TWs instead of current TWs to locate HIFs.

### ***1.2.2. Optimal sensor deployment for fault location***

The problem of economically and practically placing TW observers is considered. For a network to be completely observable, at least one observer per branch or spur is required. From an economic point of view, this is an unlikely solution. A reasonable number of relatively low-cost voltage TW observers with a global positioning system (GPS) time-synchronisation and radio communication can be deployed to detect and time-stamp TW arrivals at several points for practical purposes. The proposed method mathematically identifies a 'locatability' factor for each line that can be used to place the TW observers optimally.

### ***1.2.3. Development of a simplified transformer model***

A junction with an overhead line and transformer is common within power distribution systems. A comprehensive high-frequency transformer model is complex; for detailed modelling, every turn needs to be represented, including all the series and shunt capacitors and the self and mutual inductors. However, a simplified transformer

model is appropriate for studying wave reflections and refractions at the transformer junctions. A simplified distribution transformer model was developed as part of this research. The model was based on a series of frequency response analysis measurements.

#### ***1.2.4. Eliminating the effects of power system components***

The results of this study indicate that shunt-connected customer transformers introduce errors due to changes in TW propagation times. The effects of distribution transformers are investigated mathematically and demonstrated through laboratory tests. Compensation methods are proposed to reduce the effect of transformer delays and increase the accuracy of the proposed fault location methods.

#### ***1.2.5. Travelling wave observer prototype***

This thesis was funded through the Australian Research Council Linkage Program. A prototype TW observer was developed as part of this research. Professor Peter Wolfs designed the hardware at Central Queensland University. This work was conducted in parallel to the research but is outside the scope of this thesis. The development of the detection algorithm was the topic of this thesis. The prototype was tested in a distribution network owned by Western Power, and some initial results are presented in this thesis.

# Chapter 2

## Fault location in distribution networks

### 2.1. Introduction

Faults on distribution lines can be caused by insulation breakdowns, lightning strikes, conductors clashing, overloading, equipment failures, vegetation overgrowth and animal contact. One task that affects the time to restore power and remove faults is finding the fault's location. If the location of a fault is estimated accurately, the line will be restored more efficiently. Faults can be temporary or permanent. Temporary faults are the most common on distribution networks. Accurate temporary fault location can assist with identifying weak areas on feeders so that they can be remediated before significant permanent faults occur. In a distribution system, faults are often located using a physical inspection technique along the section of a faulted feeder. Following notification by the system operator, a maintenance crew are commonly dispatched to the affected area to inspect the faulted section and locate the fault [2]. Therefore, finding the cause of temporary faults commonly relies on human observations before personnel can report the exact location of the fault. Fault location can be a significant challenge in low-density residential or rural areas. Therefore, there has been significant research conducted to improve fault location methods in power distribution networks [9].

Most of the commonly used protection relays, digital fault recorders and monitoring devices used in modern distribution networks are microprocessor-based. They offer increased computational capabilities and high-speed communications. Further, with the decreasing cost of high-speed microprocessors and GPS, the

application of synchronised measurements is rapidly becoming widespread across the power grids [10]. These offer easy integration of the modern fault location function with a reasonable cost to improve the success of locating faults.

## **2.2. Division of fault location techniques**

Fault location methods fall into two main categories: outage mapping and precise location [11]. In the outage mapping method, a fault area is identified based on the fault current indicators, smart device status (e.g., reclosers), customer calls and geographic information systems [12]. In rural and low-density residential areas, long sections of lines need to be inspected. This fault location method can be time consuming and inefficient. The precise location method typically involves more advanced technologies, which determine fault locations by processing the voltage and current waveform parameters. Precise fault location can be classified into the following main categories:

- power-frequency-based methods
- high-frequency TW arrival time method
- knowledge-based methods.

### **2.2.1. Power-frequency-based methods**

Power-frequency-based (PFB) methods focus on a line's frequency-dependent quantities of power frequencies. These methods are also called impedance-based fault locators. They determine a fault's location by using the measured short circuit loop impedance at the fundamental frequency. The phase-to-ground voltages and phase currents are required. Impedance relays generally use separate algorithms to locate phase-to-phase and phase-to-ground faults. The source's zero sequence impedance is required to estimate a phase-to-ground fault's location. Measured voltages and currents are used to determine the short circuit loop impedance at a power frequency. Fault locations can be estimated by measuring the line impedance per unit length. The accuracy of this method relies on the following parameters:

- the presence of branches in radial feeder topology, which can produce several valid possible fault locations for a given fault impedance
- the effect of load currents and fault resistance, including the effect of an unbalanced load
- inaccurate fault type classifications



- the influence of zero sequence effects
- uncertainty about the line parameters, including the zero sequence
- the presence of shunt reactors and capacitors
- any current and voltage transformer errors
- the transients in voltages and currents during faults [13].

Different fault location methods may be implemented depending on the available data. Various PFB methods have been proposed for radial distribution networks [14-24]. These studies have contributed to the accuracy of PFB methods by addressing specific challenges. Multiple feeder bifurcations and laterals introduce a unique challenge in radial distribution networks. Fault locations in radial distribution networks cannot be uniquely identified based on the impedance parameters because multiple possibilities of fault locations with similar loop impedance are possible within a branched network. The PFB methods introduced in the literature for radial distribution networks required additional tools to specify and rank any possible fault locations. Jun et al. used a fault diagnosis algorithm to specify the possible fault locations by considering the recloser operating patterns and identify the actual fault locations [15]. Salim et al. [16], [18] used the methods introduced by Oliveira et al. [25] to identify faulty sections by analysing high-frequency components. Brahma proposed a scheme that relies on additional information from digital fault recorders [17]. This scheme assumed that voltage and current measurements were available at the source and connection point of each distribution generator. Yanfeng and Guzmán proposed a combination of reactance calculations with other intelligent field device information to determine possible fault locations [20]. Dashti and Sadeh determined faulty sections by analysing the operation of protective equipment (i.e., fuses, fault indicators and reclosers) [21]. In later research, Dashti and Sadeh used a frequency spectrum analysis to estimate faulty sections before locating the actual fault based on the fault loop impedance [22]. In another study, methods were proposed that used multiple current measurements at different nodes to locate the faults [23].

PFB methods rely on fault classification algorithms to identify the correct type of fault before calculating the fault loop impedance. The performance of fault classification algorithms will directly affect the accuracy of the fault location algorithms. These methods rely on successful fault detection by other protective measures before attempting to locate any faults. Further, HIFs that have current

magnitudes less than the load current cannot be located and detected by impedance with PFB methods.

### 2.2.2. High-frequency travelling wave arrival time method

Sudden changes in the state variable of transmission lines launch a TW in both directions. The TW appears as a high-frequency component that is travelling along the transmission line. The propagation speed is a function of the line parameters per unit length. The time that a high-frequency component takes to travel from a fault's location to the protective devices in a network could reveal information regarding the fault's location.

The high-frequency TW arrival time method (HFTWAT) is based on the travelling time-related information. It is a mature technology at the power transmission scale. The Bonneville Power Administration has used HFTWAT since the 1950s [26]. Four types of fault locators have been developed by the Bonneville Power Administration (see Figure 2.1) [27].

In the Type A fault locator, a TW travels to the end of a line and is reflected towards the fault, in turn, the TW reflects from the fault's location. A fault's location is estimated from the time difference between the initial and reflected wave's arrival

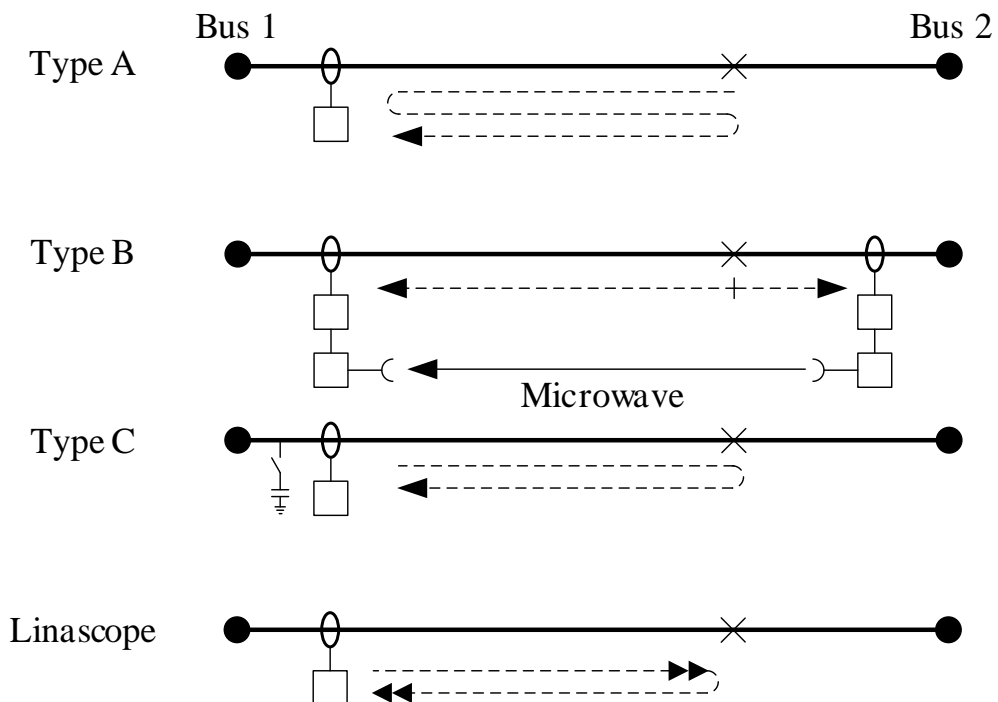


**Figure 2.1. Block diagram of the travelling wave fault location method.**

at the end of the line [28, 29]. The Type B fault locator estimates a fault's location using only the initial wave's arrival at the two ends of the line. The Type B method requires a fixed-latency communication channel to trigger a timer at one end from another. Alternatively, a synchronised clock at both ends is required [29-32]. With the reducing costs, GPS synchronised clocks are becoming widespread for TW fault location purposes. In the Type C fault locator, the initial TW initiates a sequence of fault location operations. Once the initial TW is detected, and after a controlled time delay, a surge is applied to the faulted conductor from a charged capacitor. The time difference between the charge application and reflected surge reveals the fault's location. The Type D (Linascop) method does not use the fault generated TW. Instead, a periodic sequence of pulses is applied to the transmission line, and the resulting echoes are used to estimate a fault's location [33-35].

Generally, the performance of these fault locators is based on the characteristics of TWs. However, the key challenges differ for each method. In the Type A method, the reflected wave appears in a fault locator system, which makes it difficult to interpret any faults close to the midpoint [27]. The Type B locator only uses the initial surge arrives at the two ends of a line. This avoids the issues posed by multiple reflections. However, the method requires a communication channel and synchronised clocks or timers. For Type C, the surge is applied to the phase conductors that are involved in the fault. Therefore, the faulted phase must be identified before the fault's location pulse is applied. In both Type C and Type D, surge or pulse coupling is required to inject a pulse into the line. The propagation speed of TWs is important for each method because the time measurements must be translated into units of distance.

Since the Bonneville Power Administration introduced these methods, much research has focused on the application of the HFTWAT in densely branched distribution networks [9, 36-39]. TW attenuate rapidly in distribution networks due to the many laterals and feeder bifurcations. However, HFTWAT methods have received a great deal of attention because they can provide fault estimates that are insensitive to fault inception angles, fault types, fault resistances and pre-fault system conditions [40]. HFTWAT methods can locate both high impedance and temporary faults.

Some studies have proposed fault location algorithms for distribution networks based on the Type A method [37-39]. In a field trial, Borghetti et al. demonstrated the location of faults along a feeder using a Type A method in a simple distribution

network with eight nodes [39]. Robson et al. introduced a Type B method to locate faults using a time-stamped recording from each branch [9]. Shi et al. used the time difference between the reclosing instant and the arrival instant of a reflected TW to calculate the fault distance [36]. It should be noted, must temporary faults disappear after tripping. Therefore, this method can only be used for locating permanent faults.

### **2.2.3. Knowledge-based methods**

A knowledge-based method (KBM) is an artificial intelligence (AI) procedure that uses expert human knowledge to support decision-making. The new pattern-recognition, or decision-making, algorithms can improve the accuracy of fault locating in distribution networks. The reducing costs of technology, recent developments in AI and increasing importance of fault detection and location have enabled many studies to use AI for detecting, predicting, and locating faults in distribution networks. A fault's location-related data is extracted from the voltage, current or both and entered into the KBM to estimate the fault's location.

Various approaches have been published that describe the application of a KBM to locate faults in distribution lines [41-45]. Some studies employed the fundamental frequency components (voltage and current) derived from waveforms [41, 42]. These methods consider the influence of load conditions and complexity of distribution networks. Some KBM fault locators use the high-frequency components of fault-originating waveforms [43-45].

The extracted features are commonly those of the outputs from the PFB or HFTWAT methods. For example, an artificial neural network was used in one study to replace humans and interpret the frequency spectrum of recorded fault-induced transients [45]. This study combined the methods introduced by Borghetti et al. [39] with AI systems. In large distribution systems, the transient recorded signals are not easy to interpret due to reflections from the many tee connections used in a network [46].

## **2.3. High impedance and temporary fault location in distribution networks**

High impedance and temporary fault location in radial distribution networks have been the subject of interest for utility companies and researchers. In rural radial networks, physical fault locating poses a significant challenge due to the length and accessibility of these networks; conductor size changes on the feeders; multiple feeder

taps and laterals; inaccurate system data and dynamic configurations; insufficient energy for establishing clean arcs; evolving fault characteristics and magnitudes; and effect of fault impedance and pre-fault power flows [13]. For example, Figure 2.2 provides a single-line diagram of a rural distribution network owned by Western Power. The furthest point is 37 km from the substation, and the total length is more than 300 km, including the laterals.

PFB methods for fault location in distribution networks require additional means to distinguish whether the fault is on the lateral or the feeder [47].

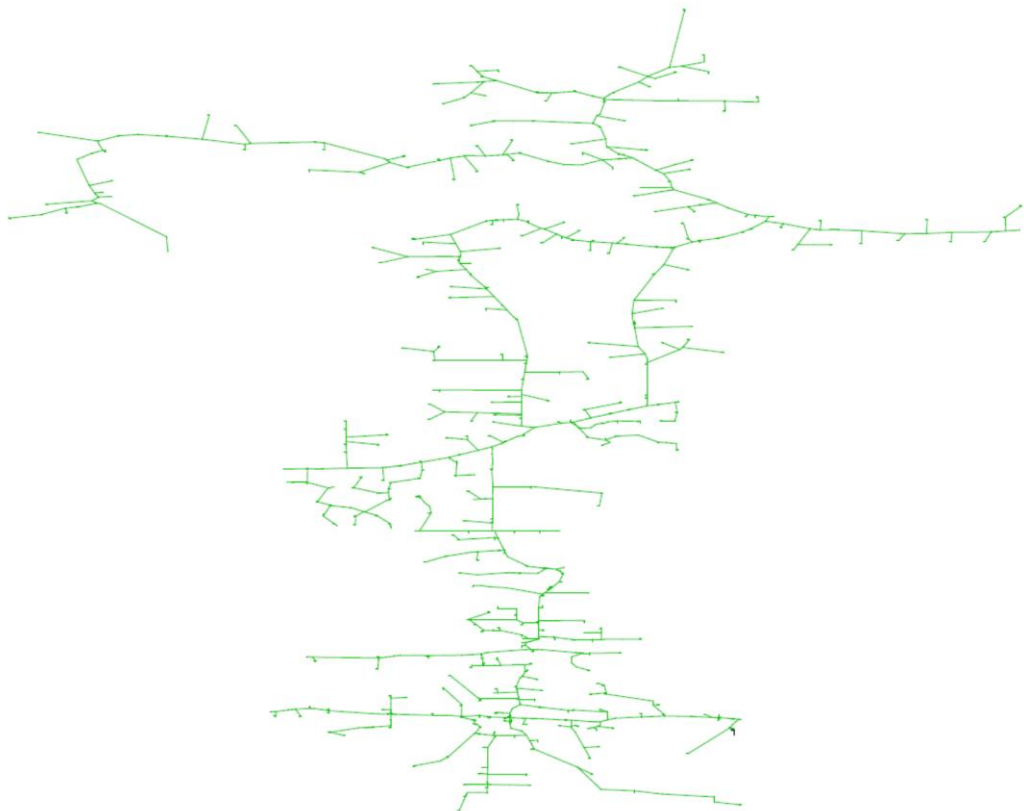


**Figure 2.2. Single-line diagram of the SVY 517 distribution network in Mundaring, West Australia, owned by Western Power.**

The impedance of a fault loop is calculated when the fault reaches a steady state. Therefore, this approach cannot locate momentary faults, such as conductor clashing.

General PFB fault location methods assume that all feeder sections have the same impedance characteristics [20]. This introduces significant errors for large distribution networks with many branches and line sections with different conductor types and cross-arm configurations. A detailed distribution network model is required

to reduce errors. The effects of fault impedance are significant in PFB methods. Therefore, it is impractical to use for locating HIFs.

The HFTWAT method calculates fault distances by using the time that a fault-induced high-frequency component takes to travel through a transmission media. This method has high precision, high reliability and is unaffected by the pre-fault state of feeders and fault impedance [10, 28, 48-51]. Borghetti et al. proposed a Type A single-ended method for distribution networks using a simple test feeder with only one tee junction [39]. In densely branched distribution networks, the TWs will attenuate rapidly. Therefore, it is difficult to detect the initial arrival time at the observer point and the subsequent reflection of TWs.

The Type B method, which has been commercialised for transmission lines, cannot identify fault locations on radial distribution networks with many laterals and bifurcations. More than two TW detectors are required to estimate fault locations in distribution networks. Sudden state variable changes of any type in a distribution network will generate a TW (e.g., load switching, conductor clashing, fuse opening, teleswitch operation, capacitor bank switching or lightning). Therefore, transient classification methods are required to distinguish between fault-related transients and other transients.

Consider the multi-terminal transmission shown in Figure 2.3; the arrival time difference between observers A and C ( $\Delta t_{AC}$ ) for a fault between points B and D is equal to:

$$\Delta t_{AC} = (t_{BA} + t_{XB}) - (t_{BC} + t_{XB}) = t_{BA} - t_{BC} \quad (2.1)$$

Where:

- $t_{BA}$  is an incident wave's travelling time between node B and A
- $t_{XB}$  is an incident wave's travelling time from a fault at point X to node B
- $t_{BC}$  is an incident wave's travelling time from node B to C

The  $\Delta t_{AB}$  is not the function of the fault location between nodes B and D. The fault location is not uniquely observable between nodes B and D.

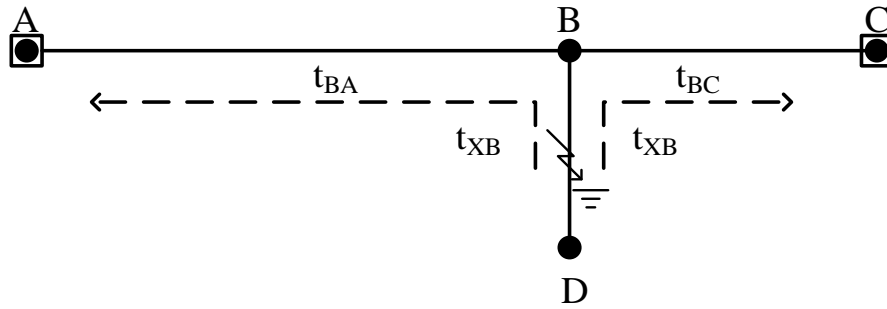


**Figure 2.3. A three-terminal system, where the travelling wave observer is installed at nodes A and C.**

AI and the KBM have received a good deal of attention among researchers for solving power system challenges. The ability of KBM has been demonstrated with HIF detection and transient classification. The main challenge of using AI for fault location in distribution networks is the available data set for training the algorithms. Table 2.1 compares the ability of the common fault location methods to locate faults in radial distribution networks.

**Table 2.1. Summary of the limitations and capabilities of fault location methods**

<b>Limitation/capability</b>	<b>Power-frequency-based methods</b>	<b>High-frequency travelling wave arrival time methods</b>	<b>Knowledge-based methods</b>
<b>Fault impedance</b>	Introduces significant error	No effect	Depends on algorithm
<b>HIF location</b>	Cannot locate the fault	Depends on algorithm	Depends on algorithm
<b>Pre-fault load current</b>	Introduces significant error	Not affected	Depends on algorithm
<b>Error due to line parameter</b>	Introduces significant error	Introduces error	Introduces error
<b>Momentary fault</b>	Cannot locate the fault	Can locate the fault	Depends on algorithm
<b>High-branched network</b>	Requires additional information	Requires multiple measurements	Depends on algorithm
<b>Cost</b>	Low	Relatively high	Depends on algorithm
<b>Implementation challenge</b>	Detailed network model	Multiple synchronised measurements	Created the training set
<b>Tested in distribution</b>	Currently in use with limitations	Tested on a simple feeder	Tested on a simple feeder

#### **2.4. Key features of the proposed fault location algorithm**

The proposed method offers a computationally efficient method of fault location based on information from the voltage TW time-stamps for radial distribution networks. The proposed method is in contrast to the approach used by Robson et al. [9], where a network must split to smaller sections to achieve the required accuracy, which increases the complexity and computational burden. Further, Salehi and Namdari successfully used a similar approach for a radial branched network [52]. First, they identified the fault lateral, and then, the exact location of the fault was estimated from the measured arrival time (using a method proposed by Abur and Magnago [53]). The proposed method here directly estimates the fault location from the measured arrival time. The complexity of the problem is not a function of the desired accuracy.

Each high impedance arc current cycle contains two dominant arc ignitions and two dominant arc extinctions that generate TWs [54]. Although the magnitude of HIF current TWs is weak and hard to detect, voltage TWs are noticeable. By monitoring the voltage, even a HIF can be located. The algorithm uses only the initial incident wave arrival time. Unlike the methods introduced in other studies [28, 38, 39, 55, 56], consecutive reflection from faults is not required to determine a fault's location. Therefore, even short intermittent faults can be located.

In extensive and complex distribution networks, TWs attenuate rapidly due to multiple discontinuities along the feeder and even first incident waves will be challenging to detect. The proposed method mathematically defines the fault locatability terms. It can be used for optimal placement of the observers at radial distribution networks when considering the observability and attenuation of TWs. The methods estimate and compensate fault location errors by considering the number and characteristics of any transformers between the voltage TW detectors and the fault's location.

#### **2.5. Summary**

Fault location approaches are divided into two main categories, outage mapping and precise location. This chapter presents background information regarding the precise fault location problem in distribution networks. Precise fault location methods are roughly divided into three main categories. Advantage and disadvantage of each category are discussed with emphasis on their ability to detect temporary and



high impedance faults. The potential benefits of using distributed travelling wave detector for fault location are also explained.

# Chapter 3

## Travelling waves in distribution networks

### 3.1. Introduction

Distribution networks are exposed to many sudden changes in circuit conditions that lead to transients. For instance, standard distribution network operating events (e.g., switching of line sections) may initiate electrical transients. Similarly, an abnormal condition, such as an electrical fault, can produce a voltage and current transient. Electrical circuits consist of three basic elements: resistors, inductors, and capacitors (RLCs). These elements are in distributed quantities for power lines, and each small part of the circuit possesses its share. Commonly, power lines are represented using lumped or concentrated RLC parameters. In many cases, the lumped element representation is adequate. However, this is not the case when the length of a power line are longer compared to the wavelength of the electromagnetic waves that pass through power line.

Power system transient studies can involve a frequency range from the direct current (DC) to above 50 MHz. At frequencies above the normal power frequency, transients usually involve electromagnetic phenomena (e.g., lightning). Below the normal power frequency, they have electromechanical origins (e.g., rotor angle instabilities [57]). Figure 3.1 summarises the various origins of such transients and their most common wavelength ranges.

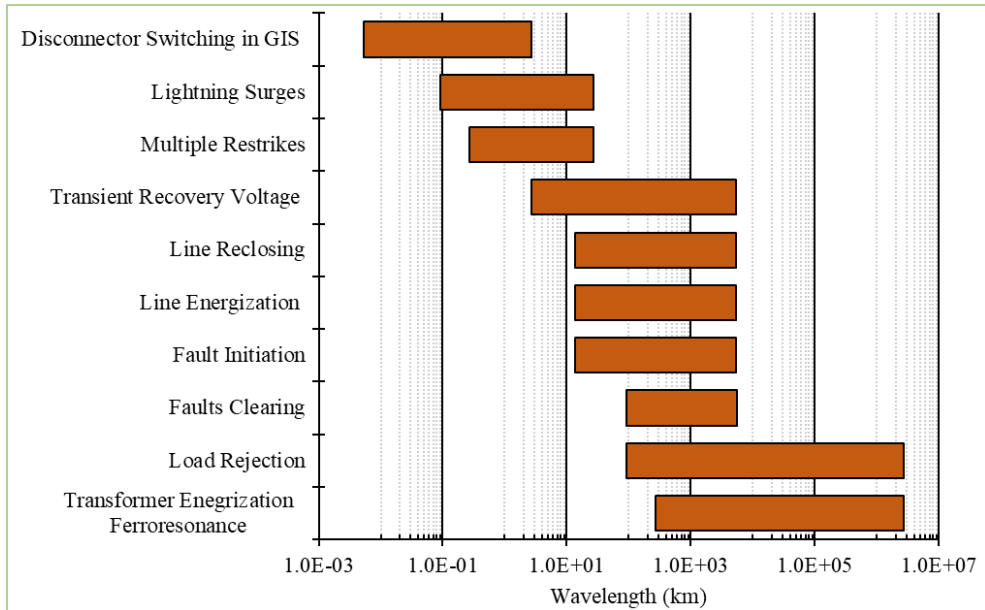


**Figure 3.1. The origin of power system electrical transients and most common associated wavelength ranges.**

Transients move along distribution lines by the interchange between the electrical energy stored in the line's distributed capacitance and the magnetic energy stored in the distributed inductance. Moving transients are called TWs. Chapter 3 discusses the TW theory and the behaviour of TWs at line junctions.

### 3.2. The travelling wave theory

Figure 3.2 shows the voltage source ( $V$ ) switches on a two-wire transmission line at  $t = 0$ . After a time ( $\delta t$ ), only a small segment ( $\delta x$ ) of the line can be charged instantaneously. If the capacitance ( $C$ ) of the line is  $C'$  farads per unit length, a charge ( $\delta Q = C'V\delta x$ ) will have been transferred to the line from the source. Because of this charge, an electrical field ( $E$ ) is then created between the line and the ground over the first  $\delta x$  unit's length. The flowrate of charge (current) can then create a magnetic field around the line segment. The current is determined from the rate that the charge flows through an infinitesimal  $\delta x$ , that is:

$$I = \lim_{\delta x \rightarrow 0} \frac{\delta Q}{\delta t} = \lim_{\delta x \rightarrow 0} C'V \frac{\delta x}{\delta t} \quad (3.1)$$

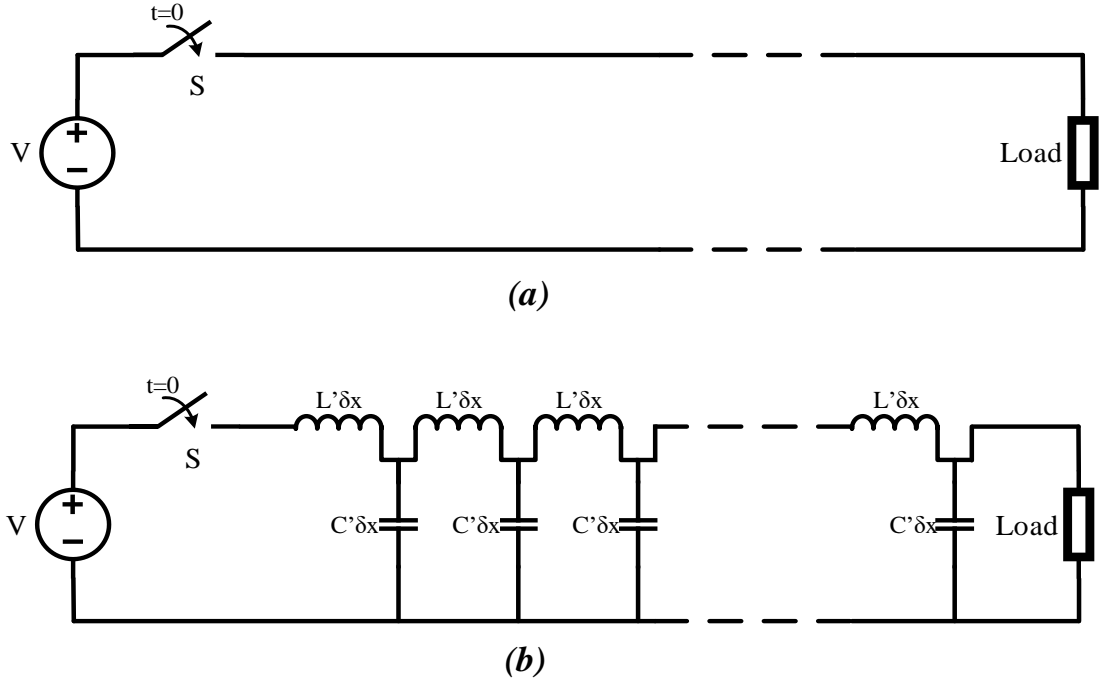


**Figure 3.2. The voltage source for (a) a two-wire transmission line; and (b) a ‘lumpy’ representation of a two-wire line [58].**

If  $\delta x/\delta t$  is the rate at which the charge propagates along the line, where this is designated as  $\vartheta$ , then:

$$I = C'V \vartheta \quad (3.2)$$

The current flows from the source into one conductor and out of the other conductor back to the source by a displacement current at the wavefront. The magnetic flux, which links line segments with an inductance ( $L$ ) of  $L'$  henries per unit length, is:

$$\phi = L'I\delta x \quad (3.3)$$

Substitute equation (3.2) into (3.3):

$$\phi = L'C'V \vartheta \delta x \quad (3.4)$$

The electric flux is created continuously at the wavefront, and the electromotive force is equal to the rate of change of flux linkage that is induced in the loop, which is created by the wavefront and the conductors [58]. The induced electromotive force is equal to:

$$emf = V = \lim_{\delta t \rightarrow 0} \frac{\delta \phi}{\delta t} = \lim_{\delta t \rightarrow 0} (L'C'V \vartheta \frac{\delta x}{\delta t}) = L'C'V \vartheta^2 \quad (3.5)$$

Thus, an expression for the propagation speed is given by:

$$\vartheta = \frac{1}{\sqrt{L'C'}} \quad (3.6)$$

The propagation speed of voltage and current TW along the line depends on the line geometry and electromagnetic properties of the surrounding media. If the

space between the conductors ( $d$ ), in meters, is large compared to the conductor radius ( $r$ ), then the flux within the conductors can be neglected; a good approximation for the  $L'$  and  $C'$  is:

$$L' = \frac{\mu_0}{\pi} \ln \frac{d}{r} \text{ H/m} \quad (3.7)$$

and

$$C' = \frac{\pi \epsilon_0}{\ln \frac{d}{r}} \text{ F/m} \quad (3.8)$$

Substituting equations (3.7) and (3.8) into equation (3.6) gives:

$$\vartheta = \frac{1}{\sqrt{\mu_0 \epsilon_0}} \text{ (m/s)} \quad (3.9)$$

Where, independent of the line geometry:

- $\epsilon_0$  is the electrical permittivity.
- $\mu_0$  is the magnetic permeability of free space.
- $\vartheta$  is the velocity of the TW in free space.

However, the  $L'$  and  $C'$  are more than the approximations shown in equations (3.7) and (3.8). Thus,  $\vartheta$  is somewhat less than the speed of light. For underground cables, the ambient medium is not air; therefore, the permittivity ( $\epsilon$ ) of the dielectric is  $\epsilon_r \epsilon_0$ , and the  $\epsilon_r$  is normally between 3 and 5, or higher. Similarly, the permeability ( $\mu$ ) may greatly exceed  $\mu_0$  if a cable is buried in a steel conduit or has steel armour wires. A change in relative permittivity ( $\epsilon_r$ ) and relative permeability ( $\mu_r$ ) affects the velocity with a ratio of  $(\mu_r / \epsilon_r)^{1/2}$ . By substituting equation (3.2) into equation (3.6), the ratio of the current and voltage amplitude can be expressed as:

$$Z_c = \frac{V}{I} = \left( \frac{L'}{C'} \right) \quad (3.10)$$

$Z_c$  is the characteristic impedance. It is identical with the surge impedance of an LC circuit.

### 3.2.1. Telegrapher's Equations

The telegrapher's equations are a pair of linear differential equations that describe the voltage and current on electrical transmission lines as a function of distance and time. The equations were formulated by Oliver Heaviside (1850 to 1925) when he was working for a telegraph company [59]. If a  $\delta x$  of the line shown in Figure

3.2 has an inductance of  $L'$ , capacitance of  $C'$ , resistance of  $R'$  and a parallel conductance of  $G'$  per unit length, the line parameters for a small segment ( $\delta x$ ) will be  $L'\delta x$ ,  $C'\delta x$ ,  $R'\delta x$  and  $G'\delta x$  (see Figure 3.3).

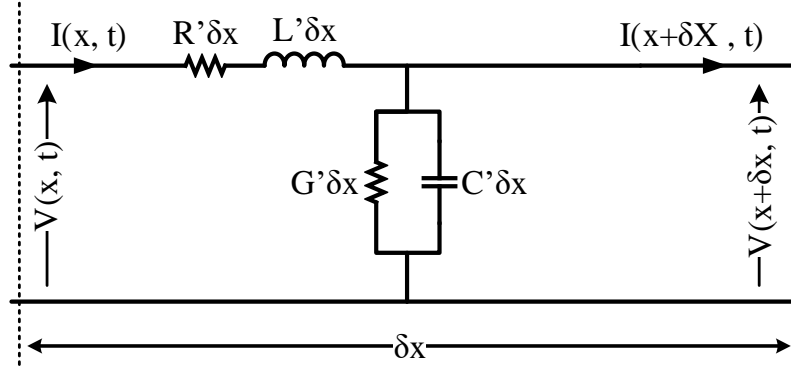


**Figure 3.3. A small segment of a transmission line (Heaviside's model).**

The electric flux ( $\psi$ ) and magnetic flux ( $\phi$ ) generated by an electromagnetic wave induced a transient voltage,  $v(x, t)$ , and current,  $i(x, t)$ . Therefore:

$$d\psi(t) = V(x, t)C'\delta x \quad (3.11)$$

and

$$d\phi(t) = i(x, t)L'\delta x \quad (3.12)$$

The voltage across the  $\delta x$  of the line will be:

$$V(x, t) - V(x + \delta x, t) = -dV = -\frac{\partial V(x, t)}{\partial x} \delta x = (R' + L' \frac{\partial}{\partial t}) i(x, t) \delta x \quad (3.13)$$

By cancelling  $\delta x$  from both sides of equation (3.13), the voltage equation becomes:

$$\frac{\partial V(x, t)}{\partial x} = -L' \frac{\partial i(x, t)}{\partial t} - R' i(x, t) \quad (3.14)$$

Similarly, for the current flowing through ( $G'\delta x$ ) and the current charging ( $C'\delta x$ ), Kirchhoff's current law can be applied as:

$$i(x, t) - i(x + \delta x, t) = -di(x, t) = -\frac{\partial i(x, t)}{\partial x} \delta x = (G' + C' \frac{\partial}{\partial t}) V(x, t) \delta x \quad (3.15)$$

If  $\delta x$  is cancelled from both sides of equation (3.15), the current equation becomes:

$$\frac{\partial i(x, t)}{\partial x} = -C' \frac{\partial V(x, t)}{\partial t} - G' V(x, t) \quad (3.16)$$

The negative sign arises in equation (3.16) because when the current and voltage waves propagate in the positive x-direction,  $i(x, t)$  and  $v(x, t)$  decrease in

amplitude for increasing  $x$ . By differentiating equations (3.15) and (3.16) for  $x$ , the second-order partial differential equations are:

$$\frac{\partial^2 i(x, t)}{\partial x^2} = -Y \frac{\partial u(x, t)}{\partial t} = YZi(x, t) = \gamma^2 i(x, t) \quad (3.17)$$

and

$$\frac{\partial^2 V(x, t)}{\partial x^2} = -Z \frac{\partial i(x, t)}{\partial t} = YZV(x, t) = \gamma^2 V(x, t) \quad (3.18)$$

Where:

$$Z = R + \frac{\partial L'(x, t)}{\partial t}$$

and

$$Y = G + \frac{\partial C'(x, t)}{\partial t}$$

The propagation constant ( $\gamma$ ) is equal to:

$$\gamma = \sqrt{ZY} = \alpha + j\beta.$$

Where:

- $\alpha$  is the attenuation constant, which influences the amplitude of a TW
- $\beta$  is the phase constant, which influences the phase displacement of the TW.

Equations (3.17) and (3.18) can be solved using the Laplace transform. The solutions for equations (3.17) and (3.18) in the time domain are:

$$V(x, t) = e^{\gamma x} f_1(t) + e^{-\gamma x} f_2(t) \quad (3.19)$$

and

$$i(x, t) = \frac{1}{Z_c} [e^{\gamma x} f_1(t) + e^{-\gamma x} f_2(t)] \quad (3.20)$$

Where  $f_1(t)$  and  $f_2(t)$  are arbitrary functions and independent of  $x$ . The characteristic impedance ( $Z_c$ ) is equal to:

$$Z_c = \sqrt{\frac{Z}{Y}}$$

### 3.2.2. The lossless line

In transmission lines, the series resistance ( $R'$ ) and shunt conductance ( $G'$ ) are relatively small in comparison to the inductance ( $L'$ ) and capacitance ( $C'$ ). Hence, in most studies, the  $R$  and  $G$  can be ignored. If the series resistance and shunt conductance

are zero, the transmission line is ‘lossless’ and the equations are substantially simpler.

For a lossless line, equations (3.17) and (3.18) become:

$$\frac{\partial^2 i(x, t)}{\partial x^2} = -C' \frac{\partial^2 u(x, t)}{\partial t} \quad (3.21)$$

and

$$\frac{\partial^2 v(x, t)}{\partial x^2} = -L' \frac{\partial^2 i(x, t)}{\partial x \partial t} \quad (3.22)$$

Solving equations (3.21) and (3.22) for  $i(x, t)$  and  $v(x, t)$  gives:

$$\frac{\partial^2 i(x, t)}{\partial x^2} = L'C' \frac{\partial^2 i(x, t)}{\partial t^2} \quad (3.23)$$

and

$$\frac{\partial^2 v(x, t)}{\partial x^2} = L'C' \frac{\partial^2 v(x, t)}{\partial t^2} \quad (3.24)$$

The  $\gamma$  and  $Z_c$  for a lossless line are:

$$\gamma = \sqrt{L'C'}$$

and

$$Z_c = \sqrt{\frac{L'}{C'}}$$

Note that the characteristic impedance of a lossless line is identical to the surge impedance of an LC circuit.

### 3.3. Reflection and refraction of travelling waves

If a characteristic impedance changes, for example, at a change in line construction, junction of several lines or location of a shunt-connected element, an adjustment must occur to maintain the proportionality between the voltage and current TW pair. This adjustment initiates two new TW pairs: reflected and refracted waves. The reflected TW travels back down the line and is superimposed on the original TW. The refracted TW propagates beyond the junction. The amplitudes and proportionality of the reflected and refracted waves are preserved for each pair and determined by the characteristic impedance of the lines on which they are travelling [58].

Consider the junction between the lines of characteristic impedance  $Z_A$ ,  $Z_B$  and  $Z_C$  in Figure 3.4. Junctions of this form occur in distribution networks at the branches



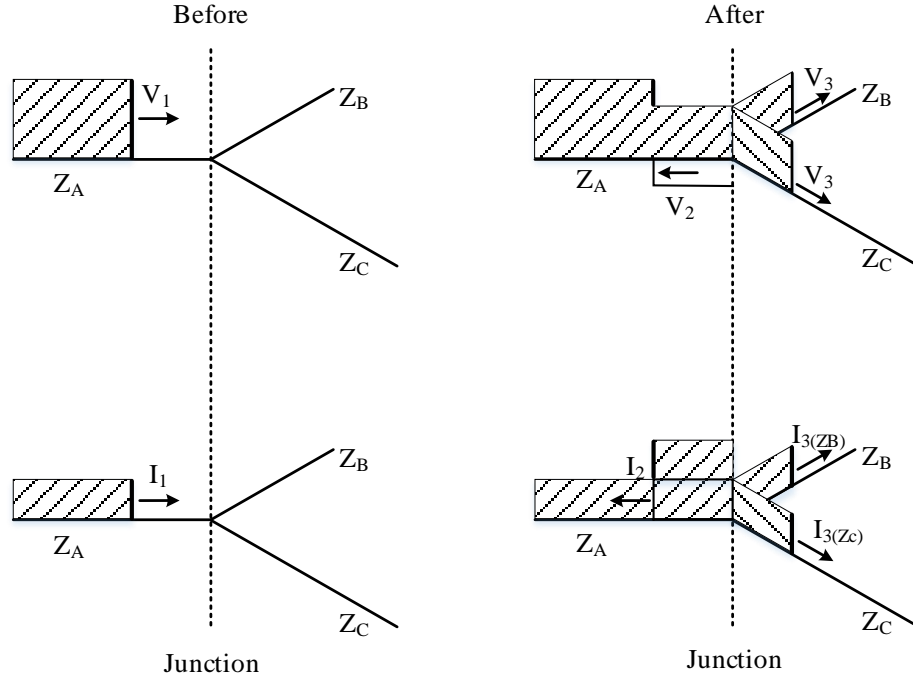


**Figure 3.4. The junctions between lines with characteristic impedance  $Z_A$ ,  $Z_B$  and  $Z_C$ .**

and tee connections. They also occur when a device, such as a transformer, is connected to a line.

A voltage TW with an amplitude of  $V_1$  approaches the junction through the branch with a characteristic impedance of  $Z_A$ . If a line is lossless, the characteristic impedance of an overhead line will be purely resistive. Therefore, a current TW has the same shape as a voltage TW and amplitude of:

$$I_1 = \frac{V_1}{Z_A} \quad (3.25)$$

The reflected and refracted voltage waves are  $V_2$  and  $V_3$ , respectively. The refracted and reflected current waves are shown below:

$$I_{3(Z_B)} = \frac{V_3}{Z_B} \quad (3.26)$$

$$I_{3(Z_C)} = \frac{V_3}{Z_C} \quad (3.27)$$

$$I_2 = -\frac{V_2}{Z_A} \quad (3.28)$$

The negative sign in equation (3.28) arises due to the changes in the travelling direction of the  $I_2$  wavefront. If the voltages are continuous at the junction and Kirchhoff's current law is imposed, it follows that:

$$V_1 + V_2 = V_3 \quad (3.29)$$

and

$$I_1 + I_2 = I_{3(Z_B)} + I_{3(Z_C)} \quad (3.30)$$

Equation (3.30) can be rewritten by substituting equations (3.26), (3.27) and (3.28):

$$\frac{V_1}{Z_A} - \frac{V_2}{Z_A} = \frac{V_3}{Z_B} + \frac{V_3}{Z_C} \quad (3.31)$$

From equation (3.31), the refracted voltage can be written as:

$$V_3 = \frac{1}{Z_A} \left( \frac{Z_B \cdot Z_C}{Z_B + Z_C} \right) (V_1 - V_2) \quad (3.32)$$

By substituting equation (3.29) into equation (3.32):

$$V_3 = \frac{2Z}{Z + Z_A} V_1 \quad (3.33)$$

Where:

$$Z = \left( \frac{Z_B \cdot Z_C}{Z_B + Z_C} \right) \quad (3.34)$$

The quantity ( $Z$ ) is equal to the parallel characteristic impedance of  $Z_B$  and  $Z_C$ ; the terminating impedance is by the line section  $Z_A$ . When  $Z = Z_A$ , the refracted wave is equal to the incident wave. That is, the incident wave propagates through the junction without attenuation. Similarly, the reflected wave is obtained by eliminating  $V_3$  between equations (3.29) and (3.32):

$$V_2 = V_1 \left( \frac{Z - Z_A}{Z + Z_A} \right) \quad (3.35)$$

When  $Z = Z_A$ , the reflected wave magnitude is equal to zero. In equations (3.33) and (3.35), the following quantities appear:

$$\text{refraction coefficient} = b = \frac{2Z}{Z + Z_A}$$

$$\text{reflection coefficient} = a = \frac{Z - Z_A}{Z + Z_A}$$

Where  $Z$  is equal to the parallel characteristic impedance of the other lines or impedances.

### 3.3.1. Reflection and refraction coefficients at line bifurcations

Radial distribution networks include many junctions between overhead lines and cables. Consider the junction between the lines of characteristic impedance,  $Z_A$  and  $Z_B$  (see Figure 3.5).

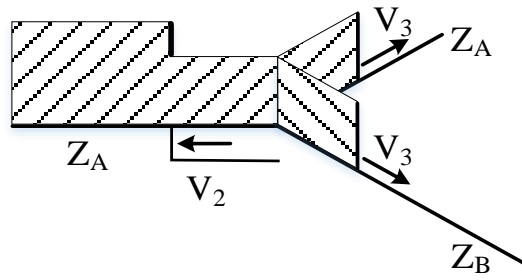


**Figure 3.5. The junction between lines with the characteristic impedance of  $Z_A$  and  $Z_B$ .**

If both the lines are lossless and the characteristic impedances are purely resistive, then:

$$Z_A = r Z_B$$

Therefore, the reflection and refraction coefficient become:

$$\text{reflection coefficient} = a = -\frac{r}{r+2} \quad (3.36)$$

and

$$\text{refracted coefficient} = b = \frac{2}{r+2} \quad (3.37)$$

If  $Z_A$  and  $Z_B$  are equal, the reflection and refraction coefficients are equal to  $-1/3$  and  $2/3$ , respectively.

The other common configuration in distribution networks is a cable tee-off from the overhead line. For a typical overhead power line, the characteristic impedance is about  $380 \Omega$ , and for a cable, it is in the range of 30 to  $80 \Omega$ . If  $Z_A$  is eight times larger than  $Z_B$ , the reflection and refraction coefficients are  $-0.8$  and  $0.2$ , respectively. Therefore, the larger portion of the TW reflects at the junction of the overhead line and cable. By increasing the value of  $r$  reflection coefficient will be increased to the maximum value of  $-1$  and refraction coefficient will approach zero.

### **3.3.2. Reflection and refraction coefficients at the junctions of power lines and capacitors**

In distribution networks, the power lines and power apparatus (e.g., capacitors and distribution transformers) often form the junctions. It is assumed that a TW wave approaches down the distribution line of surge impedance ( $Z_A$ ) to the junction with the capacitor (see Figure 3.6).

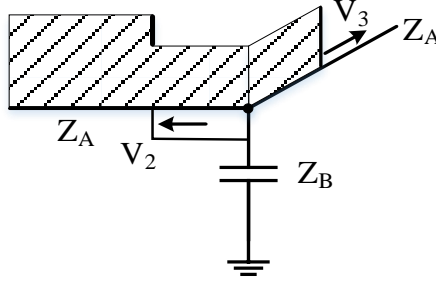


**Figure 3.6. The junction of the line and capacitor.**

The quantities are written in s-domain to simplify the equation. In a lossless line, the  $Z_A$  is purely resistive and is independent of  $s$ , and:

$$Z_B(s) = \frac{1}{Cs}$$

Using equations (3.33) and (3.34) gives the following:

$$V_2(s) = -\frac{s}{s + \frac{2}{Z_A C}} V_1(s) \quad (3.38)$$

$$V_3(s) = \frac{2}{Z_A C s + 2} V_1(s) \quad (3.39)$$

Because  $Z_A$  is resistive,  $Z_A C$  is a time constant that charges the capacitor through the distribution line with the characteristic impedance of  $Z_A$ . If:

$$\tau_c = Z_A C$$

then, equations (3.38) and (3.39) can be rewritten:

$$V_2(s) = -\frac{s}{s + \frac{1}{\tau_c}} V_1(s) \quad (3.40)$$

$$V_3(s) = \frac{2}{\tau_c s + 2} V_1(s) \quad (3.41)$$

### 3.3.3. Reflection and refraction coefficients at the junctions of power lines and inductance

The same technique that is applied to transmission line junctions with capacitors can be applied to the junctions of distribution lines and inductance (see Figure 3.7).

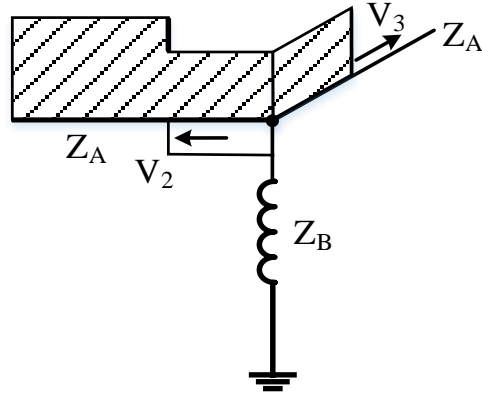


**Figure 3.7. The junction of a line and the inductance.**

Where  $Z_B(s) = Ls$ , then, by using equations (3.33) and (3.34), the following occurs:

$$V_2(s) = -\frac{\frac{Z_A}{2L}}{s + \frac{Z_A}{2L}} V_1(s) \quad (3.42)$$

$$V_3(s) = \frac{s}{s + \frac{Z_A}{2L}} V_1(s) \quad (3.43)$$

The time constant of an LR series circuit is measured by  $\tau_L = L/R$  in seconds, where  $R$  is the value of the resistor in ohms and  $L$  is the value of the inductor in henries. Because  $Z_A$  has a resistance dimension:

$$\frac{Z_A}{L} = \frac{1}{\tau_L}$$

Therefore, equations (3.42) and (3.43) can be rewritten in the following ways:

$$V_2(s) = -\frac{\frac{1}{2\tau_L}}{s + \frac{1}{2\tau_L}} V_1(s) \quad (3.44)$$

$$V_3(s) = \frac{s}{s + \frac{1}{2\tau_L}} V_1(s) \quad (3.45)$$

### 3.4. The behaviour of travelling waves at junctions

In Section 3.3, the reflection and refraction coefficients for a common junction configuration were expressed at the frequency domain. A fault originated TW is commonly assumed as a unit step function or very fast-rising front-end ramp function. In Section 3.4, the behaviour of unit step functions and ramp functions at junctions will be studied.

### 3.4.1. Model 1: unit step function travelling wave

A unit step function is a discontinuous function. Its value is equal to 0 for negative arguments and 1 for positive arguments. The unit step function in a time domain,  $u(t)$ , is defined as:

$$f(t) = \begin{cases} 0, & t < 0 \\ 1, & t \geq 0 \end{cases} \quad (3.46)$$

In S-domain, the unit step function is defined as:

$$f(s) = \frac{1}{s} \quad (3.47)$$

It is common to consider the voltage source as a unit step function and the time reference as the switching time to study power system transients during switching or faults. However, to discover the reflected and refracted unit step voltage, the time reference must be the time that the incident wave reaches the junction.

The reflected wave ( $V_2$ ) and refracted wave ( $V_3$ ) are calculated from the equations in Section 3.3. The time domain representation is found by using the inverse Laplace transformation.  $V_1(s)$  is the step function with a magnitude of  $V_1$ :

$$V_1(s) = \frac{V_1}{s} \quad (3.48)$$

Table 3.1 summarises the behaviour of step voltage TWs depending on the type of junction

### 3.4.2. Model 2: constant rising ramp travelling wave

A TW is commonly modelled as a step function or pulse with a rapidly rising leading edge. Rise times are typically in the one to ten-microsecond range. Although step functions are generated at the locations of faults, a TW's leading edge will be smoothed during the propagation of the wave in a practical system. It is more accurate to model the leading edge of a TW as a fast-rising ramp function. The ramp function in the time domain,  $v(t)$ , is defined as:

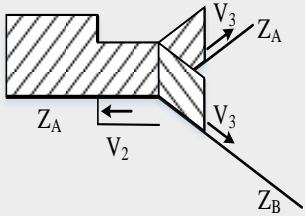
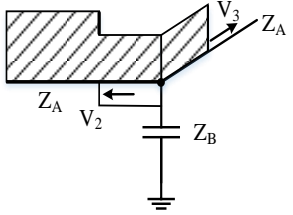
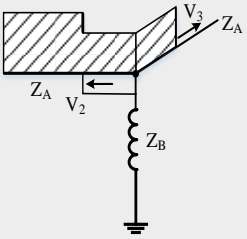
$$f(t) = \begin{cases} 0, & t < 0 \\ mt, & t > 0 \end{cases} \quad (3.49)$$

In S-domain, it is defined as:

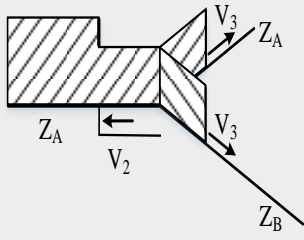
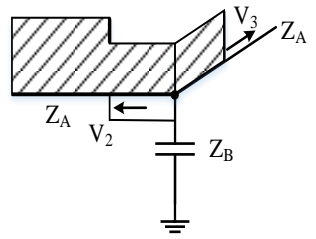
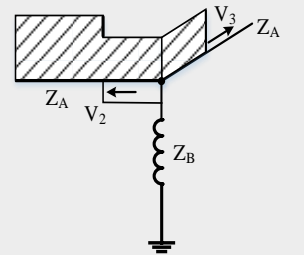
$$V(s) = \frac{m}{s^2} \quad (3.50)$$

Table 3.2 summarises the behaviour of ramp voltage TWs for different types of junctions.

**Table 3.1. The behaviour of step voltage travelling waves for different junction types**

Junction type	S-domain	Time domain	Remark
	$V_2(s) = -\frac{rV_1}{s(r+2)}$ $V_3(s) = \frac{2V_1}{s(r+2)}$	$v_2(t) = \left(-\frac{r}{r+2}\right) V_1$ $v_3(t) = \left(\frac{2}{r+2}\right) V_1$	$r = \frac{Z_A}{Z_B}$
	$V_2(s) = -\frac{V_1}{s + \frac{2}{\tau_c}}$ $V_3(s) = \frac{V_1}{s(\tau_c s + 2)}$	$v_2(t) = -V_1 e^{-\frac{2}{\tau_c} t}$ $v_3(t) = V_1 (1 - e^{-\frac{2}{\tau_c} t})$	$\tau_c = Z_A C$
	$V_2(s) = -\frac{V_1}{2\tau_L s^2 + s}$ $V_3(s) = \frac{V_1}{s + \frac{1}{2\tau_L}}$	$v_2(t) = (e^{-\frac{t}{2\tau_L}} - 1) V_1$ $v_3(t) = V_1 e^{-\frac{t}{2\tau_L}}$	$\tau_L = \frac{Z_A}{L}$

**Table 3.2. The behaviour of ramp voltage travelling waves for different junction types**

Junction type	S-domain	Time domain	Remark
	$V_2(s) = -\frac{rm}{s^2(r+2)}$ $V_3(s) = \frac{2m}{s^2(r+2)}$	$v_2(t) = -\frac{rmt}{r+2}$ $v_3(t) = \frac{2mt}{r+2}$	$r = \frac{Z_A}{Z_B}$
	$V_2(s) = -\frac{m}{s(s + \frac{2}{\tau_c})}$ $V_3(s) = \frac{2m}{s^2(\tau_c s + 2)}$	$v_2(t) = -\frac{m\tau_c}{2}(1 - e^{-\frac{2t}{\tau_c}})$ $v_3(t) = m\left(t - \frac{\tau_c}{2}\right) + \frac{m\tau_c}{2}e^{-\frac{2t}{\tau_c}}$	$\tau_c = Z_A C$
	$V_2(s) = -\frac{m}{s^2(2\tau_L s + 1)}$ $V_3(s) = \frac{m}{s(s + 1/2\tau_L)}$	$v_2(t) = 2m\tau_L \left(1 - e^{-\frac{t}{2\tau_L}}\right) - mt$ $v_3(t) = 2m\tau_L \left(1 - e^{-\frac{t}{2\tau_L}}\right)$	$\tau_L = \frac{Z_A}{L}$



### **3.5. Summary**

In this chapter, an overview of the classical travelling-wave theory is provided in detail. Moreover, travelling wave behaviour and attenuation at the line junctions are discussed. This provides a solid background for the subsequent chapters in which the travelling wave theory is employed to locate various faults in the distribution electricity grids.

## Chapter 4

# Parameter determination for modelling transformer behaviour under transient conditions

### 4.1. Introduction

Transformers are essential elements of distribution systems, after the distribution lines. The junction between overhead lines and transformers is very common. Therefore, it is important to accurately model a transformer for the study of electromagnetic transients that propagate over distribution networks. A complete high-frequency model of a transformer is complex [60]. For detailed modelling, every turn needs to be represented, including all the series, shunt capacitors and the self and mutual inductors [58]. However, not every characteristic of transformers plays a part in all transient studies. Special care must be taken to select transformer models based on the study requirements. The commonly used modelling parameters and the influence of relevant parameters are given in Table 4.1. Models of high-frequency transformers are commonly divided into two categories: (i) the transient transfers from one winding point to another point is important; and (ii) the transient transfer is not important. The models are simpler where the transfers between the winding points are not of interest. The model parameters for medium- and high-frequency studies are not provided as standard information by the manufacturers [61].

**Table 4.1. Transformer modelling guidelines**

	<b>Group I</b>	<b>Group II</b>	<b>Group III</b>	<b>Group IV</b>
	Low-frequency transients	Slow-front transients	Fast-front transients	Very fast-front transients
Parameter/effect	0.1 Hz to 3 kHz	50 Hz to 20 kHz	1.0 kHz to 3 MHz	100 kHz to 50 MHz
Short circuit impedance	Very important	Very important	Important <sup>5</sup>	Negligible
Saturation	Very important	Very important <sup>1</sup>	Negligible	Negligible
Frequency-dependent series losses	Very important	Important	Negligible	Negligible
Hysteresis and iron losses	Important <sup>2</sup>	Important <sup>3</sup>	Negligible	Negligible
Capacitive coupling	Negligible	Important <sup>4</sup>	Very important <sup>5</sup>	Very important <sup>5</sup>

Note: (1) For transformer energisation and load rejection with high voltage increase, otherwise negligible; (2) only for resonance phenomena; (3) only for transformer energisation; (4) only for surge transfer; and (5) for surge transfer. Sourced from the International Conference on Large High Voltage Electric Systems. Study Committee 33 (Overvoltages and Insulation Co-ordination). Working Group 02 (Internal Overvoltages) [57].

Where the reflection and refraction of a fast-front TW are the focus of a study, a simple surge impedance model can represent a transformer. The surge impedance is relatively easy to determine for a large power transformer through off-line testing. A DC is established in the primary winding and then interrupted. The interruption of the direct current in the winding excites an oscillatory transient at the natural frequency of the transformer, which is determined by the magnetising inductance and the effective winding capacitances.

The effective inductance, capacitance and surge impedance can be calculated by measuring the natural frequency and interrupted DC. However, with small distribution transformers, the oscillation is critically damped or over-damped. Therefore, measuring the surge impedance using the oscillatory approach is almost impossible. Figure 4.1 shows the difference between the ringing test results of a power transformer and a small distribution transformer.

Chapter 4 develops a high-frequency model of a small distribution transformer for the study of fault originating electromagnetic transients in distribution networks. The proposed simplified transformer model is suitable for use in an Electromagnetic Transient Program (EMTP).

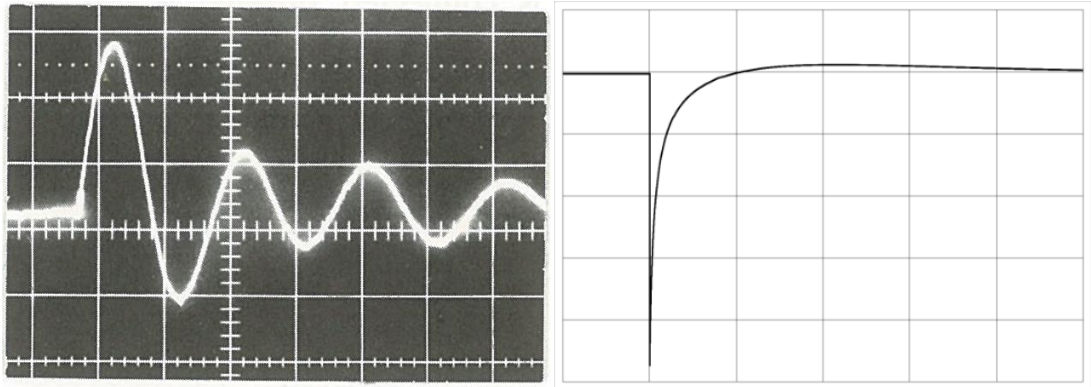


**Figure 4.1. A typical transformer response to the sudden suppression of a direct current, showing a power transformer (left) a [58] (right) Single-phase 25 kVA distribution transformer (right).**

#### **4.2. Travelling wave behaviour at the transformer terminals**

There are capacitances between every metallic part of a transformer. Each conductor segment has self-inductance, and each pair of conductor segments has mutual inductance. A simplified physical representation of winding is shown in Figure 4.2, where every circle block represents a cross-section of turns.

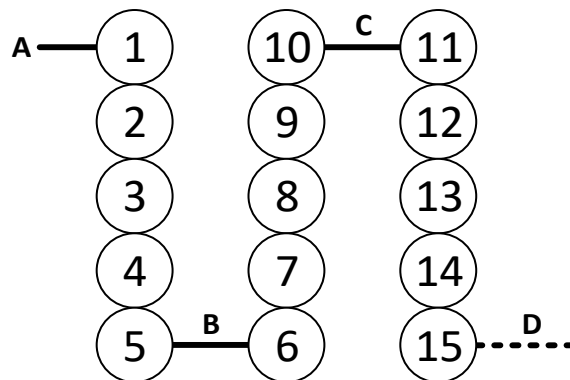


**Figure 4.2. A simplified winding cross-section through turns.**

The terminal is A, and the winding continues turn by turn to the end. Each layer can be represented by a series of inductors and capacitors between the turns, layers and ground (tank) as shown in Figure 4.3. This model does not include the inter-turn capacitances, the mutual inductances between turns or the resistance. Although it would be inadequate for some study cases, this model is helpful for exploring the behaviour of incident waves at transformer terminals.

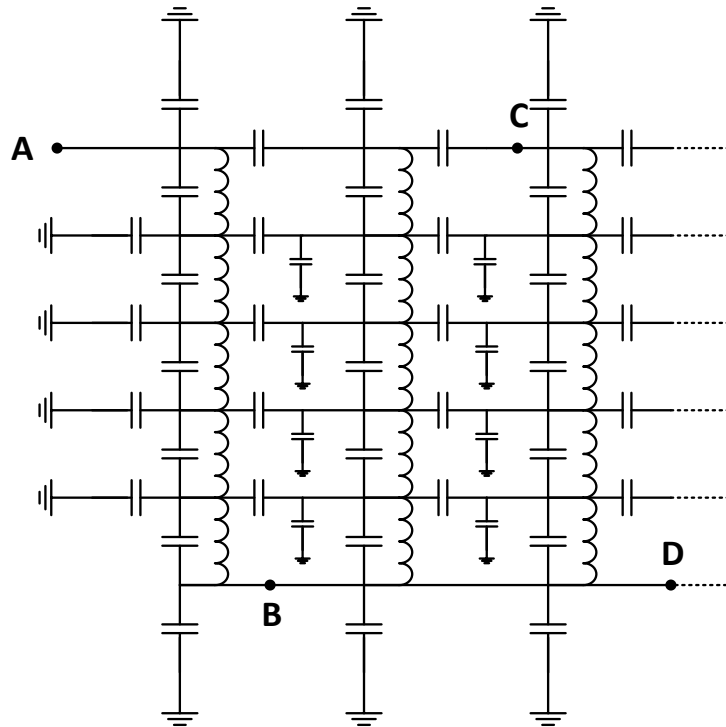


**Figure 4.3. A simplified representation of a detailed equivalent network [58].**

It is useful to divide the time after an incident wave strikes a transformer terminal into three intervals. The first period is extremely short. During this period, the windings' inductances block any fast-changing currents from entering the windings. A fast front-end incident wave considers the transformer inductances an open circuit at the low microsecond or sub-microsecond timescale. The second period starts from the point at which the currents flowing through the windings' inductances cannot be ignored. This quickly gives way to a complicated system of forced and natural responses within the windings. To replicate the initial voltage distribution, the model requires only capacitive elements. During the second and third period, the RLC circuit responses determine the transformer's behaviour.

#### **4.2.1. Admittance matrix terminal model**

Terminal models are based on the frequency or the time domain characteristic behaviour of transformers at the terminal level [62]. The transformers have been modelled as a multiport complex equivalent circuit [63]. For a single-phase transformer, a high-frequency terminal model defines the relationship between two terminal voltages and two terminal currents (see Figure 4.4).

For the frequency domain, the relationships between the terminals shown in Figure 4.4 can be written as:

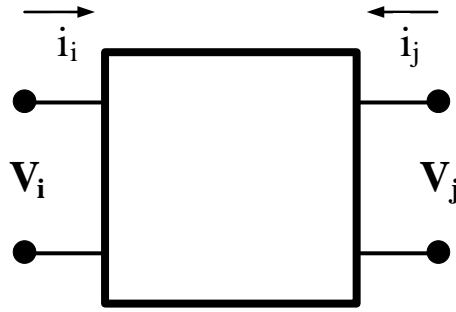


**Figure 4.4. The voltage and current of a two-port network.**

$$\begin{bmatrix} I_i(s) \\ I_j(s) \end{bmatrix} = \begin{bmatrix} Y_{ii}(s) & Y_{ij}(s) \\ Y_{ji}(s) & Y_{jj}(s) \end{bmatrix} \begin{bmatrix} V_i(s) \\ V_j(s) \end{bmatrix} \quad (4.1)$$

Where  $Y_{ij}(s)$  is the admittance between terminals  $i$  and  $j$ . Each element of the admittance matrix can be directly measured in the frequency domain. The frequency variable sinusoidal voltage waveform can be applied to one port, and the current can be measured in another port with its terminal shorted together.

In Figure 4.5, the terminals at port  $j$  are shorted together, and its voltage is equal to zero. Therefore, using equation (4.1), the current that flows into terminal  $i$  can be written as:

$$I_i(s) = Y_{ii}(s) V_i(s) \quad (4.2)$$

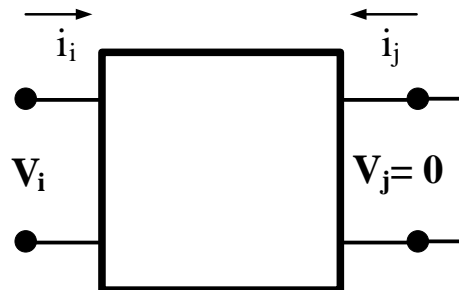


**Figure 4.5. The voltage and current of a two-port network when one port is a short circuit.**

Equation (4.2) suggests that the diagonal elements of an admittance matrix can be measured by applying a variable frequency voltage source to the terminal and measuring the current flowing into the same terminal while keeping all other terminals shorted. Conversely, the off-diagonal elements of an admittance matrix can be measured by applying a variable frequency voltage source to a terminal, while keeping all other terminals connected. For the off-diagonal elements, the current must be measured in a different terminal. Consider that the variable frequency voltage source is connected to port  $i$  and the current measure in terminal  $j$ , while other terminals are

shorted together. The voltage at port  $j$  will be equal to zero; from equation (4.1) this gives:

$$I_j(s) = Y_{ij}(s)V_i(s) \quad (4.3)$$

or

$$Y_{ij}(s) = \frac{I_j(s)}{V_i(s)} \quad (4.4)$$

If a transformer's admittance matrix is assumed to be balanced, then  $Y$  can be written as:

$$\mathbf{Y}(s) = \begin{bmatrix} Y_s(s) & Y_m(s) \\ Y_m(s) & Y_s(s) \end{bmatrix} \quad (4.5)$$

Where  $Y_s(s)$  and  $Y_m(s)$  are the average of all diagonal and off-diagonal elements, respectively. For a transformer with multiple windings, equation (4.5) can be written as:

$$\mathbf{Y}(s)_{ij} = \begin{bmatrix} Y_s(s) & \cdots & Y_m(s) \\ \vdots & \ddots & \vdots \\ Y_m(s) & \cdots & Y_s(s) \end{bmatrix}$$

Then, the symmetrical admittance matrix can be modelled using the zero and positive sequence parameters in a  $\pi$ -circuit [64]. A single-line diagram of a multi-terminal  $\pi$ -equivalent circuit is shown by Figure 4.6.

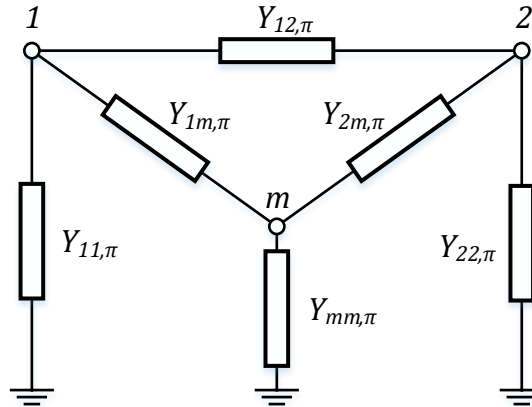


**Figure 4.6. A single-line diagram of a multi-terminal  $\pi$ -equivalent circuit [62].**

To obtain the time domain response of a transformer, the admittance matrix  $\mathbf{Y}(s)_{ij}$  is approximated with rational functions that contain real and complex conjugate poles and zeros [65]. These rational functions can be presented in the form of RLC networks, which create the parameters of an  $\pi$ -equivalent circuit. Figure 4.7 shows a

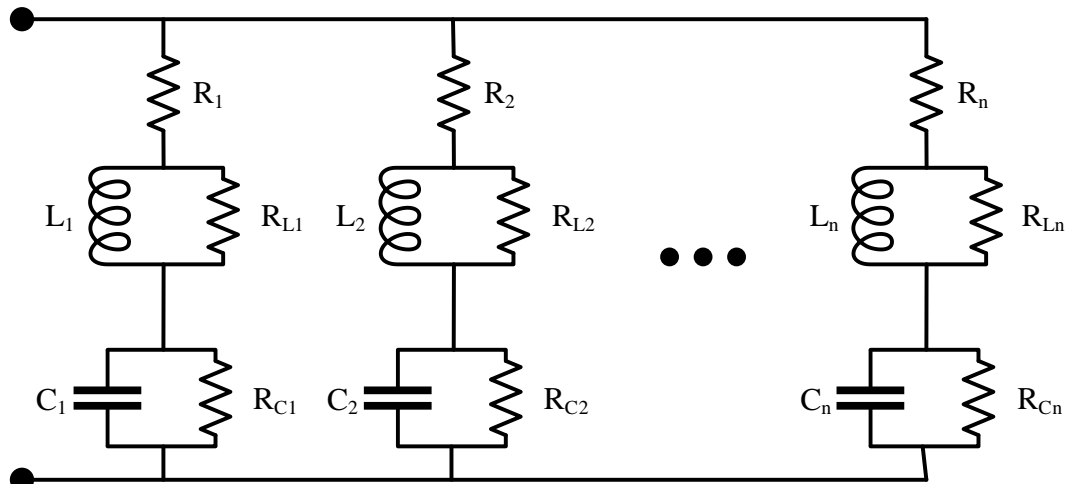


**Figure 4.7. The generic structure of a resistor, inductor, and capacitor branch.**

generic RLC branch, which can be used in a  $\pi$ -circuit to represent a transformer's positive, negative or zero sequence behaviour.

The generic structure of RLC elements reflects the known transformer characteristics for an impedance matrix, which include:

- the inductive behaviour at low frequencies (e.g., the windings and iron core eddy currents and hysteresis losses), which are reproduced by the resistor-inductor branches
- the series and parallel resonances caused by winding-to-winding and winding-to-ground stray capacitances from mid to high frequencies, which are simulated by the RLC branches
- the predominantly capacitive behaviour at high frequencies, which are represented by a single RC series branch [62].

For a known admittance matrix, a recursive convolution procedure can be used to calculate a rational approximation in the form of an RLC network in EMTP-type programs.

#### **4.2.2. Experimental measurements**

Transformer manufacturers commonly provide the power frequency model parameters. The power frequency parameters are easily obtained from standard open and short circuit test results and can often be estimated from the nameplate data. The manufacturers generally do not provide the high-frequency model, especially for small distribution transformers. The required admittances are commonly measured by vector network analysers (VNAs) [61]. VNAs are expensive and not available in most



laboratories. In this study, the admittance matrix elements of a single-phase transformer were measured using a commercial sweep frequency response analyser (SFRA).

SFRA is a diagnostic tool designed to detect the defects in a transformer's windings. It is relatively more accessible and cheaper than VNAs. The primary objective of SFRA is to determine the voltage transfer function (VTF) of transformer windings, and it uses a shunt resistor to measure the currents instead of direct measurements. Therefore, that admittance matrix that was measured with an SFRA needs to be corrected [66]. Subsection 4.2.2 demonstrates how to use an SFRA device to measure an admittance matrix. The correction procedure is based on the methods described by Morched et al. [62] and Nikolaidis et al. [61, 66]. Figure 4.8 provides a connection diagram for measuring the diagonal and off-diagonal elements.

The following equations for measuring the diagonal elements can be written for the connection diagram shown in Figure 4.8 (a):

$$I_i = (V_s - V_{in})Y_{ii} \quad (4.6)$$

and

$$I_i = V_{in}/Z_{in} \quad (4.7)$$

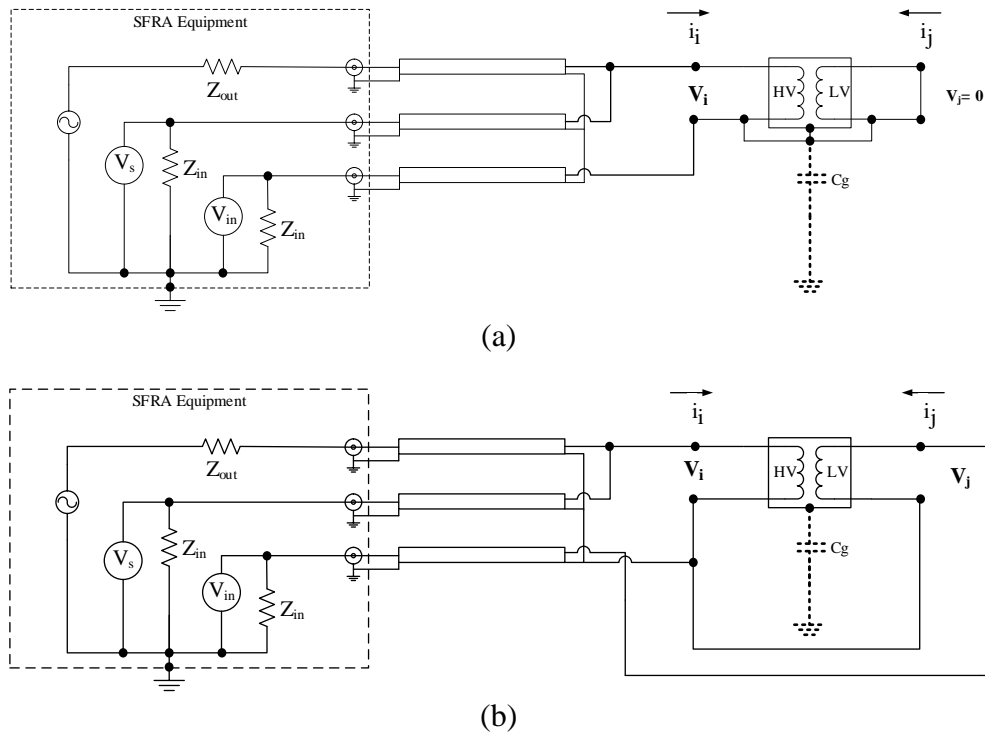


**Figure 4.8. Connection diagrams for measuring: (a) the diagonal elements of  $Y(s)$ ; and (b) the off-diagonal elements of  $Y(s)$ .**

The following equation is given from equations (4.6) and (4.7):

$$V_{in} = (V_s - V_{in})Y_{ii}Z_{in} \quad (4.8)$$

Solving equation (4.8) for  $Y_{ii}$  gives:

$$Y_{ii} = \frac{V_{in}}{Z_{in}(V_s - V_{in})} = \frac{V_{in}/V_s}{Z_{in}(1 - (V_{in}/V_s))} \quad (4.9)$$

The standard output format of SFRA equipment is a VTF,  $H(\omega)$ :

$$H(\omega) = \frac{V_{in}(\omega)}{V_s(\omega)} \quad (4.10)$$

The self-admittance of the winding,  $i$ , ( $Y_{jj}$ ), can be expressed in terms of the VTF:

$$Y_{ii}(\omega) = \frac{H(\omega)}{Z_{in}(1 - H(\omega))} \quad (4.11)$$

A transformer tank's capacitance to the ground ( $C_g$ ) can affect the measurements at very high frequencies. However, based on the physical dimension of the transformer and the required frequency range,  $C_g$  may be ignored. Alternatively, battery-powered SFRA equipment can be used to avoid any measurement errors caused by the  $C_g$  of a transformer tank [61]. In a distribution network application, transformer tanks are usually earthed for safety reasons.

Figure 4.8 (b) shows a connection diagram for measuring the off-diagonal elements of an admittance matrix using the SFRA equipment. However, the voltage of port  $j$  is not equal to zero because the current is measured through  $Z_{in}$ . From equation (4.1) and Figure 4.8 (b), the current that flows into terminal  $j$  can be expressed as:

$$I_j(\omega) = Y_{ii}(\omega)V_i(\omega) + Y_{ij}(\omega)V_j(\omega) \quad (4.12)$$

The measured, mature admittance is equal to:

$$\tilde{Y}_{ji}(\omega) = \frac{I_j(\omega)}{V_i(\omega)} - Y_{jj}(\omega) \frac{V_j(\omega)}{V_i(\omega)} \quad (4.13)$$

Equation (4.13) shows that the measured admittance,  $\tilde{Y}_{ji}(\omega)$ , is not just a mutual admittance between terminals  $j$  and  $i$ . However, the measured mutual admittance can be corrected to find the real mutual admittance between terminals  $i$  and  $j$ . The real admittance,  $Y_{ij}(\omega)$ , is equal to:

$$Y_{ij}(\omega) = \tilde{Y}_{ij}(\omega) + Y_{ii}(\omega) \frac{V_i(\omega)}{V_j(\omega)} \quad (4.14)$$

Where  $\frac{V_i(\omega)}{V_j(\omega)}$  is equal to the voltage transform function obtained from the SFRA measurements, and  $H_{ij}(\omega)$  and  $Y_{ii}(\omega)$  are the self-admittance of terminal  $i$ . Further,

from Figure 4.8 (b), the measured admittance is equal to:

$$\tilde{Y}_{ij}(s) = \frac{I_i(\omega)}{V_j(\omega)} = \frac{V_{in}(\omega)}{Z_{in}V_s(\omega)} \quad (4.15)$$

or

$$Y_{ij}(\omega) = \frac{1}{Z_{in}} H_{ij}(\omega) + Y_{ii}(s) H_{ij}(\omega) \quad (4.16)$$

Where  $H_{ij}(\omega)$  is the measured VTF obtained from the SFRA.

### 4.3. Creation of the model

Figure 4.9 shows a comprehensive high-frequency transformer model, which consists of several components that can be combined to obtain the desired simulation capabilities. The short circuit reactance ( $X_{sh}$ ) and resistance ( $R_{sh}$ ) mainly represent the loaded transformer's behaviour at low and power system frequencies. The total impedance,  $Z_{sh}$ , which is the vector sum of the resistance and reactance, is commonly provided by the manufacturer, and most national standards require that it be written on the transformer rating plate. Manufacturers routinely perform short circuit and open circuit tests. These provide a good understanding of the low-frequency model values. Transformer manufacturers do not often specify any high-frequency parameters. Only the short circuit impedance and capacitive couplings are important in a simulation model to study the fast-front transients (see Table 4.1).

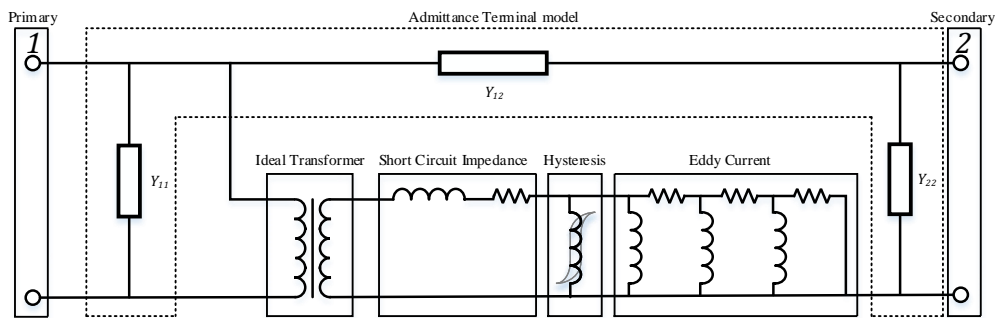


**Figure 4.9. A comprehensive model of a transformer.**

A transformer's terminal admittance versus its frequency provides the desired information to build a high-frequency transformer model for a fast-front transient.

Figure 4.10 shows a typical single-wire earth-return transformer (SWER) and its nameplate information. Its admittance-frequency characteristics have been measured and corrected based on the methods described in Subsection 4.2.2. Figure 4.11 shows the raw measured VTF magnitude and phase angle.

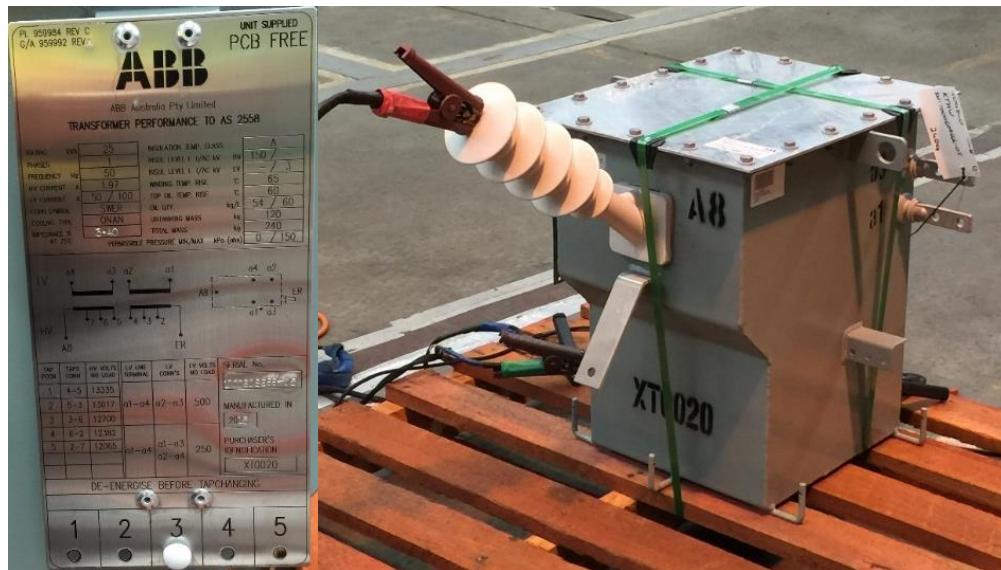
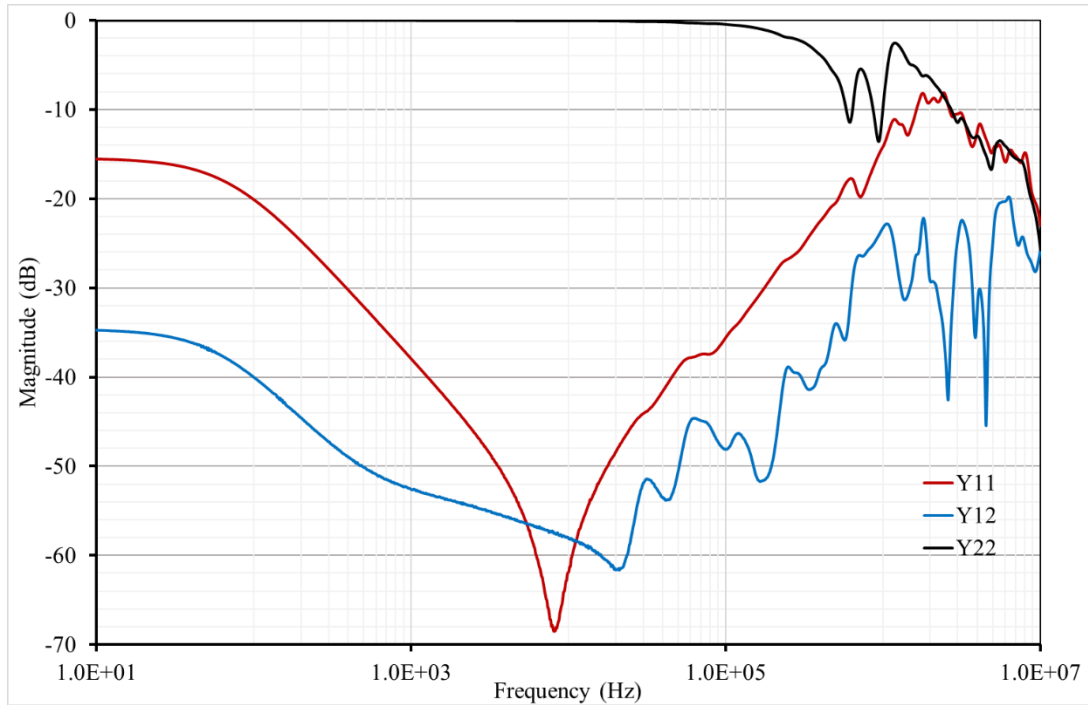


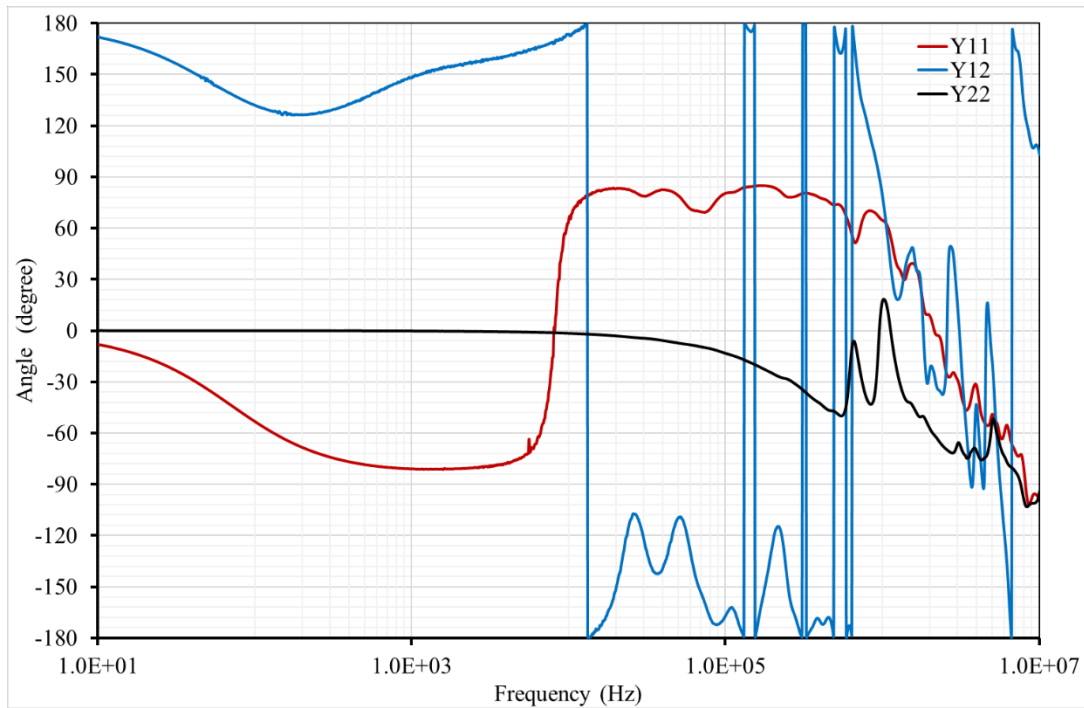
**Figure 4.10. A 25 kVA single-wire earth-return transformer and its nameplate information.**

In Figure 4.11,  $Y_{11}$  is the self-admittance of the high voltage (HV) winding,  $Y_{12}$  is the mutual admittance between the high and low voltage winding and  $Y_{22}$  is the self-admittance of the low voltage winding. Figure 4.11, especially the phase plot, demonstrates that  $Y_{11}$ , the primary winding admittance, appears initially resistive in the 10 Hz range. As the frequency increases, it becomes inductive, particularly in the region of 1 kHz. Above 10 kHz, and up to approximately 1 MHz, the admittance is capacitive. Some tools will attempt to fit complex models. The frequency-dependent branch-fitting (FDBFIT) module, which comes as a standard function of the EMTP-RV software package, was used to calculate the RLC branch elements based on the SFRA corrected measurements. Figure 4.12 to 4.14 show the transformer measured and fitted RLC equivalent admittance versus the frequency.

The fitted element's details are provided in Appendix A. The accuracy of the admittance measurements is limited at 10 Hz to 1 kHz and very high frequencies (higher than 1 MHz). The self- and transfer-admittance at low and power frequencies are affected by the short circuit impedance and magnetisation admittance. The magnetisation branch effect is evident in the low-frequency admittance angle. The low-frequency model is, topologically, a T-model. A single branch model will necessarily have errors in the low-frequency range. Therefore, only the measurements between 1 kHz and 1 MHz are used for the fitting process. Figure 4.15 shows the circuit model of a 25 kVA SWER transformer. Figure 4.16 compares the simulation model and the measured voltage transform function of the transformer.



(a)



(b)

**Figure 4.11. A 25 kVA single-wire earth-return transformer measured voltage transform function showing: (a) the magnitude; and (b) the phase angle.**

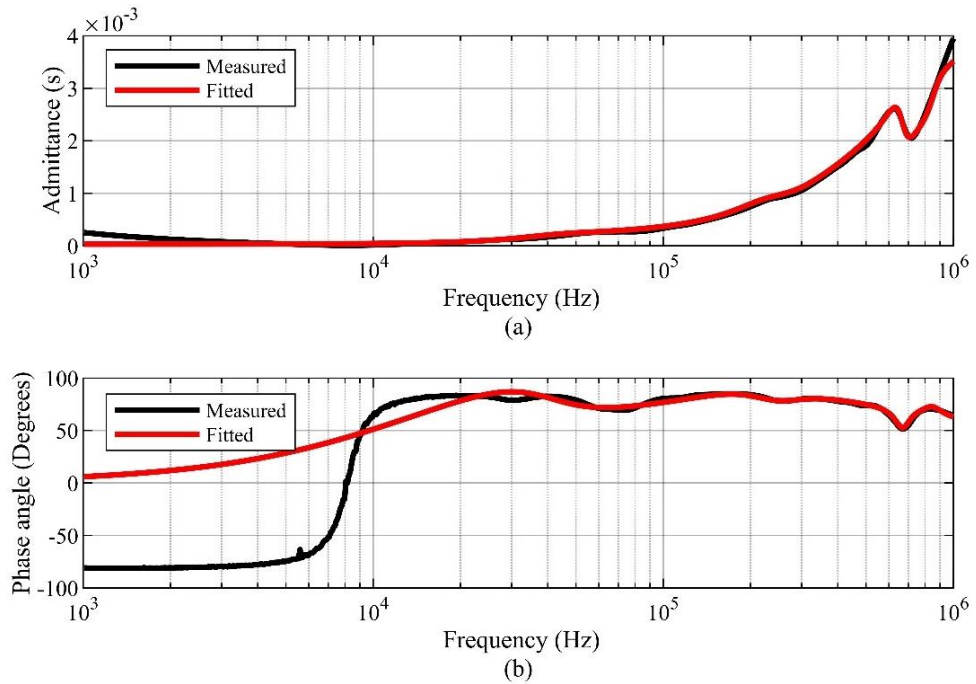


**Figure 4.12. Comparison of the frequency characteristics of a 25 kVA single-wire earth-return transformer high voltage terminal self-admittance (Y11) between the measured and resistor, inductor and capacitor fitted equivalent, showing: (a) the admittance magnitude; and (b) the admittance phase angle.**

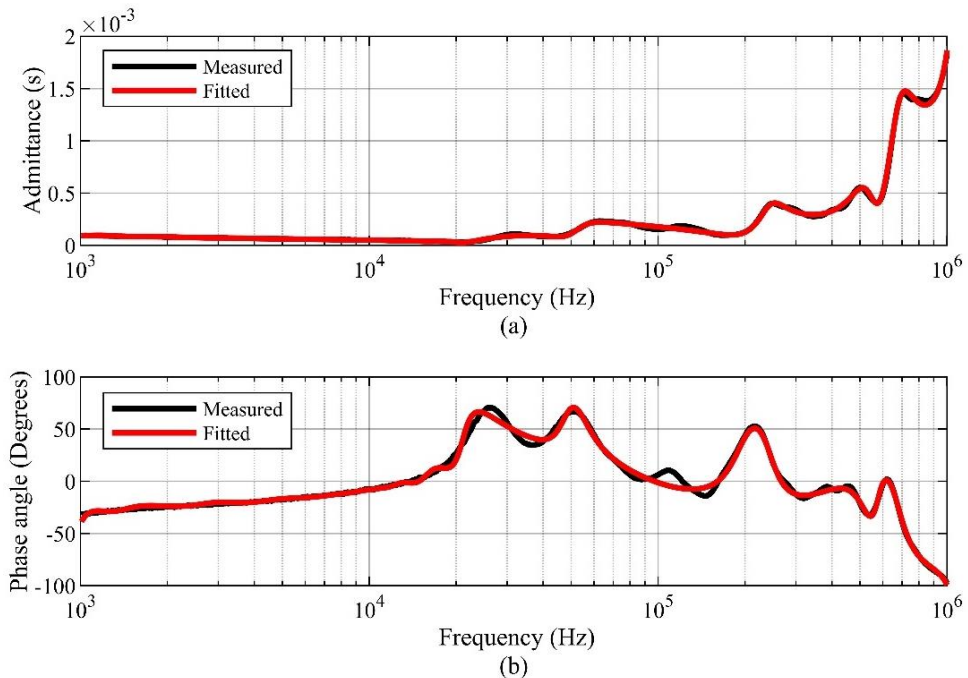


**Figure 4.13. Comparison in the transmission impedance admittance (Y12) frequency characteristics of a 25 kVA single-wire earth-return transformer between the measured and resistor, inductor and capacitor fitted equivalent showing: (a) the admittance magnitude; and (b) the admittance phase angle.**

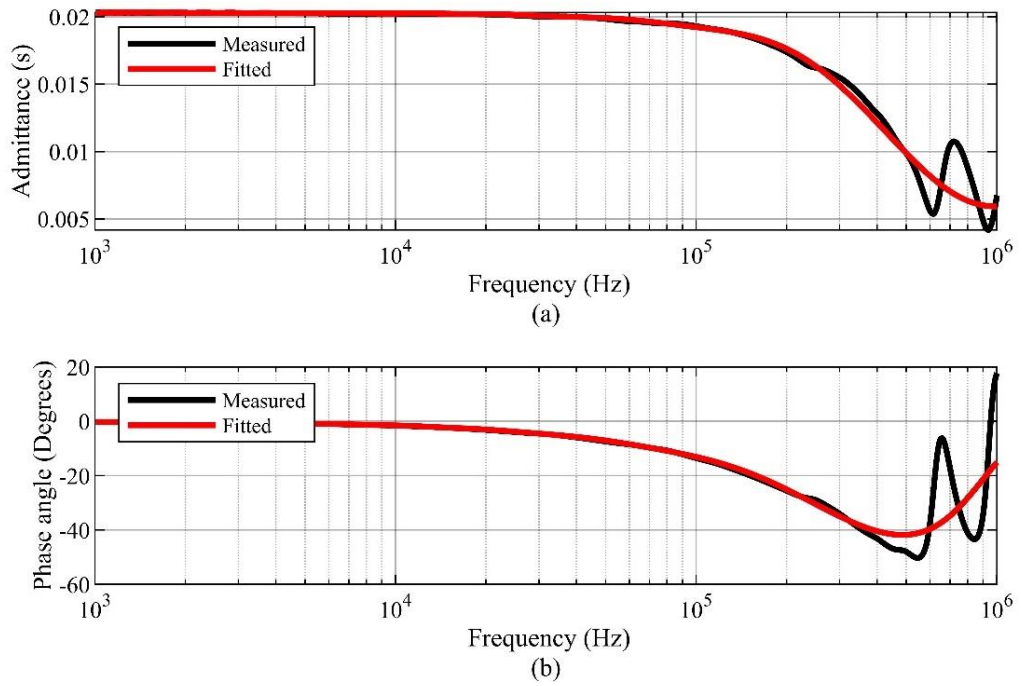


**Figure 4.14. Comparison in the low voltage terminal self-admittance ( $Y_{22}$ ) frequency characteristics of a 25 kVA single-wire earth-return transformer between the measured and RLC fitted equivalent, showing: (a) the admittance magnitude; and (b) the admittance phase angle.**

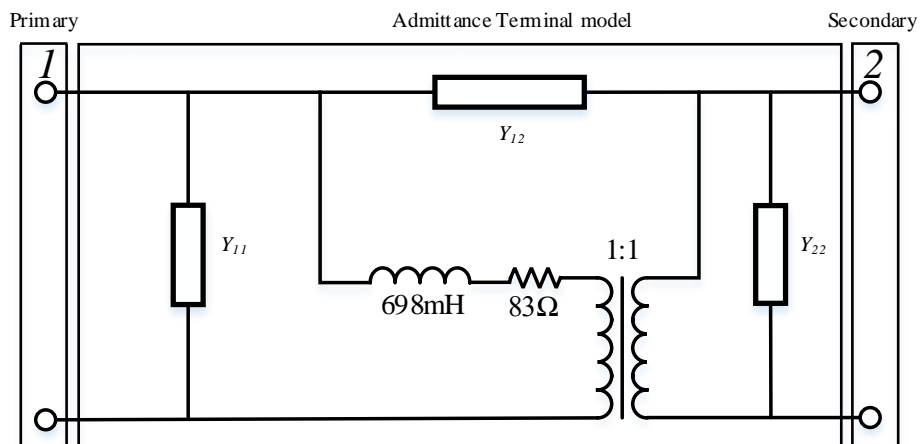


**Figure 4.15. A circuit model of a 25 kVA single-wire earth-return transformer.**



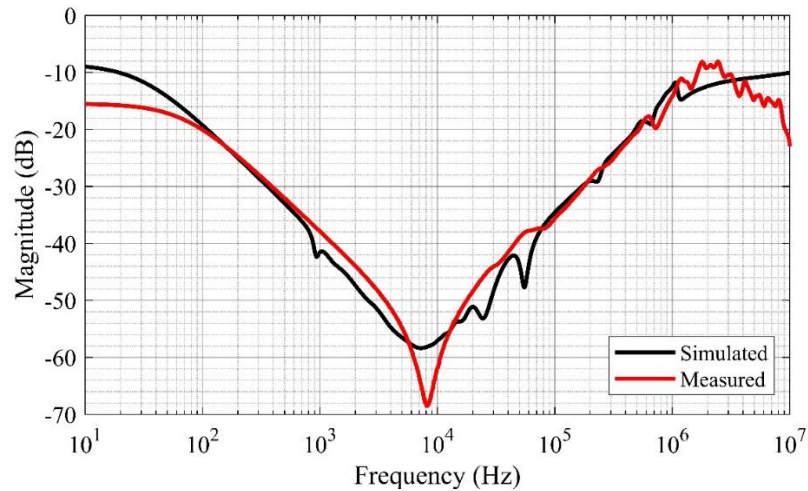


**Figure 4.16. Comparison between the simulation model and the measured voltage transfer function of a 25 kVA single-wire earth-return transformer.**

#### 4.4. Simplified transformer model

Section 4.4 provides the guidelines for developing a simplified transformer model based on the SFRA measurements. This model is appropriate for studying TW reflection and refraction in power lines and transformer junctions. The simplified model is not suitable for investigating TW penetrations into or between windings. Figure 4.17 illustrates the admittance magnitude versus frequency of an HV winding measured on a 12.7/0.240 kV, 25 kVA single-phase SWER transformer.

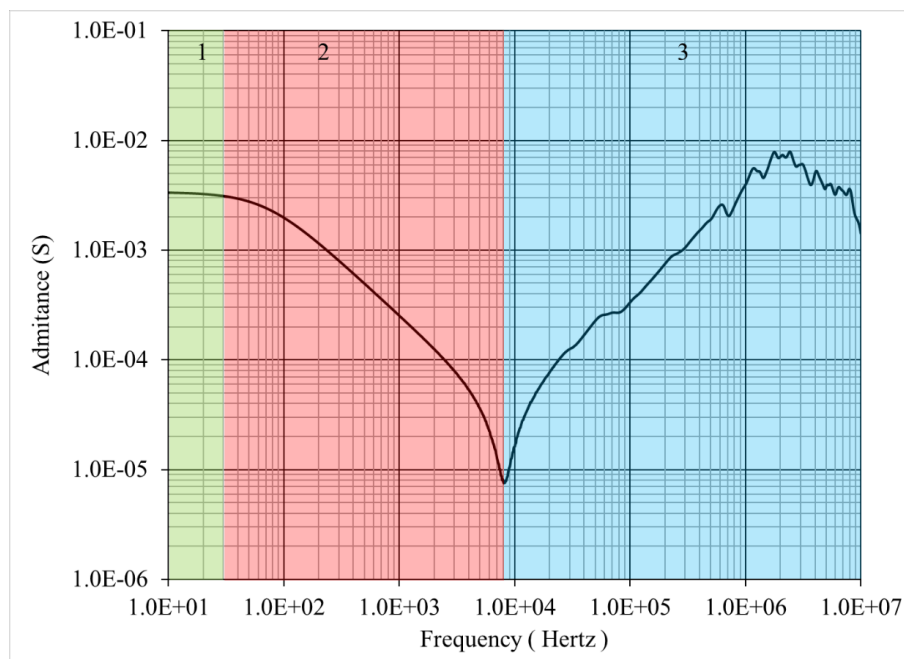


**Figure 4.17. The high voltage winding admittance magnitude of a 12.7/0.250 kV, 25 kVA single-phase single-wire earth-return transformer.**



Three distinct areas can be identified in the SFRA plot, which are shown by the different colours and numbers (see Figure 4.17). For very low frequencies (green), the winding inductance behaves like a short circuit, and the winding capacitances are an open circuit. In this area, winding resistance dominates the admittance magnitude. The skin effect is negligible, and admittance can be observed in the SFRA plot as a flat line. In the second area (red), with an increasing frequency, the inductive admittance of winding reduces. The shunt capacitive admittances are smaller but increasing with frequency. In this field, the total admittance is dominated by inductance. At the resonance frequency, inductance and capacitive admittance magnitudes are equal with the opposite sign. Above the resonance point, the admittance starts increasing and is dominated by capacitive reactance. A proposed simplified model of a single-phase transformer is shown in Figure 4.18.

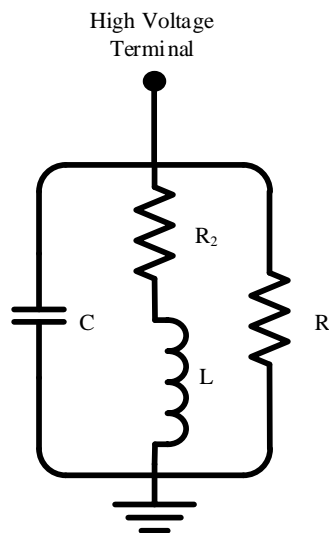


**Figure 4.18. A simplified model of a single-phase transformer.**

The behaviour of the transformer winding is, in its simplest form, a parallel RLC circuit frequency response. Therefore, the resistance, inductance and capacitance can be calculated at the resonance frequency, in the second and third areas, respectively. The extra resistance in the series with an inductance replicates the transformer's winding resistance, which is dominated by the admittance magnitude at a very low frequency (green area in Figure 4.17). The simplified model's parameters can be calculated by choosing the required data point from the admittance versus frequency graph (see Figure 4.19).

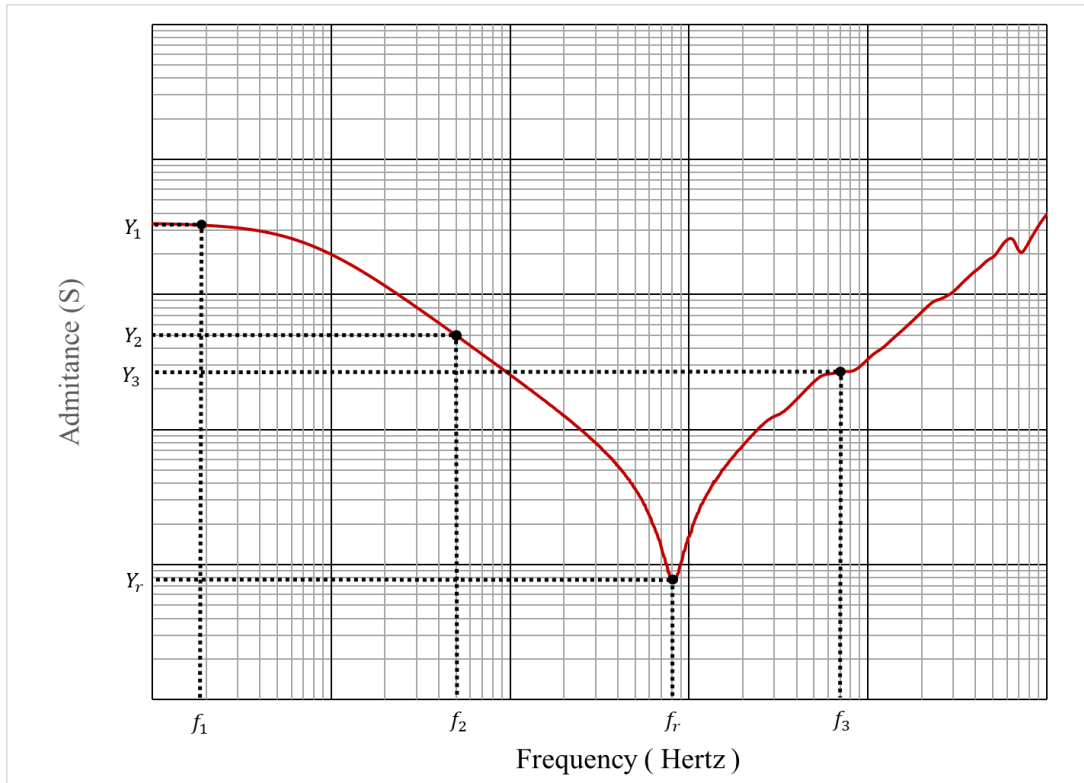


**Figure 4.19. A typical admittance versus frequency graph of distribution transformers.**

At a very low frequency, the winding resistance ( $R_2$ ) dominates the admittance and can be approximated as:

$$R_2 = \frac{1}{Y_1} \quad (4.17)$$

The winding leakage inductance can be approximated by:

$$L = \frac{1}{2\pi f_2 Y_2} \quad (4.18)$$

Similarly, the effective capacitance of the winding to the ground is approximated by:

$$C = \frac{Y_3}{2\pi f_3} \quad (4.19)$$

#### **4.4.1. Transformer load's effects**

The transformer admittances that were measured in Subsection 4.2.2 were those that were under short circuit conditions. Under this condition, the magnetisation branch short-circuited, and the transformer load impedance was  $0 \Omega$ . Therefore, the simplified model developed in Section 4.3 cannot replicate the loaded or unloaded transformer's behaviour. For a distribution transformer, the magnetisation inductance is in the range of a few henries. Due to the large inductance, the magnetisation branch

can be considered an open circuit for frequencies higher than nominal frequencies or a very fast transient. The magnetisation impedance is very high compared to the nominal transformer load. To study the TWs on a distribution network, the nominal load of the feeder is the pre-fault condition. Therefore, the magnetisation inductance can be ignored. Figure 4.20 shows the admittance versus frequency for different loading conditions on the primary winding of a small laboratory 250/120 V transformer.

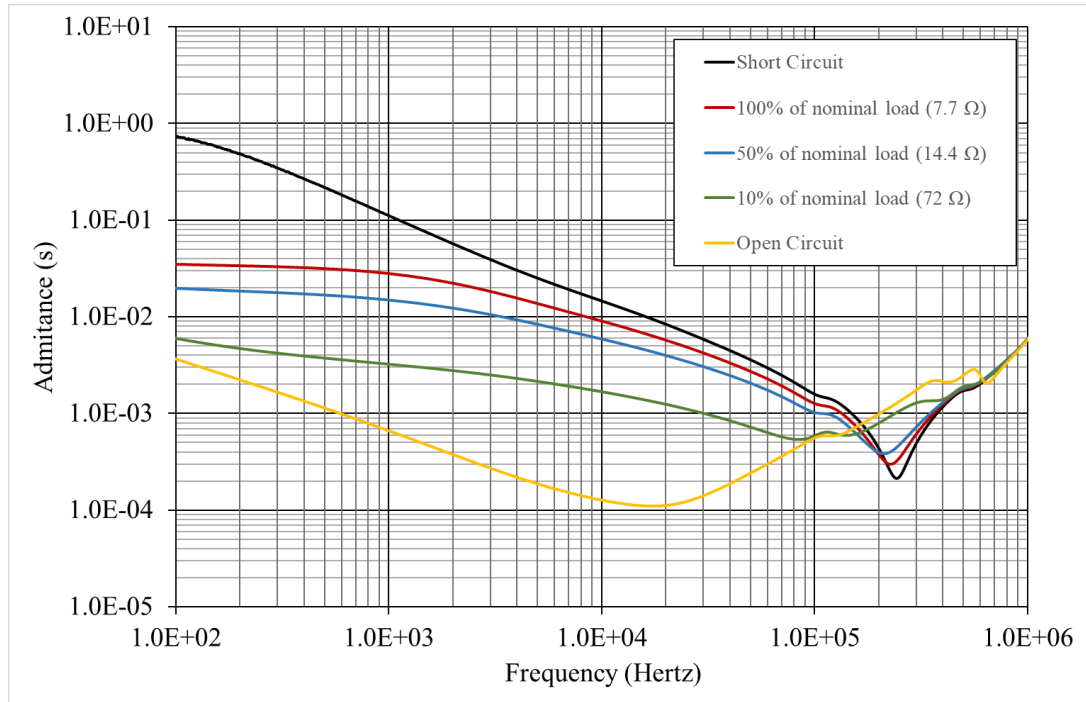


**Figure 4.20. The frequency response of a single-phase 2 kVA, 250/120 V transformer under different load conditions.**

A transformer's admittance at lower frequencies is dependent on the transformer load (see Figure 4.20). Magnetisation inductance has a greater effect on the total admittance in lower load conditions. However, the magnetisation branch can be ignored for up to 50% of the load. By assuming that there is a purely resistive load, the transformer load's effects can be added to the series resistance of the simplified model ( $R_2$ ) shown in Figure 4.18.

The resistance is equal to the secondary winding load resistance multiplied by the square of the transformer ratio:

$$R_2 = \frac{1}{Y_1} + R_{load} \times \left(\frac{V_p}{V_s}\right)^2 \quad (4.20)$$

Where:

- $Y_1$  is the measured admittance of an HV terminal at a very low frequency
- $R_{load}$  is the transformer load's impedance
- $V_p/V_s$  is the transformer's primary to secondary voltage ratio.

The simplified model parameters for the tested transformer are shown in Table 4.2. Notably, in the higher-frequency region (from 600 kHz to 1 MHz) load does not affect the input admittance that is dominated by the winding capacitances.

**Table 4.2. Model parameters for a 2 kVA, 250/120 VAC transformer in different loading conditions**

Loading	$R_2$	$R_1$	$L$	$C$
Condition	$\Omega$	$\Omega$	mH	pF
Short Circuit	1.03	4668	0.85	600
100% loaded	34.43	4668	0.85	600
50% loaded	67.83	4668	0.85	600

#### 4.4.2. Verification of model

The frequency response characteristics of the model were compared with the measured transformer frequency response to validate the simplified transformer model. Figure 4.21 shows the model in the EMTP-RV environment, which was used to simulate a transformer under a sweep frequency response analysis.

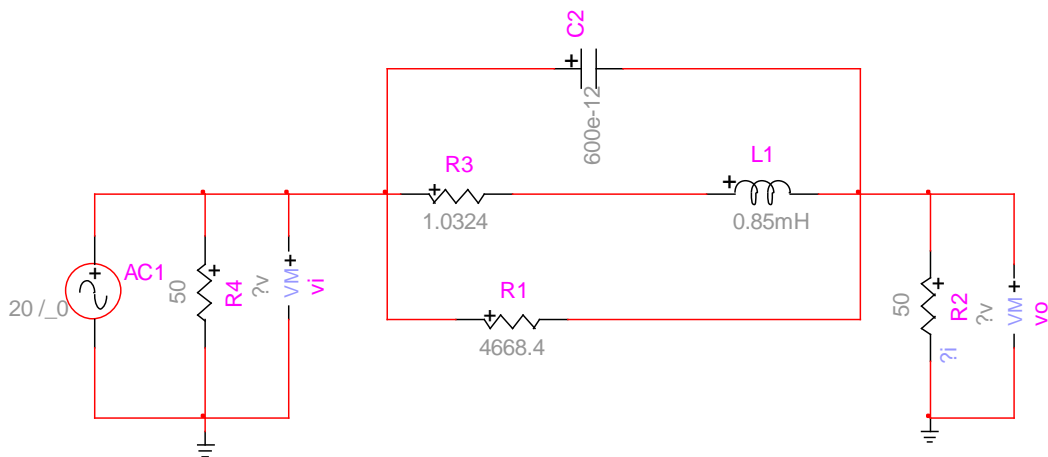


**Figure 4.21. The simple model used to simulate the sweep frequency response analyser test.**

Figure 4.22 demonstrates the measured and simulated VTF magnitudes versus the frequency of the tested transformer. The developed model closely replicates a transformer's winding behaviour adequately up to 500 kHz and strongly deviates at above 2 MHz. The intended application of the model and accuracy of the equipment must be considered when analysing very high-frequency ranges.

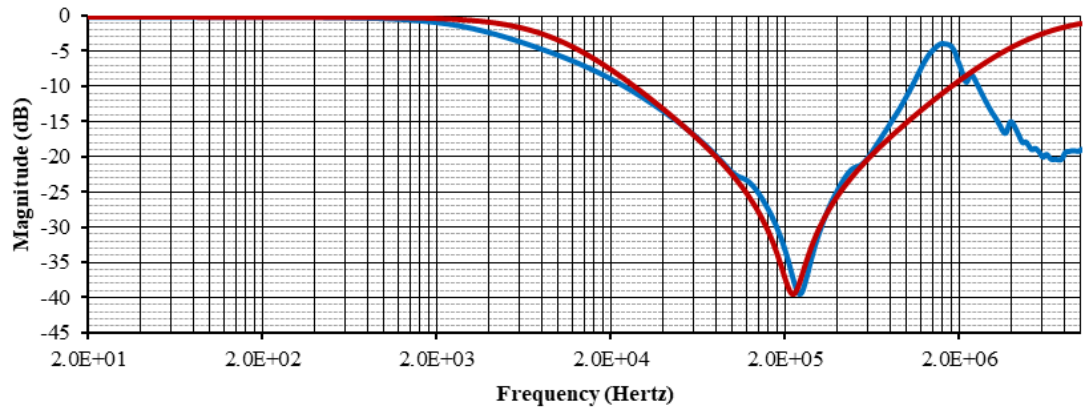
The simulation model was further verified by analysing its behaviour for sharp rising or falling edges applied with a square waveform. Figure 4.23 (a) shows the setup of the laboratory, and Figure 4.23 (b) shows the schematic diagram of the test setup. A 20 m length of 50  $\Omega$  coaxial cable was used with T-connector at the middle. A 50  $\Omega$  termination impedance was installed at the end of the cable. The signal generator produced a pulse at 1 s intervals. The pulse duration was 1 ms with a 1  $\mu$ s rise and fall time. The digital storage oscilloscope recorded the signal at a 25 Ms/s sampling rate. Figure 4.23 (c) shows the simulation circuit in the EMTP-RV environment to verify the transformer's response to the square voltage waveform. As shown by Figure 4.24, the transformer simplified model is in good agreement with the experimental results under transient conditions.

#### 4.4.3. Distribution transformer models

The simplified model of a single-phase distribution transformer was developed following the procedure described in Section 4.4, and the SFRA measurement was described in Section 4.3. The M5400 and M5300 SFRA were both used for the SFRA measurements. The measurement frequency range was 10 Hz to 10 MHz. Figure 4.25 shows the admittance versus frequency of the tested transformers. The selected transformers were the most common sizes and types that were used in the Western Australian rural distribution network. Table 4.3 provides the simplified model parameters of the tested transformers.

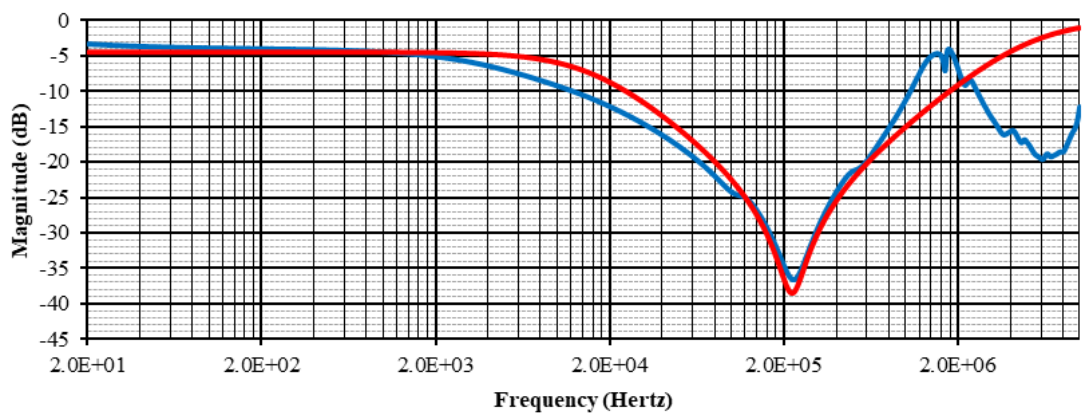
**Table 4.3. Simplified model parameter of single-phase single-wire earth-return transformers**

Item No.	Manufacturer	Nominal Power	Nominal Primary Voltage	Inductor (L)	Resistors		Capacitor (C)
					$R_1$	$R_2$	
		kVA	kV	H	k $\Omega$	k $\Omega$	pF
1	ABB	25	12.7	0.634	131.8	13.4	548
2	ABB	25	19	1.23	263.2	29.7	904



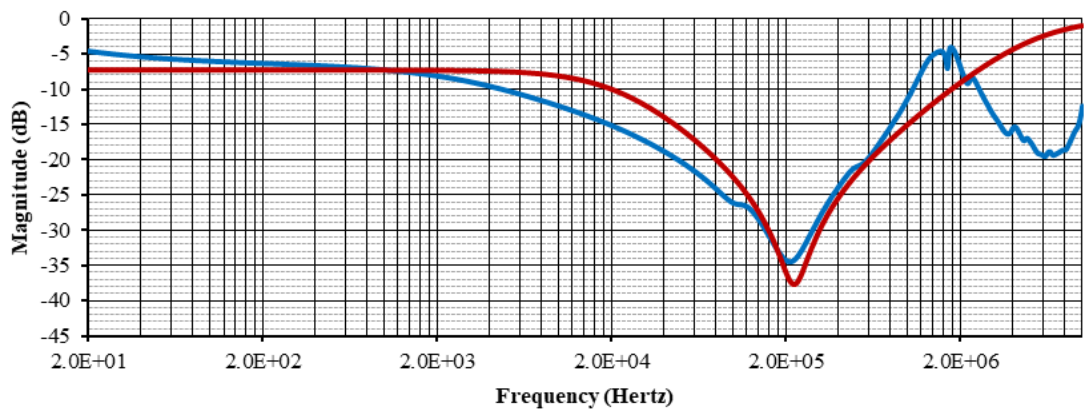
— Measurement — Simulation

(a)



— Measurement — Simulation

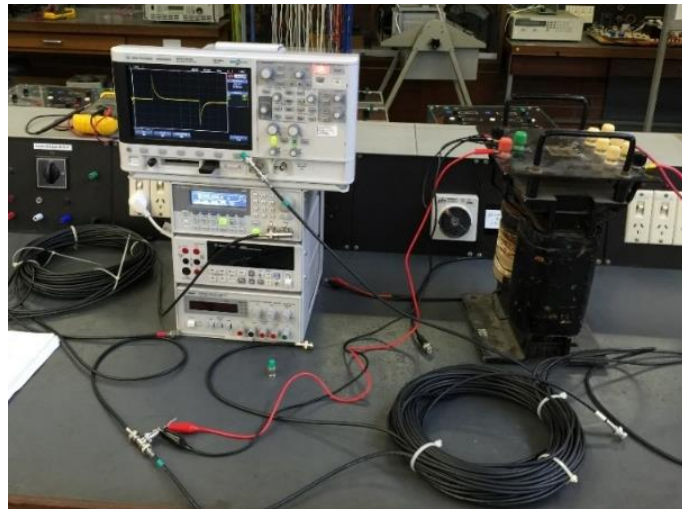
(b)



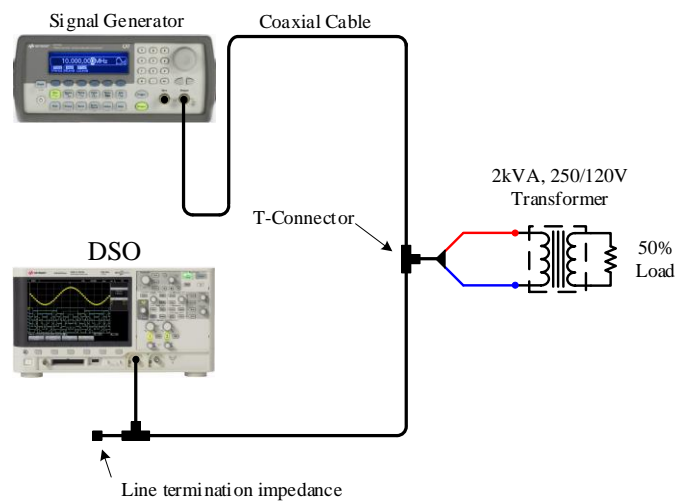
— Measurement — Simulation

(c)

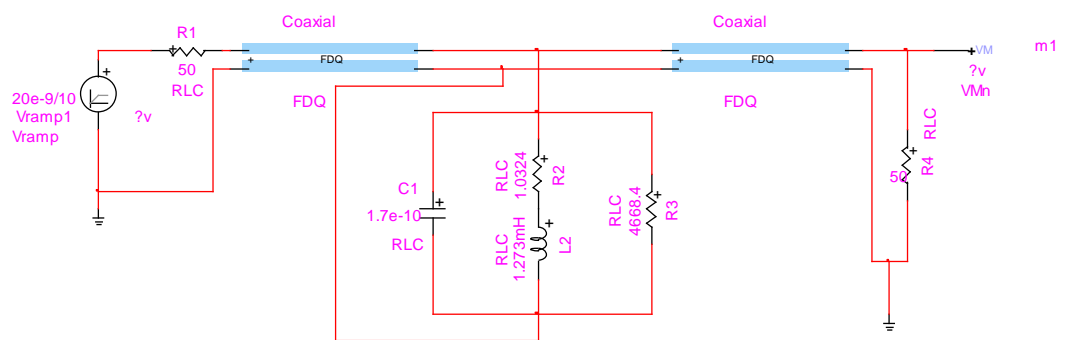
**Figure 4.22. Frequency response results from the simulation and measurements under (a) the short circuit; (b) 100% of the nominal load condition; and (c) 50% of the nominal load condition.**



(a)

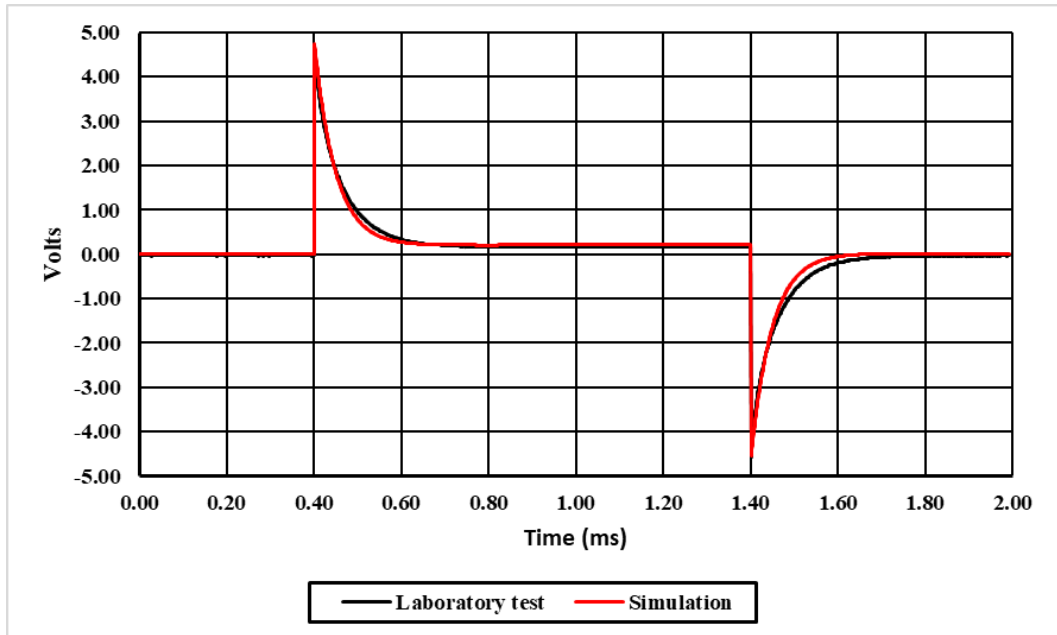


(b)

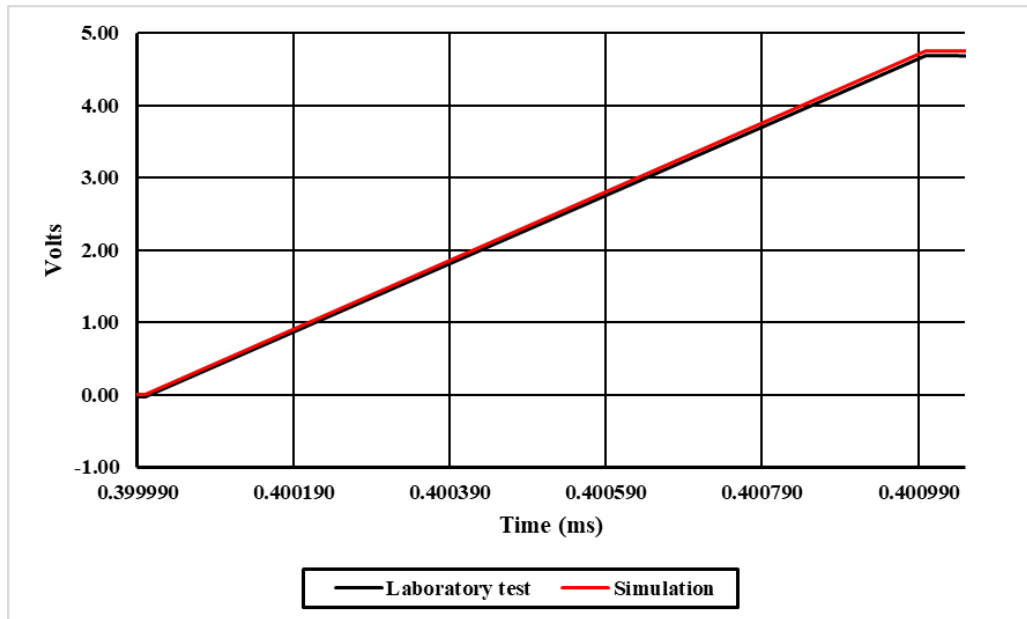


(c)

**Figure 4.23. The simulation model was verified: (a) the setup of the laboratory; (b) the schematic diagram for the test; and (c) the simulation circuit.**



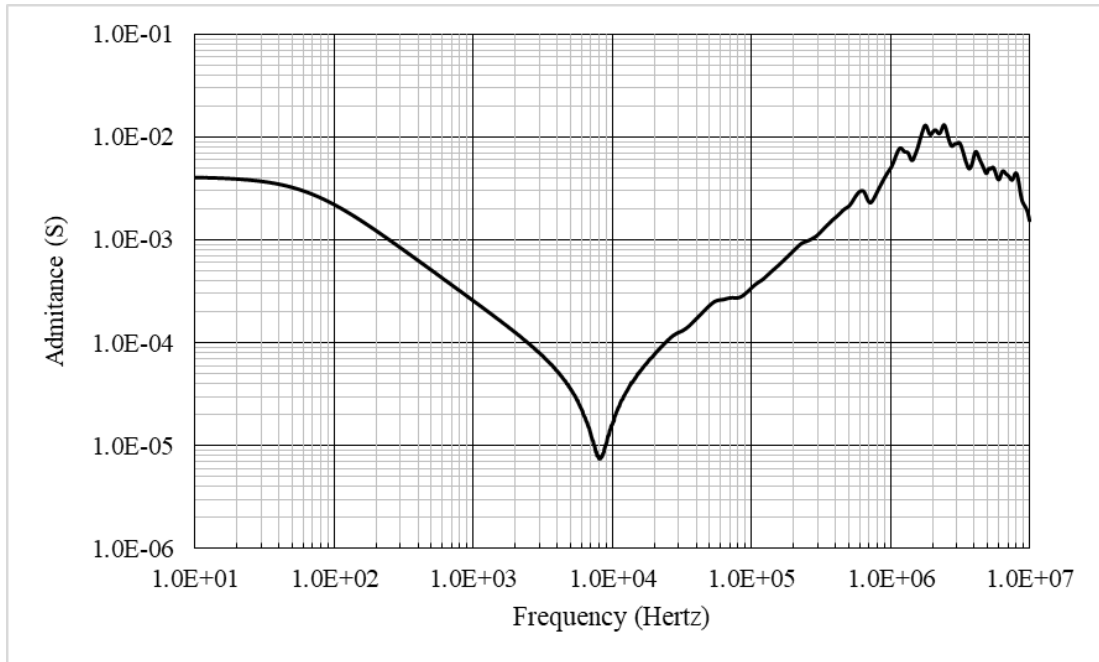
(a)



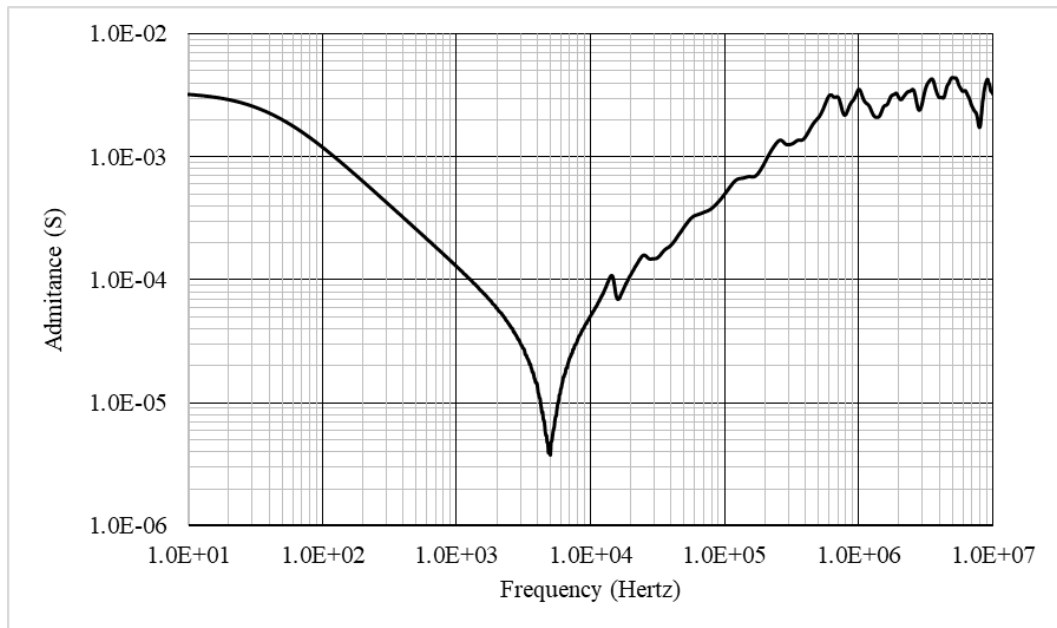
(b)

**Figure 4.24. Comparisons of the simulation and laboratory test results: (a) the recorded and simulated voltage across the termination impedance; and (b) close-up of the rising edge.**





(a)



(b)

**Figure 4.25. Results from the measured sweep frequency response analysis of common distribution transformers in the Western Australian network: (a) 25 kVA, 12.7/0.240 kV single-wire earth-return transformer; and (b) 25 kVA 19/0.240 kV single-wire earth-return transformer.**

In Australia, the HV winding of three-phase distribution transformers is commonly connected in a delta configuration. Figure 4.26 shows a simplified model of a three-phase transformer in a delta configuration. The  $R_1$  can be calculated from the self-admittance versus frequency of the HV terminal with the other phase terminals

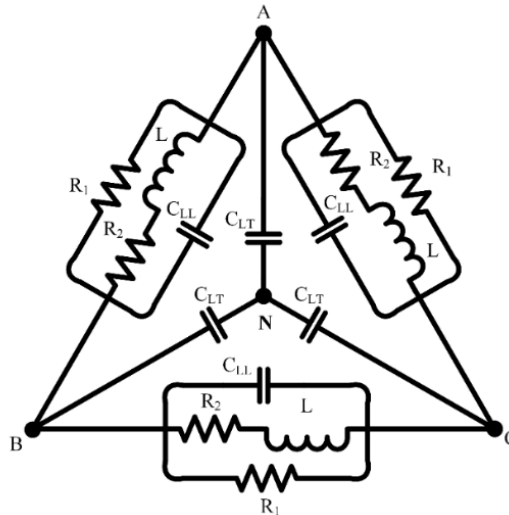


**Figure 4.26. A simplified model of a three-phase transformer in a delta configuration.**

earthed. The resistance of both the primary windings connected to the terminal are in parallel. Therefore, the calculated resistance should be doubled to obtain the  $R_1$ , and the calculated inductances should be doubled. The calculated capacitance from equation (4.19) is equal to:

$$C = C_{LT} + 2C_{LL} \quad (4.21)$$

Therefore, another measurement is required to determine the model capacitances. To obtain the  $C_{LT}$ , all the low voltage terminals should be grounded and the HV terminals should be connected. The capacitance to the ground of the grouped HV terminal and the ground will then be equal to  $3C_{LT}$ . The  $3C_{LT}$  and  $C_{LL}$  can be calculated from equation (4.20). This measurement could be performed by applying the sinusoidal voltage at a reasonably high frequency while measuring the current. The frequency should be selected centrally within the range of interest for the required model.

#### 4.5. Summary

This chapter proposes a high frequency transformer model for transient analysis. The simplified transformer model described in this chapter enables the study of travelling wave reflection and refraction at various junctions with distribution transformers. The proposed model is developed based on the frequency response analysis of the transformer. The model sufficiently represents the behaviour of the

distribution transformers under fast transient conditions, where it is simplified to reduce the complexity of the distribution network model.

# Chapter 5

## High impedance faults

### 5.1. Introduction

Contact between a bare conductor and a high impedance object or material, such as asphalt, sand, grass, gravel, concrete or tree branches creates a HIF [67]. A HIF in distribution networks often occurs when an overhead conductor breaks and falls to the ground or overgrown vegetation touches or grows close to the bare conductor. These instances cause an energised HV conductor to create step and touch potential hazards around the fault, which may threaten human life. Further, HIFs can ignite fires through a variety of mechanisms, such as direct ignition from high-energy arcs, molten or burning particles expelled from faults, burning or smouldering embers from vegetation, or the ignition and expulsion of insulating fluids common in power system apparatus [68]. Figure 5.1 shows the splash of a molten conductor and arcing caused by vegetation.

Although HIF arcs violently deliver substantial amounts of energy to fault points, the sustained currents are relatively small with regards to protection tripping. The HIF sustained current is usually lower than the normal load current of the feeder. Hence, HIFs cannot be detected by conventional protection means, which identify faults from the magnitude of their currents. The nature of a HIF and its characteristics are complex. A deep understanding of HIFs is required to develop an appropriate model for HIF protection studies. The complex nature of HIFs is apparent from their typical features, including:

- low current magnitudes

- arcing
- time-varying harmonic content
- nonlinear impedance characteristics
- asymmetry of fault current waveforms
- gradual current magnitude growth
- random characteristic changes [69-74].

Various high impedance models have been proposed over time to replicate the characteristics mentioned above.



(a)



(b)

**Figure 5.1. Contact events showing: (a) a down conductor ejecting molten particles; and (b) a vegetation-initiated arc [68].**

## 5.2. High impedance fault models

The Emanuel model was first introduced in 1990 and is based on a laboratory test [70]. In the Emanuel model, an arc is modelled with the help of two DC sources connected antiparallel by two diodes (see Figure 5.2(a)).

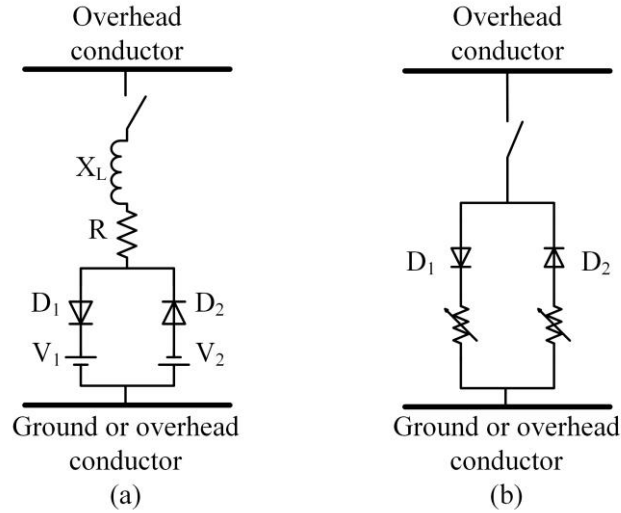


**Figure 5.2. Diagrams showing: (a) the Emanuel model; and (b) the modified Emanuel model.**

During the positive half cycle, the current flows through  $D_1$  and the arc ignition point is controlled by  $V_1$ . Similarly, in the negative cycle, the current flows through  $D_2$  and the arc reignition point is set by  $V_2$ . The second and third harmonics generated by the model are a function of  $\Delta V$  ( $\Delta V = |V_1 - V_2|$ ) and  $\tan \theta = X_L/R$ ;  $X_L$  is the arc column inductive reactance and  $R$  is the arc resistance. Emanuel defined the parameters  $V_1$ ,  $V_2$  and  $\tan \theta$  for a variety of surfaces from his experimental work [70].

The Emanuel model aims to represent the characteristics of the second and third harmonics resulting from an arc-to-ground fault. Sedighi and Haghifam introduced a different model (see Figure 5.2(b)) in which the resistance and inductance of the Emanuel model changes with two nonlinear resistances for considering the nonlinearity in earth impedance [75]. Further, Tat and Yibin developed a novel HIF model (see Figure 5.3) that uses several Emanuel arcs modelled together until the simulated HIF current resembles the real recorded HIF current [76]. Based on the arc theory, Zamanan and Sykulski proposed a HIF fault model to show a more realistic representation of HIF [77]. A realistic model of HIF embracing nonlinear impedance, time-varying voltage sources and transient analysis of a control system is shown in Figure 5.4 [78].

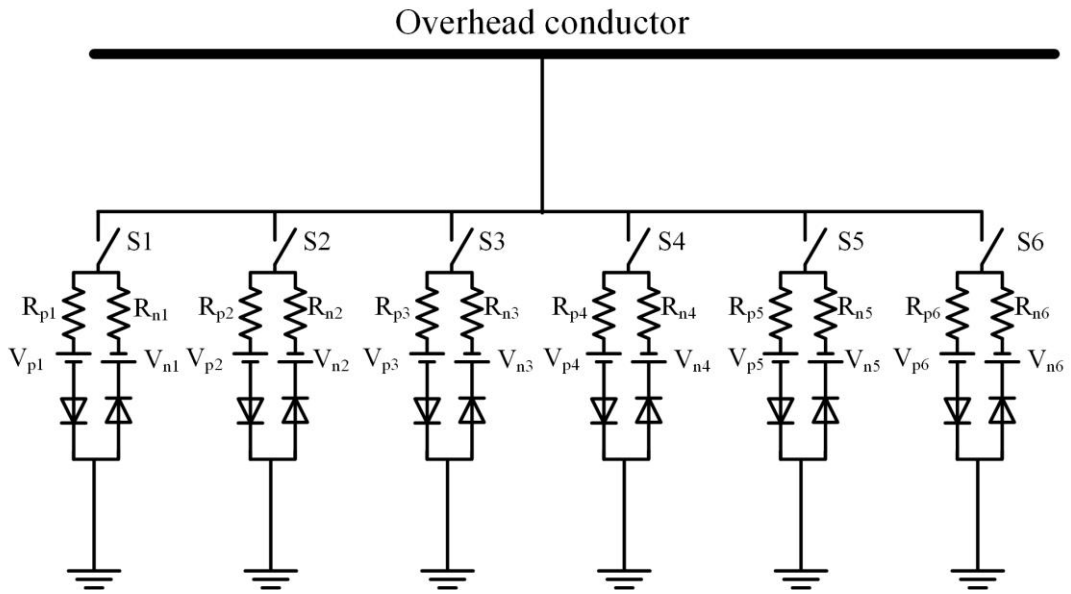


**Figure 5.3. A high impedance fault model using multiple Emanuel arc models [76].**

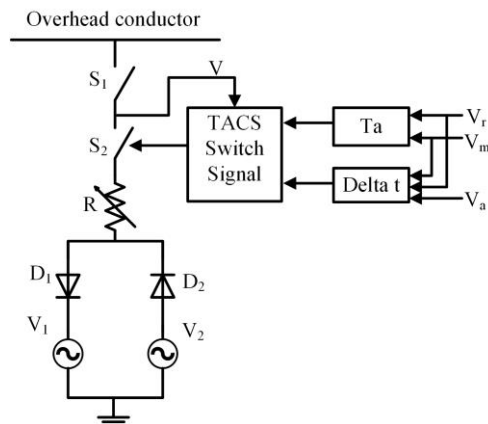


**Figure 5.4. A high impedance fault model based on arc features [78].**

Kizilcay and Pniok [79] and Michalik [80] introduced a model that contains two diodes and polarising ramp voltages to control the arc ignition instant (see Figure 5.5). The arc model consists of a linear resistor representing the ground path resistance, nonlinear time-varying resistor,  $r(t)$ , time-varying voltage and constant DC voltage source. In this model,  $r(t)$  represents the dynamic arc characteristic.

Kizilcay and Pniok stated that the arc model was adopted to obtain a dynamic feature of the ground fault nonlinear impedance [79]. Michalik used the Horchraimer equation to describe the dynamic behaviour of an arc, which is based on energy balance in the arc [80].

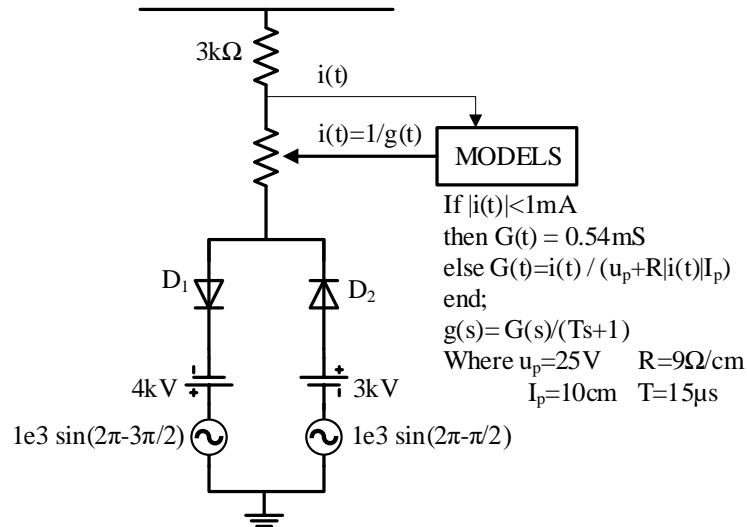


**Figure 5.5. A high impedance fault model considering the ignition instants [80].**

That is, arc conductance is related to the temperature inside the arc column that forms the discharge path [73]. This is written as:

$$\frac{dg(t)}{dt} = \frac{1}{\tau} (G(t) - g) \quad (5.1)$$

Where:

- $g$  is stationary arc conductance
- $G(t)$  is time-varying arc conductance
- $\tau$  is the time constant.

The solution to equation (5.1) in the time domain is:

$$G(t) = G_0(1 - e^{-t/\tau}) \quad (5.2)$$

Where  $G_0$  is the initial arc conductance.

Multiple studies have been conducted to determine the model parameters [69-71, 74, 79, 81]. These vary depending on the system's voltage level and the materials. When the current approaches zero at each cycle of the alternating current (AC) arc, the  $G(t)$  decreases due to heat loss and the temperature decreases inside the arc's discharge path. The conductance variation lags behind the current due to  $\tau$ . There is a delay between the current zero-crossing point and when the conductance reaches its lowest magnitude in the cycle. This delay causes the arc's persistence. The arc quenches and re-ignites at every half cycle.

Sharat et al. introduced a model that considered only the arc dynamics in series with the ideal switch (see Figure 5.6) [74]. The arc parameters were determined based on the experiment.



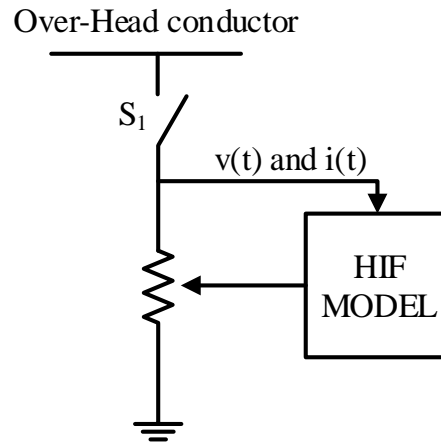


**Figure 5.6. The high impedance fault model proposed by Sharat et al. [74].**

### 5.3. Suggested high impedance fault model

Most models discussed in the literature aim to replicate the HIF characteristics after the initiation of a fault. These models are often used to investigate the performance of HIF detection techniques based on harmonics or lower-frequency randomness in arc currents. In this thesis, the HIF low-frequency characteristics are not a point of interest. Instead, the arc or fault initiation is the point of interest. Section 5.3 suggests the model that can reveal the instant at which the breakdown of a fault's path results in a sudden change of current; this sudden change will induce a TW.

When a conductive surface or material approaches a bare conductor, it will not initially establish a reliable electrical contact. The presence of a dielectric layer, narrow air gap or material surface oxides will initially impede the flow of current. Any available charge carriers, either ions or free electrons, will be accelerated by the electrical field formed between the conductor and the surface. When the kinetic energy of the charge carriers reaches a critical threshold, the neutral atoms in the discharge path will be ionised, releasing new free electrons and ions. Then, a process of successive collisions of electrons with neutral atoms will intensify within a very short time. The self-sustaining increase of free carriers and the discharge current is known as an avalanche discharge. As a result of this process, the dielectric layer will be punctured, and the discharge column will become a conductor, causing electric arcs [72].

The time that it takes for an arc current to rise from zero to its maximum is a function of the materials characteristics and external influences, such as gas pressure. In the air, this time will take a couple of nanoseconds [82, 83], and in air under

pressure, this process takes sub-nanoseconds the rapid increase of current results in a sudden release of energy at the point of contact. During the process of arc formation, the occurrence of scintillations and a bursting sound is common. This process may be repeated at every half cycle. However, the insulation breakdown may happen at a lower voltage and closer to the crossing point due to the increase in material temperatures. Because this process is relatively faster than a common simulation time step, it is reasonable to simulate the arc burst formation stage with an ideal switching action. Figure 5.7 shows the suggested HIF burst ignition model for this thesis, which simulates the arc burst ignition only. This model is sufficient to study the performance of the TW fault location algorithm.

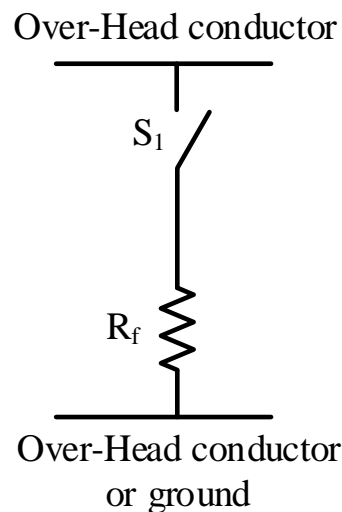


**Figure 5.7. The suggested high impedance fault burst ignition model.**

The resistance ( $R_f$ ) is the total resistance of the current path, including the initial arc and ground resistance. HIFs typically produce currents smaller than 75 A [74]. The  $R_f$  is the function of the arc's length, system voltage, power system grounding, dielectric material, and ground resistance.

Fault resistances that are in the range of the line's characteristic impedance introduce significant voltage TWs. A rural overhead line will have a characteristic impedance of approximately 360  $\Omega$  to 380  $\Omega$ . The fault resistance forms a voltage divider with the line's characteristic impedance occurring at the instant of the fault's inception. The travelling voltage wave has a magnitude equal to the voltage drop. A fault resistance equal to the characteristic impedance launches a TW with a magnitude of half the pre-fault voltage. Faults with resistances of hundreds of ohms will launch significant TWs.

#### **5.4. Summary**

The behaviour of high impedance faults is very complex. In order to understand this behaviour, various high impedance models are reviewed in this chapter. The various high impedance fault models suitability for travelling wave studies is investigated. The chapter is concluded by selecting a suitable high impedance fault model for travelling wave studies.

## Chapter 6

# Travelling wave arrival time detection techniques

### 6.1. Introduction

The sudden change of a power line's state variable launches a TW, which propagates in all directions from the disturbance location. A fault-induced TW appears as a step-like signal. The magnitude of the TW is determined by the degree of disturbance in the power line's state variables. The relative ratio of the line's characteristic impedance to the fault's impedance determines the relative disturbance. Given that distribution overhead line impedances are typically near  $380 \Omega$ , HIF faults can produce relatively strong TWs. For example, a 22 kV fault with an impedance equal to the characteristic impedance of  $380 \Omega$ , which corresponds to a 34 A earth fault, still produces a TW with a magnitude equal to half the line voltage at the time of the fault's inception.

Although TWs can have significant initial magnitudes, the rising edge rate will slow as the wave travels, and higher-frequency components are attenuated. TWs also reflect and refract at discontinuities. There is a real potential that TWs arriving at a detector will be heavily attenuated. Such a weak TW is difficult to detect with the presence of high interference noise. Precise time-stamping of the incident wave's arrival at the observer location is the most fundamental step for estimating a fault's location. The fault associated signal is superimposed on the power frequency as a high-frequency component. The arrival time is when a fault-induced high-frequency

component arrives at an observer location. Many time-frequency signal-processing techniques can be used to detect TW arrival times. Few techniques are suitable for practical application due to the calculation burden. In Chapter 6, various signal processing techniques are investigated concerning their application to detect and time-stamp voltage TWs.

## 6.2. Signal processing techniques

### 6.2.1. Differences and approximate derivatives

The first derivative of a signal is interpreted as the slope of the tangent to the signal at each point. This provides the signal's rate of change at each instant. The rate of change of a TW's leading edge is significantly higher than the voltage or current at the power frequency. The first-order derivative of the signal has been used in radar technology for tracking the leading edge of reflected signals [84]. The first-order derivative was used in an HV DC line's fault locator [85]. The first derivative of the voltage signal from calculus can be written as a limit:

$$v'(t_0) = \left. \frac{dx}{dt} \right|_{t \rightarrow t_0} = \lim_{t \rightarrow t_0} \frac{v(t) - v(t_0)}{t - t_0} \quad (6.1)$$

An interpolating polynomial can find the estimates for derivatives of discrete signals among a set of discrete values [86]. This estimate is not as dependable as when the time domain signal is approximated. Differentiation is known to cause problems and unstable processes; a signal with a minor amount of noise can lead to wild variations in the output signal. The standard approach to this problem is to use a low-pass filter to smooth the waveform and remove high-frequency components above the frequency ranges of interest [31].

A three-stage discrete finite impulse response filter can be considered. A general finite impulse response filter operation based on three sample observations can be expressed as:

$$\Delta V_n = \mathbf{H} \mathbf{V} = [h_1, h_2, h_3] \begin{bmatrix} V_{n-2} \\ V_{n-1} \\ V_n \end{bmatrix} \quad (6.2)$$

Where  $V_n$  is the  $n^{th}$  sample and vector  $\mathbf{H}$  contains the sample weighting factors that determine the impulse response. The system with an impulse response of  $\mathbf{H} = [-1/2, 0, 1/2]$  approximates the discrete first derivative. Conversely,  $\mathbf{H} = [1, -2, 1]$  approximates the discrete second derivative. A second difference reveals abrupt

changes in signal and produces a zero response within flat and linearly sloped signal regions [29]. The use of a twice-delayed sample to calculate the derivative provides a 50% reduction in the influence of random noise. For Gaussian noise, the noise component in each sample is the same. The time doubles, reducing the noise effect after divisions. However, noises in the sampled signal can still lead to wild variations in the derivative estimations.

### 6.2.2. Discrete wavelet transformed spectral energy

Wavelet transform methods are well suited to detecting TW arrival times [87]. Wavelet transform is based on a multi-resolution analysis that uses small time windows for higher frequencies and longer time windows for lower frequencies [88]. This is suitable for non-stationary signals like the TW transients [29]. The term wavelet refers to a ‘small wave’ [88]. A signal must satisfy two conditions to be considered a wavelet: (i) its oscillation magnitude should decay quickly to zero; and (ii) it must have an average value of zero [29]. The digitally implemented wavelet transform is called the discrete wavelet transform (DWT). Only DWT will be discussed in Chapter 6. The continuous wavelet transform is not suitable for analysing signals in a digital signal processor environment. The DWT of a sampled waveform is given by:

$$DWT(k, n, m) = \frac{1}{\sqrt{a_0^m}} \sum_n x[n] \psi\left(\frac{k - nb_0 a_0^m}{a_0^m}\right) \quad (6.3)$$

The transformed signal is a function of the variables  $a_0^m$  and  $b_0$ , which are the scaling and translation parameters, respectively. The  $a_0^m$  and  $b_0$  are fixed constants, and  $a_0^m > 1$ ,  $b_0 > 0$  and  $m, n \in Z$ . The factor  $\frac{1}{\sqrt{a_0^m}}$  is used to ensure each scaled wavelet function has the same energy as the wavelet basis function [29], where the basis function is expressed with a discrete variable such that:

$$\psi(t) = a_0^{-m/2} \psi\left(\frac{k - nb_0 a_0^m}{a_0^m}\right) \quad (6.4)$$

The  $\psi(t)$  is the mother wavelet. There are various classes of wavelet-based functions, including the Haar, sinc, Daubechies, spline, Battle-Lemarie and Meyer functions [89]. Some wavelets have a better correlation with fault-induced TWs and can detect arrival times more accurately. The Daubechies, Coiflets, symlets, and biorthogonal wavelets were considered for fault-induced TW arrival time detection by Mallat [90]. Efficient implementation of DWT involves passing the signal ( $x[n]$ )

through a pair of high- and low-pass filters with various scaling factors [89, 91]. The first scale will have the highest time resolution and the higher scales will have a lower time resolution. DWT uses the low-pass mother wavelet ( $H[n]$ ) and its related half band high-pass filter ( $G[n]$ ) [92]. According to Nyquist's rule, after each step, the highest frequency of the signal is  $f/2$  instead of  $f$ , and after each step, the signal can be down-sampled by two [47]. The structure of the one-level DWT algorithm is shown in Figure 6.1.

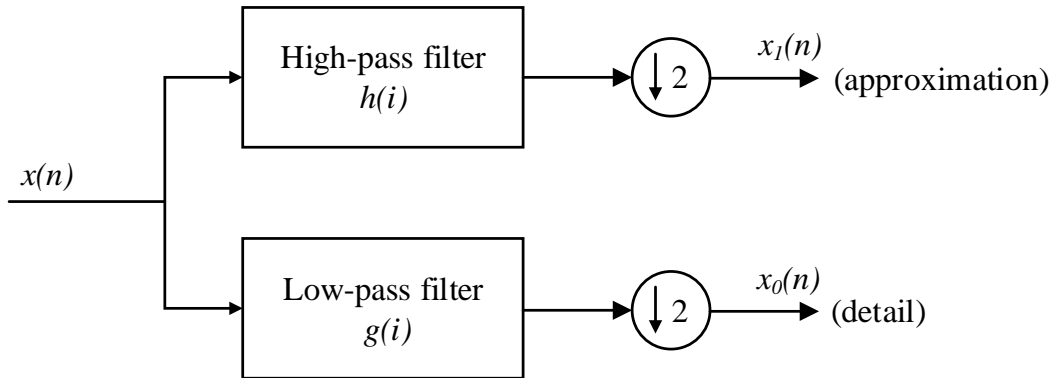


**Figure 6.1. The structure of the one-level discrete wavelet transform.**

The signal ( $x_0[n]$ ) is a smoothed version of the input signal, while the  $x_1[n]$  on the output of the high-pass filter contains only the higher-frequency residual [47]. The details and approximation signal result from the following equations:

$$x_1(n) = \sum_{k=0}^{M-1} h(2n - k)x(k) \quad (6.5)$$

$$x_0(n) = \sum_{k=0}^{M-1} g(2n - k)x(k) \quad (6.6)$$

Where  $h(2n - k)$  is the impulse response of the high-pass filter and  $g(2n - k)$  is the impulse response function of the low-pass filter. The impulse response relation is defined as:

$$h(M - 1 - k) = (-1)^k g(k) \quad (6.7)$$

Where  $M = 2L$  defines the filter window length [93], and  $L$  is the wavelet level.

For TW arrival time detection, transients are detected faster using the wavelet coefficients of the maximal overlap DWT (MODWT) than the DWT [94]. The MODWT is also known as the stationary wavelet transform [95]. It is a redundant scheme because the output of each level of the MODWT contains the same number of samples as the input. There is a redundancy of  $N$  in the wavelet coefficients for

decomposition of the N-level in the MODWT. The structure of the one-level MODWT algorithm is shown in Figure 6.2.

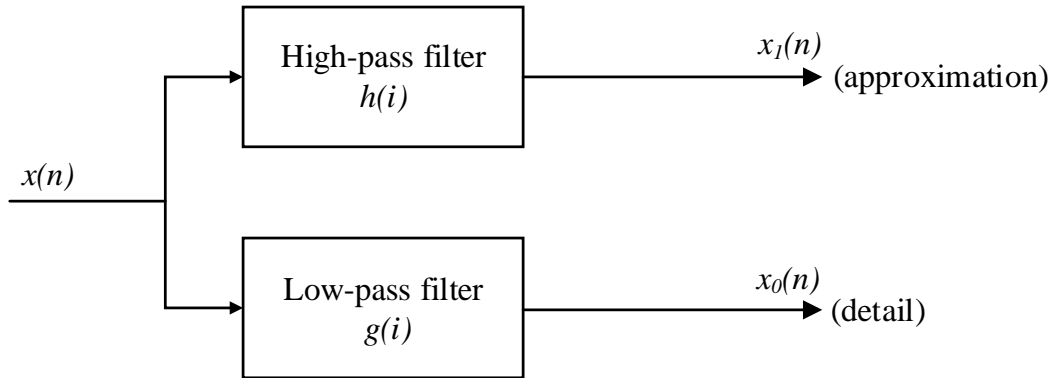


**Figure 6.2. The structure of the one-level maximal overlap discrete wavelet transform.**

### 6.2.3. Boundary wavelet transform

Like all other methods, wavelet-based techniques have advantages and limitations. The performance of wavelet methods is highly dependent on the chosen wavelet. Percival and Walden [94] proposed a boundary DWT method for the real-time detection of fault-induced transients, which was based on methodology presented by Costa et al. [96] where the wavelet energy coefficient accounts for the border effects of sliding windows. The performance of the proposed arrival time detection methods that are based on the boundary wavelet transform is scarcely affected by the chosen wavelet.

In a study by Costa, the boundary maximum overlaps discrete wavelet transform (BMODWT) method was demonstrated as a powerful tool for detecting over-damped signals induced by HIFs in distribution networks [97]. The first-level boundary wavelet coefficient was defined as a convolution process between the wavelet filter ( $\tilde{h}$ ) and circular sliding windows with a length ( $\Delta k$ ) [97]:

$$\omega(l, k) = \sum_{n=0}^{L-1} \tilde{h}(n)x(k - L + n + 1 + l) \quad (6.8)$$

Where  $0 \leq l < L$ ,  $L \leq \Delta k$  and  $k \geq \Delta k - 1$ . Notably,  $\omega(0, k) = \omega(k)$  is equivalent to the wavelet coefficient from the conventional DWT, whereas  $\omega(l, k)$  and  $l \neq 0$  are the boundary wavelet coefficients [98]. The first scale one-cycle wavelet energy coefficient ( $\varepsilon^\omega$ ) can be defined as [94, 97, 98]:



$$\varepsilon^\omega(k) = \varepsilon^{\omega^a}(k) + \varepsilon^{\omega^b}(k) \quad (6.9)$$

Where  $k \geq N - 1$ , and  $N = f_s/f$  is the length of the window. The  $\varepsilon^{\omega^a}$  is the energy component with a border distortion, given by [94, 97]:

$$\varepsilon^{\omega^a}(k) = \sum_{l=1}^{L-1} \omega(l, k) \quad (6.10)$$

The  $\varepsilon^{\omega^b}$  is defined as follows:

$$\varepsilon^{\omega^b}(k) = \sum_{n=k-\Delta k+L-1}^{L-1} \omega(0, k) \quad (6.11)$$

During the steady-state condition,  $\varepsilon^\omega$  is approximately equal to  $\varepsilon^{\omega^b}$  because there are no border distortions when using one-cycle windows. However, when the transient is present, border distortions are presented in the  $\varepsilon^{\omega^a}$ . Therefore, the  $\varepsilon^\omega$  presents the same features of  $\varepsilon^{\omega^b}$  with an additional increase in energy from the transient. Costa proposed a high impedance detection technique using the  $\varepsilon^\omega$  of the recorded current [97]. The study demonstrated that the technique was not sensitive to the selected mother wavelet. The boundary wavelet coefficient is capable of detecting the current transient created from a HIF faster and more accurately than the MODWT. However, it would be challenging to implement this for the detection of online TW arrival. Accurate fault location based on TW arrival time requires a higher sampling rate than the HIF detection, and higher sampling rates require a larger circular buffer.

### 6.3. Dealing with multiphase lines

In multiphase transmissions or distribution systems, the phases have significant electromagnetic coupling between conductors, and therefore, a single TW does not exist [99]. Single transients introduce multiple TWs that travel at different speeds. The measured voltage waveforms are initially converted to their modal components to precisely estimate the location of faults [51].

#### 6.3.1. Clarke's transformation

Clarke's transformation was used to simplify the analysis of the three-phase circuits by decomposing the phase voltage and current to their modal components. The modal components are not mutually coupled together, and this simplifies the analysis. Clarke's transformation matrix is given by:

$$T = \frac{1}{3} \begin{bmatrix} 1 & 1 & 1 \\ 2 & -1 & -1 \\ 0 & \sqrt{3} & -\sqrt{3} \end{bmatrix} \quad (6.12)$$

The phase voltages are transformed into their modal components as in the following:

$$\begin{bmatrix} V_0 \\ V_1 \\ V_2 \end{bmatrix} = T \begin{bmatrix} V_a \\ V_b \\ V_c \end{bmatrix} \quad (6.13)$$

Where  $V_a$ ,  $V_b$  and  $V_c$  denote the phase voltages.

The first mode ( $V_0$ ), is usually referred to as the ground mode, and  $V_1$  and  $V_2$  are the aerial mode voltages. The ground mode magnitude is significant only during faults that include a ground [99]. However, the aerial mode is present for any fault. To detect the TW arrival time,  $V_1$  or  $V_2$  are processed using the appropriate signal processing techniques. The distribution lines are not transposed and therefore, cannot be decomposed to uncoupled components using Clarke's transformation. For the untransposed circuit, an eigenvector-based transformation matrix (which is frequency-dependent) must be used. However, to detect TW arrival times, the error from ground or aerial mode is acceptable. Therefore, it is reasonable to assume that the lines are fully transposed and that Clarke's transformation can be used.

### 6.3.2. *Park's transformation*

Park's transformation was presented by Park in 1929 [100]. Park's transformation, or direct-quadrature-zero transformation, produces a tensor that rotates in a reference frame. Lopes et al. suggested a simple method for transient arrival detection through the application of Park's transformation [101]. Such methods permit the monitoring of the three-phase signals simultaneously by the analysis of only the direct axis signal [102]. Lopes et al. proposed an algorithm based on Park's transformation that improved the technique and made it less sensitive to electrical noises [103]. For transient detection, the Park's transformation is used to generate a rotating reference frame synchronised with a voltage phasor at the power frequency ( $\omega$ ). The steady-state portion of the direct axis has negligible value. When a disturbance arrives at the observer, large waveform variations appear, enabling transient detection. Direct-quadrature-zero methods also detect sudden changes in phase imbalances due to faults. This differs from conventional TW arrival detection methods, where the beginning of the disturbance is found by identifying the high-frequency components. These features make direct-quadrature-zero useful for

HIFs induced detection of TW arrival times in distribution networks, where fault-induced transients attenuate significantly.

The direct axis and quadrature axis components are called  $A_d$  and  $A_q$ , respectively, and are computed as:

$$\begin{bmatrix} A_d(n) \\ A_q(n) \end{bmatrix} = \mathbf{P}_{dq} \cdot \begin{bmatrix} A_a(n) \\ A_b(n) \\ A_c(n) \end{bmatrix} \quad (6.14)$$

or

$$\mathbf{A}_{dq} = \mathbf{P}_{dq} \cdot \mathbf{A}_{abc} \quad (6.15)$$

This gives:

$$\mathbf{P}_{dq} = \frac{2}{3} \cdot \begin{bmatrix} \cos(\varnothing) & \cos(\varnothing - \frac{2\pi}{3}) & \cos(\varnothing + \frac{2\pi}{3}) \\ -\sin(\varnothing) & -\sin(\varnothing - \frac{2\pi}{3}) & -\sin(\varnothing + \frac{2\pi}{3}) \end{bmatrix} \quad (6.16)$$

Where:

- $n$  is the  $n$ th signal sample.
- $A_{abc}$  is the monitored three-phase voltage.
- $A_d$  is the direct-quadrant reference frame component.
- $\varnothing = n\omega\Delta t + \theta$ ,  $\omega$  is the angular power frequency.
- $\Delta t$  is the sampling interval.
- $\theta$  is the angle of the direct component and the reference axis.

The behaviour of the  $A_d$  can be monitored to detect a TW's arrival time. The  $A_d$  enables transient detection irrespective of the type of fault [103]. It provides the same information as aerial mode voltages in Clarke's transformation.

#### 6.4. Detection criteria

Faults and HIFs generate TWs that are potentially highly attenuated in distribution networks. Regardless of the signal processing methods used, it is challenging to distinguish TW signals from noise and disturbances. The signal sliding window technique has been used to overcome this challenge and minimise error due to electrical noises [94, 103]. The signal sliding window energy is defined as:

$$\xi(k) = \sum_{n=k-M+1}^k D(n)^2 \quad (6.17)$$

Where:

- $\xi(k)$  is the energy of the  $n$ th data window.
- $M$  is the number of samples within a half cycle of the power frequency.
- $D(n)$  is  $n$ th sample of the processed signal.

The  $D(n)$  can be the output of any signal processing technique discussed in subsection 6.2.

### 6.5. Thresholding

Thresholding aims to select an appropriate threshold window to detect the fast-rising edge of energy,  $\xi(k)$ . The  $\xi(k)$  translates to the TW's arrival time at the relay point. Several fault detection algorithms that are based on hard thresholding were described by He et al. [104].

If noise disturbances are truly random, or white in spectral terms, they can be modelled using the Gaussian distribution. According to the Gaussian probability distribution theory, it is possible to find the  $\sigma_\xi$  that 99.73% of the  $\xi$  falls into the range  $[\mu_\xi - 3\sigma_\xi, \mu_\xi + 3\sigma_\xi]$ . Therefore, during a steady-state condition, the noise-related components of the signal energy,  $\xi(k)$ , can be expected to remain inside the range  $[\mu_\xi - \rho_\xi, \mu_\xi + \rho_\xi]$ ; where  $\mu_\xi + \rho_\xi$  is the steady-state upper threshold and  $\rho_\xi > 3\sigma_\xi$ . The steady-state period can then be identified when:

$$\xi(k) \leq \mu_\xi + \rho_\xi \quad (6.18)$$

A TW's arrival time is detected when:

$$\xi(k) \geq \mu_\xi + \rho_\xi \quad (6.19)$$

Hard thresholding is very sensitive to changes in background electrical noise, and the appropriate threshold ( $\rho_\xi$ ) will change over time if the electrical noise environment changes. Therefore, the reliability of detecting the TW's arrival time could be compromised by selecting a fixed  $\rho_\xi$ .

To avoid this problem, Lopes applied a self-adaptive approach where the 'energy sensitivity factor' ( $E_{sf}$ ) was updated whenever the monitored system was at steady state [103].  $E_{sf}$  represents the ratio between the global maximum and the global minimum values picked up in a  $\xi$  data window with a programmable length  $\Delta E_{SF}$ :

$$E_{sf} = \frac{\max\{\xi(k)\}}{\min\{\xi(k)\}}, \text{ for } 1 \leq k \leq \Delta E_{SF} \quad (6.20)$$

Where  $k$  represents the  $k$ th sample index of the ,  $\max\{\}$  and  $\min\{\}$  are functions for calculating the global maximum and minimum values of  $\xi$  over the period of  $\Delta E_{SF}$ .

## 6.6. Arrival time detection procedures

TWs propagate in overhead lines with a velocity close to the speed of light or approximately  $300\text{ m}/\mu\text{s}$ , and the sampling rate should be significantly higher than 1 MHz to achieve a 300 m accuracy. For rural overhead lines, this is approximately the span length where one span is considered to have a good locational performance. The high-performance methods proposed by Costa [97] to detect high impedance induced transients and the self-adaptive thresholding proposed by Park [103] rely on a repetitive average energy calculation over the sliding window for every sample. The recommended length of a sliding window is one cycle. This is equal to 40,000 samples per cycle, at a sampling rate equal to 2 MHz.

Implementing such a resource-demanding calculation would be challenging, even for a frequency range of kilohertz. This study aims to develop relatively low-cost hardware. Therefore, a simpler approach is recommended with hard thresholding. Due to the simplicity, the system could be sensitive to noise. However, regardless of the TW detector methods that are used, the transient classification algorithm requires post-processing of the recorded transient. Even normal feeder events, such as capacitor switching, could initiate significant TWs.

A transient classification algorithm is presented in the literature that distinguishes fault transients from other feeder activity [56, 105-113]. The classification of transients is beyond the scope of this study. For this thesis, it is assumed that transients can be successfully classified after they have been detected. The stages of the computational section from the recommended method are shown in Figure 6.3, which is based on Korkali's method [51]. The expected waveform from each step is shown in Figure 6.4. Figure 6.4(a) demonstrates the simulated sampled three-phase voltages that contain the high-frequency transient. Figure 6.4(b) presents the correspondence voltage of the aerial mode. Figure 6.4(c) shows the wavelet coefficient energy ( $WTC^2$ ). For the threshold value,  $(\mu_{\xi} + \rho_{\xi})$  is equal to  $5 \times 10^{-5}$ , the arrival time is equal to 0.005041 s.

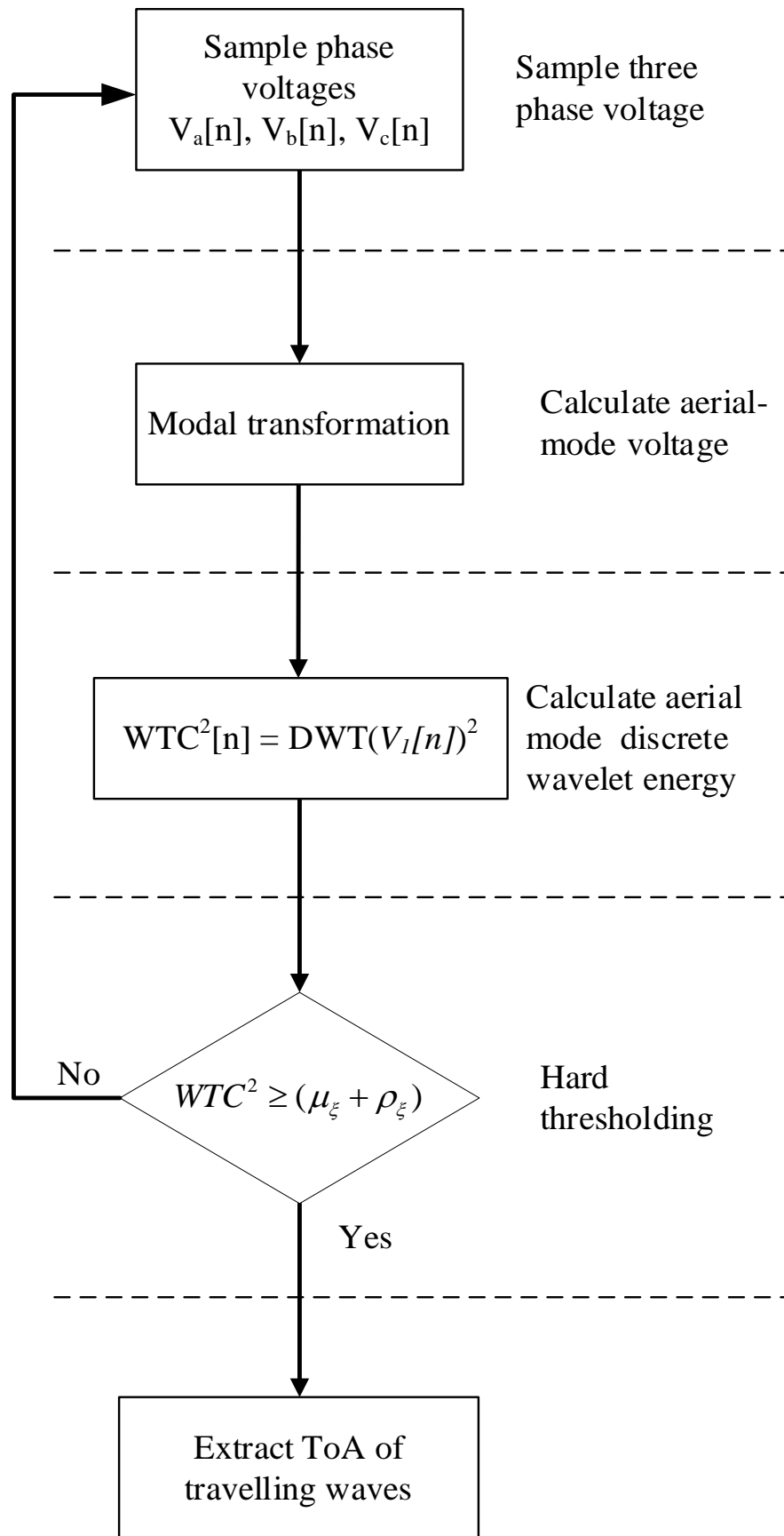
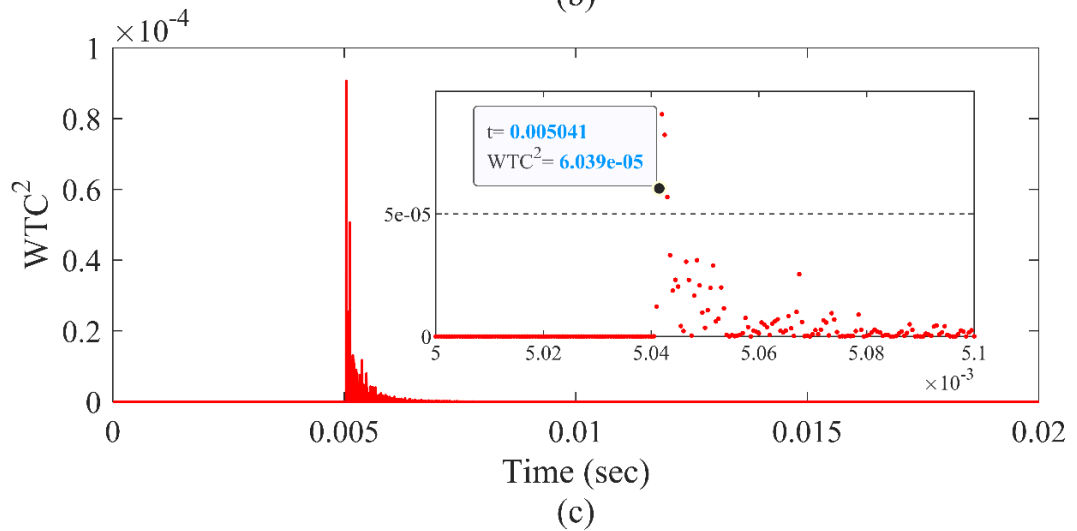
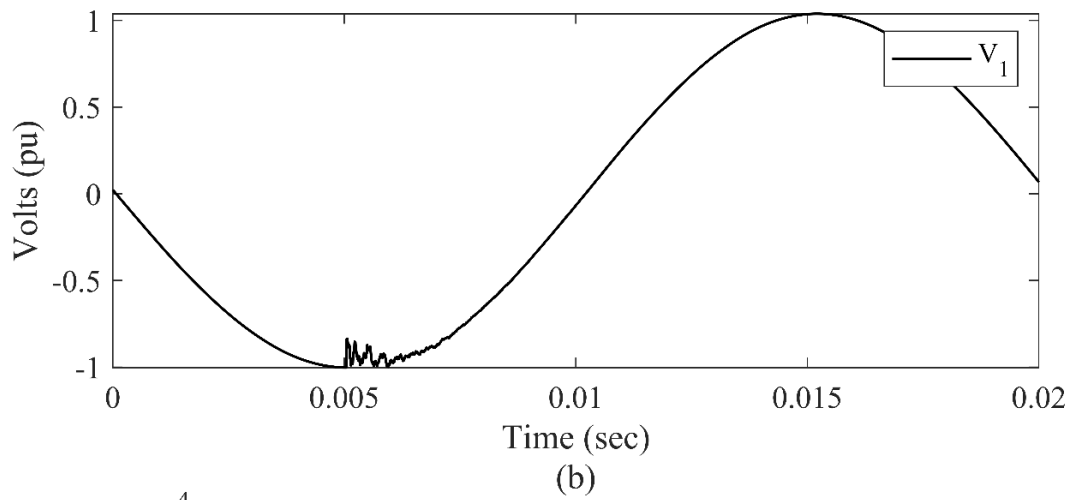
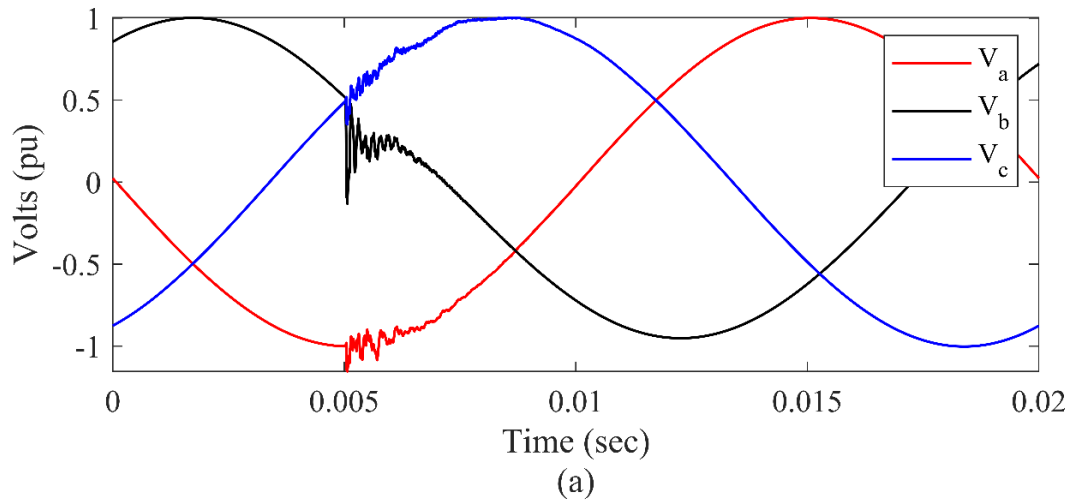


Figure 6.3. The computational stages of a travelling wave arrival time-stamp.



**Figure 6.4. The expected waveform from each step, showing: (a) the samples phase voltages; (b) the calculated aerial mode voltages; and (c) the wavelet energy coefficient.**

## **6.7. Summary**

Given the importance of the accurate detection of the travelling wave arrival time, this chapter highlights the steps and signal processing techniques required to time stamp the travelling wave arrival time at the observer point.



## Chapter 7

# Travelling wave-based fault location for radial distribution networks

*Content of this chapter is published in the IEEE Transactions on Power Delivery, vol. 35, no. 3, pp. 1553-1562, June 2020, doi: 10.1109/TPWRD.2019.2948174.*

### 7.1. Introduction

Fault location on transmission systems using TWs has become a well-developed and successfully commercialised technology. However, distribution networks have more complex topologies than transmission networks and feature many laterals and load taps. Therefore, fault location is much more complicated than on transmission systems. On a transmission system, TWs propagate freely towards the ends of the line and over many kilometres. Conversely, there are numerous junctions and load taps along the length of a relatively short distribution line [114], which present many points for partial reflection.

The existence of multiple laterals and bifurcation points in a distribution network necessitates synchronised measurements at selected locations and complex calculations to determine the locations of faults. A relatively low-cost TW detector [115] allows several detectors to be easily incorporated into existing systems to provide synchronous TW voltage observations. Robson et al. presented a method based on time-stamping TWs at each branch termination in a radial distribution network [9]. The desired accuracy was achieved by dividing the networks into smaller sections that were shorter than the desired accuracy by using virtual nodes [9]. This

increased the complexity and required calculations. Previously, Korkali and Abur demonstrated that multiple synchronised measurements from selected buses could be used for fault location in a meshed transmission grid [10]. In Chapter 7, a fault location method based on time-stamping the arrival time of TWs is proposed for radial feeder distribution networks. This is in contrast to the approach used by Robson et al., where the accuracy and complexity of locating the fault depended on the chosen resolution [9]. Chapter 7 investigates the performance and uncertainty of the proposed method using the Monte Carlo analysis.

## 7.2. Proposed fault location method

When  $N$ -detectors, which are independently measuring the time of arrival (ToA) of a voltage TW launched by an electrical fault, are deployed in a distribution network, the location of the fault can be determined from a set of ToAs ( $\{T_n; 1 \leq n \leq N\}$ ). Because the travelling time is the point of interest (instead of the line's length), a set of travelling times ( $\{T_l; 1 \leq l \leq L\}$ ) can be computed for a given network with  $L$  distribution lines. The set of a line's propagation times ( $\{T_l\}$ ) is the set of a theoretical TW's propagation times from the line's origin to its terminus (see Figure 7.1).

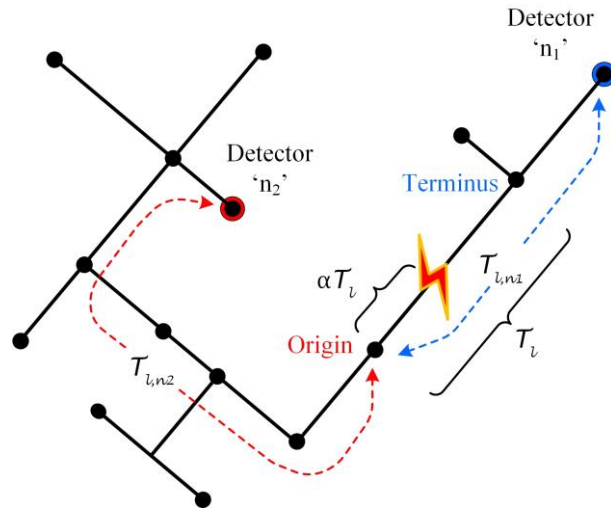


**Figure 7.1. The propagation delay:  $T_l$ ,  $T_{l,n_1}$  and  $T_{l,n_2}$ .**

Considering Figure 7.1, the travelling time to detector 'n' from a fault occurring on line 'l' is equal to:

$$T_{l,n} + S_{n,l} \alpha^{(l)} T_l \quad (7.1)$$

Where  $T_{l,n}$  is the travelling time from the origin of the line (' $l$ ') to detector ' $n$ ' and  $\alpha T_l$  is the propagation delay from the fault location to the origin of the ' $l$ '.  $\alpha$  defines the fault's location from the ' $l$ ' origin as a fraction of the line length and  $0 \leq \alpha \leq 1$ .  $S_{n,l}$  is equal to  $-1$  if the closer path to detector ' $n$ ' is included the ' $l$ ' terminus or  $S_{n,l}$  is equal to  $+1$  if it is not included the ' $l$ ' terminus.

By using equation (7.1), the arrival time difference between detectors  $n_1$  and  $n_2$  is  $\Delta T_{n_2,n_1}^{(f)}$ . For the fault occurring at  $\alpha T_l$ , this can be expressed as follows (assuming  $T_{l,n_1} < T_{l,n_2}$ ):

$$\Delta T_{n_2,n_1}^{(l)} = (T_{l,n_2} - T_{l,n_1}) + (S_{n_2,l} - S_{n_1,l}) \alpha T_l \quad (7.2)$$

The system of equations can be obtained for a fault's location by exchanging the theoretical time differences ( $\Delta T_{n_2,n_1}^{(l)}$ ) with the measured time differences ( $\Delta T_{n_2,n_1}^m$ ).

The equation that needs to be solved is:

$$\Delta \mathbf{T}_{n_n,n_i}^{(l)} + \mathbf{S}_{n_n,n_i}^{(l)} \alpha^{(l)} T_l - \Delta \mathbf{T}_{n_n,n_j}^m = 0 \quad (7.3)$$

Where:

$$\Delta \mathbf{T}_{n_n,n_i}^{(l)} = \begin{pmatrix} T_{l,n_1} - T_{l,n_i} \\ T_{l,n_2} - T_{l,n_i} \\ \vdots \\ T_{l,n_N} - T_{l,n_i} \end{pmatrix} \quad (7.4)$$

$$T_{l,n_i} = \min(T_{l,n_1}, T_{l,n_2}, \dots, T_{l,n_N}) \quad (7.5)$$

$$\mathbf{S}_{n_n,n_i}^{(l)} = \begin{pmatrix} S_{l,n_1} - S_{l,n_i} \\ S_{l,n_2} - S_{l,n_i} \\ \vdots \\ S_{l,n_N} - S_{l,n_i} \end{pmatrix} \quad (7.6)$$

$$\Delta \mathbf{T}_{n_n,n_j}^m = \begin{pmatrix} T_{n_1}^m - T_{n_j}^m \\ T_{n_1}^m - T_{n_j}^m \\ \vdots \\ T_{n_1}^m - T_{n_j}^m \end{pmatrix} \quad (7.7)$$

$$T_{n_j}^m = \min(T_{n_1}^m, T_{n_2}^m, \dots, T_{n_N}^m) \quad (7.8)$$

Equation (7.3) is an over-determined system of equations for  $N > 2$ . Most of the quantities in equation (7.3) can be determined a priori and stored. Only  $\Delta \mathbf{T}_{n_n,n_j}^m$  must be evaluated after the fault has occurred and the ToAs have been measured. To address the issue of measurement and propagation velocity estimation accuracy, equation (7.3) can be redefined as a constrained optimisation problem, as follows:

$$\min_{\{l, \alpha\}} \left\| \Delta \mathbf{T}_{n_n, n_i}^{(l)} + \mathbf{S}_{n_n, n_i}^{(l)} \alpha^{(l)} T_l - \Delta \mathbf{T}_{n_n, n_j}^m \right\| \quad (7.9)$$

and

$$\delta^{(l)} = \alpha^{(l)} T_l \quad (7.10)$$

By applying the first-order optimality condition, closed-form expressions can be obtained for  $\delta^{(l)}$ :

$$\frac{\partial F_c^{(l)}}{\partial \delta^{(l)}} = 2 \mathbf{S}_{n_n, n_i}^{(l) T} (\Delta \mathbf{T}_{n_n, n_j}^{(l)} + \mathbf{S}_{n_n, n_j}^{(l)} \delta^{(l)} - \Delta \mathbf{T}_{n_n, n_j}^m) = 0 \quad (7.11)$$

Equation (7.11) can be rewritten for  $\delta^{(l)}$  as:

$$\delta^{(l)} = \frac{1}{K} \mathbf{S}_{n_n, n_j}^{(l) T} (\Delta \mathbf{T}_{n_n, n_i}^m - \Delta \mathbf{T}_{n_n, n_j}^{(l)}) \quad (7.12)$$

$$K = \sum_{n=1}^{n=N} (S_{n_n, n_j}^{(l)})^2 \quad (7.13)$$

Where  $N$  denotes the number of observers.

The optimisation problem can be solved by performing an exhaustive search for the full range of possible ‘ $l$ ’ and  $\alpha$  values. Although there is a limited number of lines, reaching a level of accuracy for  $\alpha$  can be challenging and will depend on an individual line’s length. Therefore, a more effective two-step approach is proposed as follows:

- i. Determine the optimum values of  $\alpha$  for  $l \in \{1, 2, \dots, L\}$ .
- ii. Search the ‘ $l$ ’ values to determine the minimum value of the corresponding cost function for  $l \in \{1, 2, \dots, L | 0 \leq \alpha \leq 1\}$ .

### 7.3. Monte Carlo uncertainty analysis

The Monte Carlo uncertainty analysis involves propagating the distributions of the input sources of uncertainty by using the model to study the distribution of the output. Uncertainty analysis is widely used in various applications, such as electronics, control systems, economics and neural sciences [52]. The Monte Carlo uncertainty analysis involves the following steps:

- i. define the input quantities
- ii. prepare the modelling
- iii. estimate the probability density
- iv. find the functions for the input quantities
- v. setup and run the Monte Carlo simulation

vi. summarise and express the results [116].

For an uncertainty analysis, everything that can drive a variation in the output can be liberally classified as an input. The output error for fault location methods arise from a measured TW arrival time and estimated arrival time. The uncertainty in a measured TW arrival time arises from a time-synchronous device error and the TW front-end detection methods. The error from a line's length and TW propagation speed estimation are the primary sources of estimated arrival time uncertainty. These uncertainties lead to further uncertainty in determining the exact values of  $\Delta \mathbf{T}_{n,n_i}^m$ ,  $\Delta \mathbf{T}_{n,n_j}^{(l)}$  and  $T_l$  in equations (7.10) and (7.12). The uncertainty can be added indirectly to the theoretical values of  $\Delta \mathbf{T}_{n,n_i}^m$ ,  $\Delta \mathbf{T}_{n,n_j}^{(l)}$  and  $T_l$  by adding the source of the distributed random values to a line's length and the arrival times. Therefore, a line's length and the arrival times are considered input parameters of the Monte Carlo simulation.

Figure 7.2 illustrates the Monte Carlo uncertainty analysis of the proposed fault location method. First, the fault location is chosen randomly by selecting the  $L_f$  and  $\alpha_f$ . The  $L_f$  is the faulty line number and the  $\alpha_f$  is the location of the fault on the  $L_f$  with respect to the line's origin as a percentage of line's length. The  $U([x_1, x_2])$  is a random number from a uniform distribution in the interval  $[x_1, x_2]$ .

To add the uncertainty to  $\Delta \mathbf{T}_{n,n_j}^{(l)}$  and  $T_l$ , a random value can be added to the model line's length. The number,  $N\left(\ell_i, \ell_i \times \left(\frac{\mu}{3}\right)\right)$ , is a random number from a normal distribution with a mean of  $\ell_i$  and a standard deviation of  $\ell_i \times \left(\frac{\mu}{3}\right)$ . The  $\ell_i$  is the line's  $i$  length and the  $\mu$  is the percentage of the line's length. There is a 99.7% probability that the  $\ell_i^e$  lies within a band between  $\pm \ell_i \times \left(\frac{\mu}{3}\right)$ .

The vector ( $\mathbf{T}^m$ ), which contains the arrival times from a fault's location to the observers, is calculated by using the  $\mathbf{L}^e$ . Using the  $\mathbf{L}^e$  simulates uncertainty on the value of  $\Delta \mathbf{T}_{n,n_j}^{(l)}$  and  $T_l$  because of the uncertainty about the exact value of the line's length and the propagation speed of the TW. Further, to include the arrival time's detection or synchronised time errors, the random value from the normal distribution must be added to  $\mathbf{T}^m$ . The  $N(t_n^m, \delta)$  is a random value from a normal distribution with mean of  $t_n^m$  and a standard deviation of  $\delta$ .

The result ( $\mathbf{T}^e$ ) is a vector of the theoretical TW's arrival time, which contains the uncertainty of the line's length, propagation speeds, arrival time's detection and time-synchronisation error. The  $\mathbf{T}^e$  is input to the proposed fault's location algorithm to determine the fault's location. The  $LOC(\mathbf{T}^e, \mathbf{G})$  calculates the fault's location. The  $\mathbf{G}$  is the weighted graph that represents the distribution network. The difference between the randomly selected fault location and the algorithm output is used to determine the error of the result. The *IEEE guide for determining fault location on AC transmission and distribution lines* [13] describes the traditional relative fault location error for measuring a result's accuracy, such that:

$$e_r = \frac{|d_m - d_t|}{D} \times 100 \quad (7.14)$$

Where  $d_m$  and  $d_t$  are the estimated fault distance found by the proposed algorithm and the actual distance to the fault from the reference node or substation, respectively. The  $D$  is the total length of the feeder. Finally, the uncertainty can be determined by analysing the error mean and standard deviation for many randomly selected fault locations.

An IEEE 34-bus network was used as a test system to evaluate the accuracy of the proposed method (see Figure 7.3). The line lengths and TW propagation times are provided in Table 7.1. To have a fully observable network, TW observers must be installed at the end of all branches. For the network shown in Figure 7.3, at least 10 observers are required for buses 1, 5, 12, 14, 18, 22, 24, 29, 33 and 34. Three independent Monte Carlo simulations were considered for analysing the output and robustness of the proposed algorithm. Table 7.2 summarises the parameters for the three given scenarios. The first scenario is the simulation without any uncertainty to demonstrate the proposed fault location performance under the ideal conditions as a benchmark. Figure 7.4 provides histograms representing the probability distribution function for the fault location based on the line's number and the fault location from the line's origin as a percentage of the line's length. The length of line 20 is equal to zero. Therefore, it was excluded from the input distribution.

Figure 7.5 shows the output probability distribution where there is no error added to the line's data and the theoretical arrival times. The output error is negligible. There is a small amount of error due to numerical and computational errors and limitations. However, the error at the fault location is not negligible for the second and third scenarios.

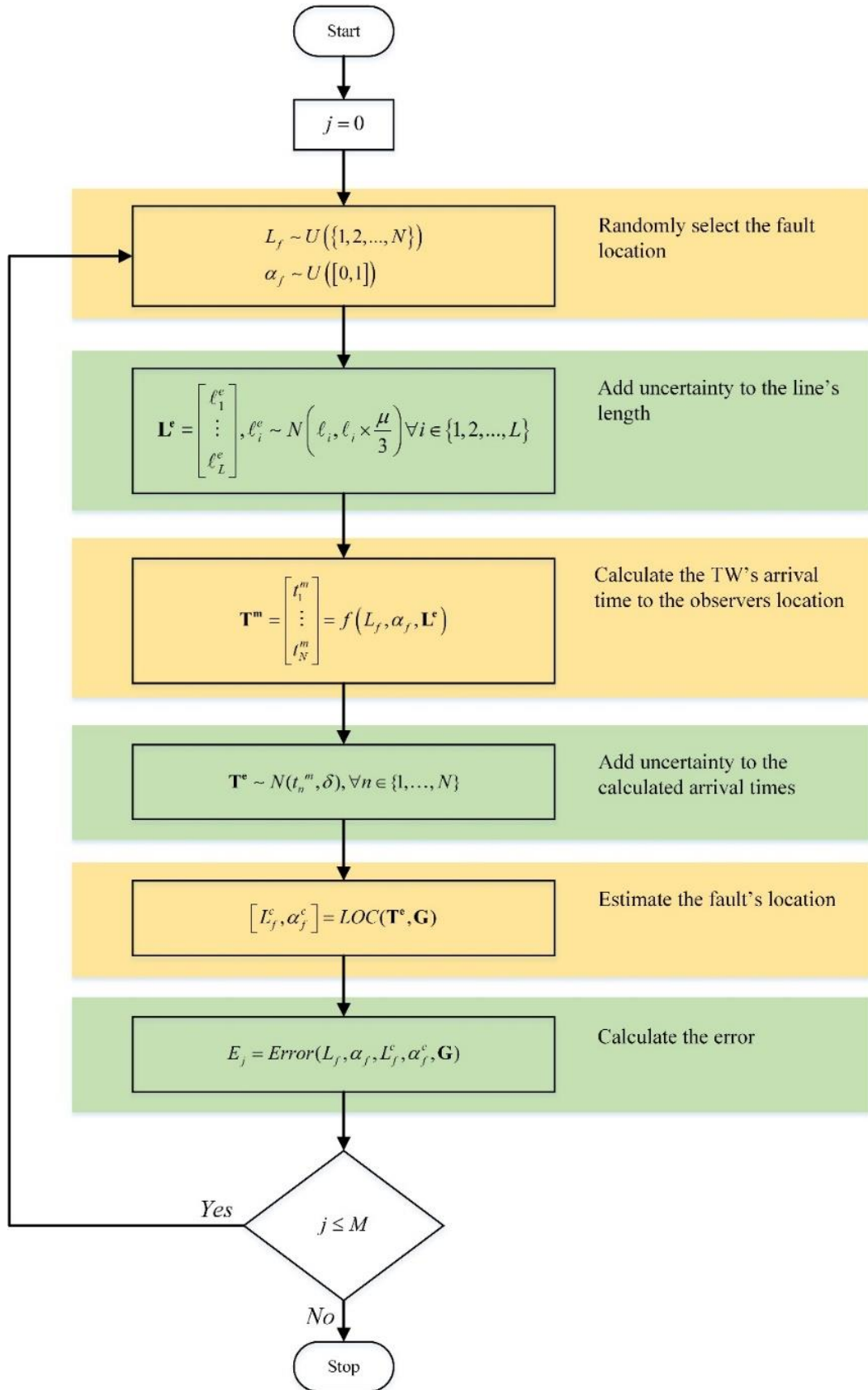


Figure 7.2. A diagram of the Monte Carlo uncertainty simulation.

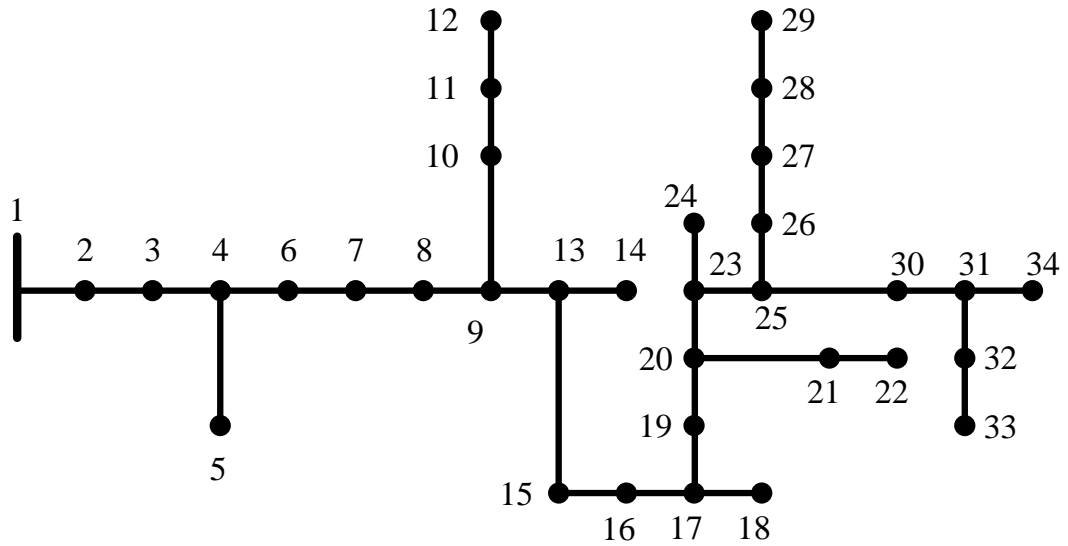


Figure 7.3. A modified single-line diagram of the IEEE 34-bus test distribution network.

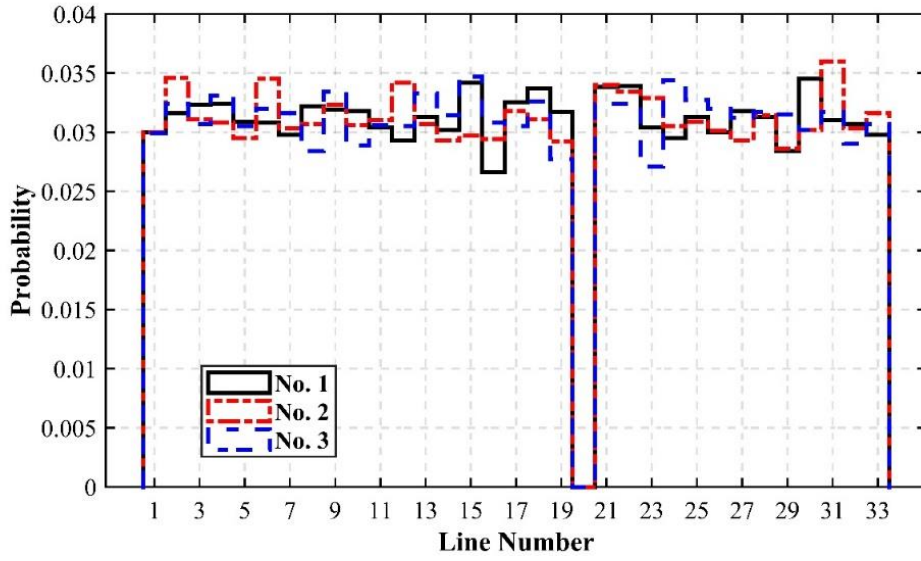
Table 7.1. IEEE 34-bus distribution line lengths and propagation times

Line	Length (m)	Time ( $\mu s$ )	Line	Length (m)	Time ( $\mu s$ )
001–002	786.38	2.63	017–019	11225.78	37.54
002–003	527.30	1.76	019–020	3.05	0.01
003–004	9823.70	32.86	020–021	0.00	0.00
004–005	1769.06	5.92	020–023	1493.52	5.00
004–006	11430.00	38.23	021–022	3218.69	10.76
006–007	9061.70	30.31	023–024	493.78	1.65
007–008	3.05	0.01	023–025	1776.98	5.94
008–009	94.49	0.32	025–026	85.34	0.29
009–010	521.21	1.74	025–030	615.70	2.06
009–013	3112.01	10.41	026–027	411.48	1.38
010–011	14676.12	49.08	027–028	1109.47	3.71
011–012	4187.95	14.01	028–029	161.54	0.54
013–014	923.54	3.09	030–031	816.86	2.73
013–015	256.03	0.86	031–032	85.34	0.29
015–016	6230.11	20.84	031–034	262.13	0.88
016–017	158.50	0.53	032–033	1481.33	4.95
017–018	7110.98	23.78			

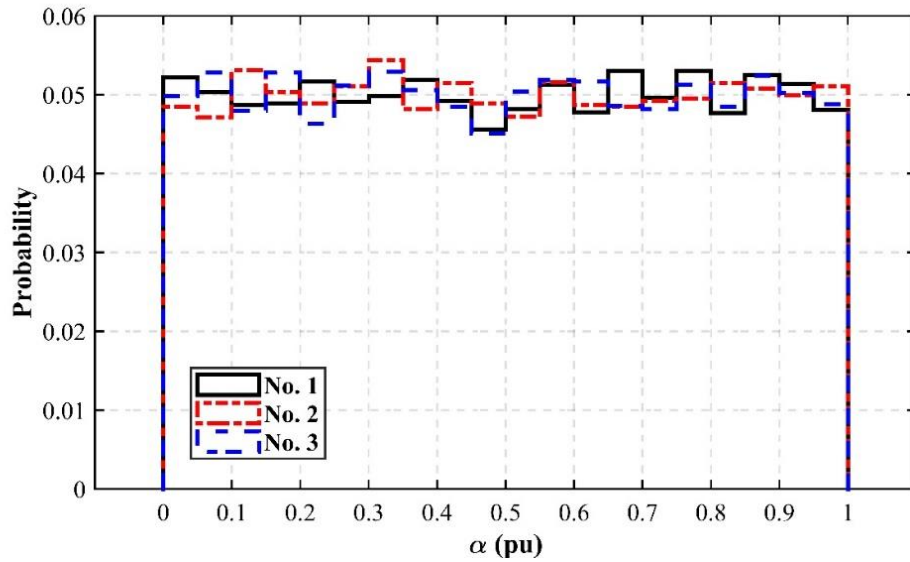
Table 7.2. The Monte Carlo simulation parameters

Scenario No.	$\mu$ pu	$\delta$ $\mu s$	Run trials
1	0	0	$10 \times 10^3$
2	0.05	0.5	$10 \times 10^3$
3	0.10	1	$10 \times 10^3$





(a)



(b)

**Figure 7.4. Histograms representing the probability distribution function for the fault location: (a) line numbers ( $L_f$ ); and (b) the location of the fault at the  $L_f$  with respect to the line's origin as a percentage of the line's length ( $\alpha$ ).**

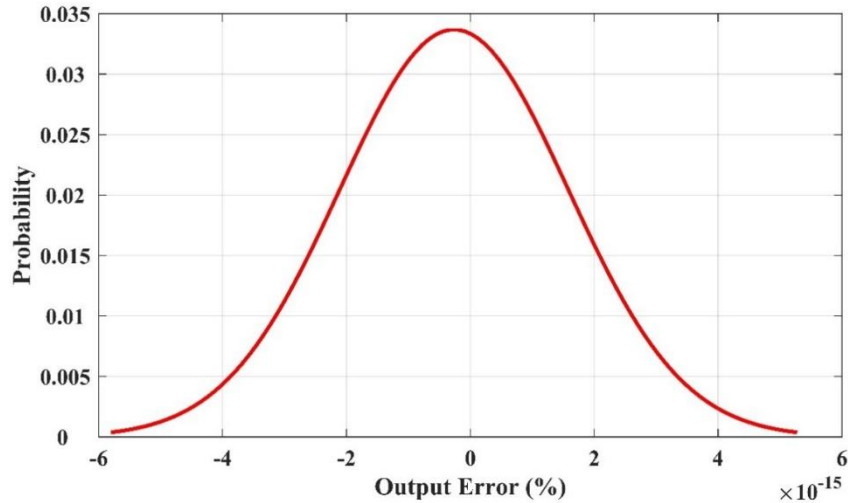


**Figure 7.5. The output probability distribution of the first scenario.**

Figure 7.6 represents the probability distribution of the fault location algorithm for the second and third simulations. As expected, the error dispersion was around zero for scenario 1 and lower than scenario 2.

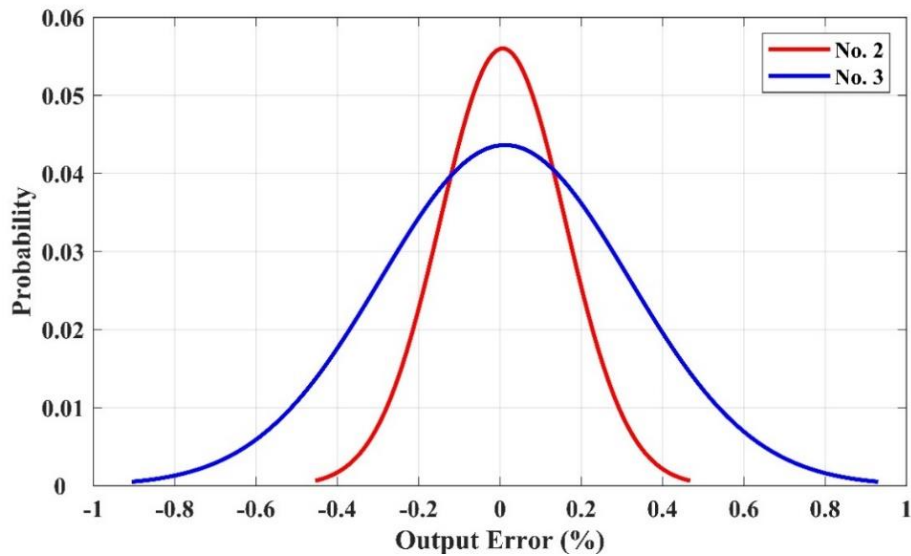


**Figure 7.6. The output probability distribution of the second and third scenarios.**

For a more comprehensive comparison, Table 7.3 summarises the mean, standard deviation and maximum error of the location for all three scenarios. The accuracy is defined by the symmetrical band around zero, where 99.7% of the output error lies. This is associated with the standard deviation times three. The maximum error is almost double in scenario 3 compared to scenario 2, where the amount of error in the line's length is halved.

**Table 7.3. Summary of the results for all scenarios**

<b>Scenario</b>	<b>Mean</b>	<b>Standard deviation</b>	<b>Correct line identified</b>	<b>Accuracy</b>
<b>No.</b>	<b>(%)</b>	<b>(%)</b>	<b>(%)</b>	<b>(m)</b>
1	$-2.632 \times 10^{-16}$	$1.847 \times 10^{-15}$	100	$\pm 5.204 \times 10^{-12}$
2	$7.036 \times 10^{-3}$	$15 \times 10^{-2}$	72.2	$\pm 433$
3	$12.64 \times 10^{-2}$	$31 \times 10^{-2}$	61.8	$\pm 862$

#### 7.4. Summary

In this chapter, a new travelling wave-based fault location method is proposed for radial distribution networks. This chapter also deals with the performance of the proposed method and presents uncertainty analysis. The performance and uncertainty analysis, demonstrate the method accuracy is limited by the level of uncertainty in the lines length, estimated TW propagation speed and TW arrival time detection. The proposed methods lead to an increase in precision without increasing the complexity.

## Chapter 8

# Accuracy enhancements for the proposed fault location algorithm

*Content of this chapter is published in the IEEE Transactions on Power Delivery, vol. 35, no. 3, pp. 1553-1562, June 2020, doi: 10.1109/TPWRD.2019.2948174.*

### **8.1. Introduction**

Regardless of the TW location method used, the travel time along the line or feeder is the critical parameter. Junctions, load taps and bifurcations not only cause the TW energy to dissipate rapidly in a distribution network, but they also affect the incident wave travel time. A simple distribution feeder was considered in most studies, and the effect of the power system components was ignored.

Chapter 7 demonstrated that the HIF location could be successfully implemented by using the voltage observers distributed along a radial distribution feeder. The behaviour of voltage TWs at the junctions of power lines and passive circuit elements (resistances, inductances and capacitances) was discussed in Chapter 3.

Chapter 8 discusses the effects of the parasitic capacitance of a distribution transformer on the TW arrival time detection algorithm. A method is proposed to increase the fault location accuracy by estimating the TW arrival time error. The proposed algorithm estimates the fault location accuracy by considering the number

and characteristics of transformers between the voltage TW detectors and the fault's location.

## 8.2. The effects of parasitic capacitance

A junction between a power line and shunt capacitor is shown in Figure 3.6. When a voltage TW with amplitude ( $V_1$ ) approaches the junction of a power line, with a characteristic impedance ( $Z_A$ ) with a capacitor, the junction behaves as a first-order low-pass filter with a time constant of  $\frac{\tau_c}{2}$  (see Table 3.2). The refracted voltage TW is equal to:

$$v_3(t) = m \left( t - \frac{\tau_c}{2} \right) + \frac{m\tau_c}{2} e^{-\frac{2t}{\tau_c}} \quad (8.1)$$

Where  $m$  is the slope of the incident wavefront edge. The refracted wave,  $v_3(t)$ , can be rearranged to a general form of:

$$v_3(t) = g(t) + h(t) \quad (8.2)$$

This indicates that the refracted wave is the summation of two functions. The first function,  $g(t)$ , is the ramp function with a time delay of  $\frac{\tau_c}{2}$  and a rising or falling slope equal to the initial incident wave. The second function is an exponential function that decays to zero. The refracted wave can be approximated as a time-delayed version of the original incident wave if the time constant ( $\tau_c$ ) is small compared to the rise time. The TW detection algorithms detect the ToA through observations that are a function of the voltage or current rate of change. Therefore, they may be affected by capacitors connected to the line.

For a shunt-connected inductor, a high-pass characteristic is obtained. From Table 3.2, the refracted wave is equal to:

$$v_3(t) = 2m\tau_L \left( 1 - e^{-\frac{t}{2\tau_L}} \right) \quad (8.3)$$

For relatively short periods to the time constant is:

$$\left( 1 - e^{-\frac{t}{2\tau_L}} \right) \approx \frac{t}{2\tau_L} \quad (8.4)$$

and

$$v_3(t) = mt \quad (8.5)$$

Equation (8.5) implies that inductors behave like an open circuit for times that are short relative to the time constant. The fast-rising edge of a TW will pass the

inductor junction; however, the lower-frequency components will be attenuated. The reflected wave is equal to (see Table 3.2):

$$v_2(t) = 2m\tau_L \left( 1 - e^{-\frac{t}{2\tau_L}} \right) - mt \quad (8.6)$$

Substituting equation (8.5) into equation (8.6) gives:

$$v_2(t) = 2m\tau_L \left( \frac{t}{2\tau_L} \right) - mt = 0 \quad (8.7)$$

### 8.3. The effects of a transformer

A junction with an overhead line and transformer is common within power distribution system. A simplified model of the transformer is sufficient to study a TW reflection and refraction at these junctions (see Chapter 4). The simplified models for the single- and three-phase transformers are shown in Figure 8.1.

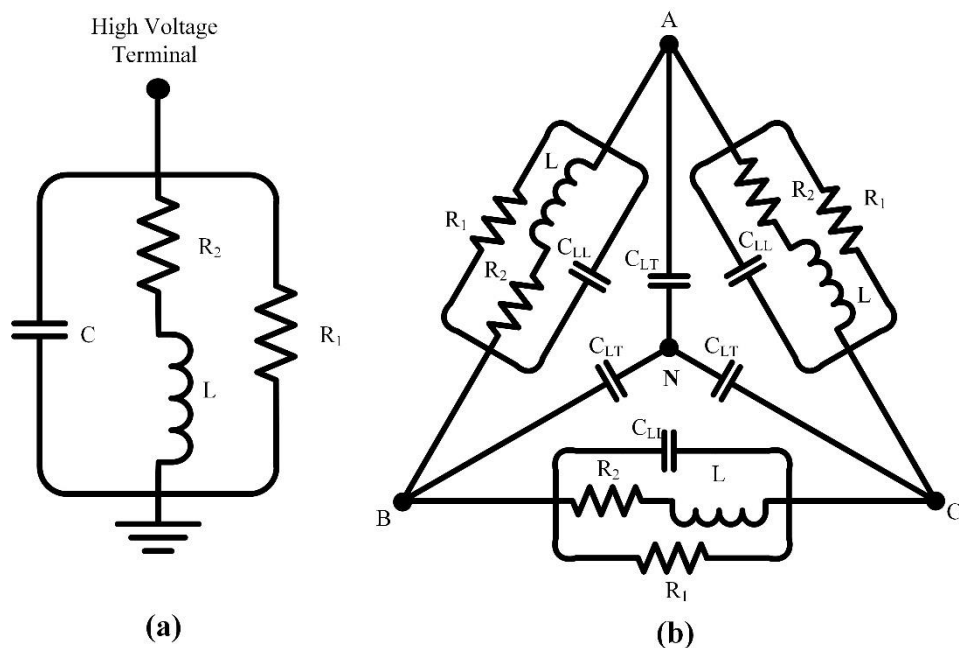


**Figure 8.1. Simplified models for the: (a) single-phase or single-wire earth-return transformer; and (b) three-phase transformer.**

For the single-phase transformer in normal operating conditions, the values of the parallel ( $R_1$ ) and series resistance ( $R_2$ ) with the inductive reactance ( $L$ ) are very large compared to the overhead line's characteristic impedance. These can be assumed as an open circuit. However, the capacitance of the transformer can affect the high-frequency components of the incident wave. The refracted TW from the capacitor junction can be assumed as a time-shifted version of the original incident wave (see

Section 8.2). That is, transformers can increase the travelling time along a feeder. The capacitance of a single-phase transformer in the aerial mode is shown in Figure 8.1 (a); this is equal to:

$$C_{\alpha} = C_{\beta} = C \quad (8.8)$$

Where:

- $C_{\alpha}$  and  $C_{\beta}$  are capacitances of the aerial mode voltage TWs
- $C$  is the HV transformer terminal's capacitance to the ground.

Similarly, for a three-phase transformer model (see Figure 8.1 (b)):

$$C_{\alpha} = C_{\beta} = 2C_{LL} + C_{LT} \quad (8.9)$$

Where  $C_{LL}$  and  $C_{LT}$  are the line-to-line and line-to-tank capacitance of the three-phase transformer, respectively.

Travelling time delay is caused by a single- or three-phase transformer and can be estimated by using equations (3.40), (8.8) and (8.9). For instance, the parameters measured for a 25 kVA, 19/0.240 kV SWER transformer under 50% load conditions are:  $R_1 = 263.2 \text{ k}\Omega$ ,  $R_2 = 29.7 \text{ k}\Omega$ ,  $L_1 = 1.23 \text{ H}$  and  $C = 904 \text{ pF}$ . Therefore, the travelling time delay created by a 25 kVA SWER transformer junction and overhead line with a characteristic impedance of  $300 \text{ }\Omega$  is 135 ns. This is equivalent to approximately 40 m. Multiple transformers in a distribution network will exacerbate the situation and could cause a considerable magnitude of error. Many transformers can cause cumulative errors in a TW fault location algorithm.

#### 8.4. Validation and experimental setup

Section 8.4 presents two case studies to validate the effects of a junction with a transformer on an incident wave. The transmission line was emulated by a single twisted pair of standard Cat5E cable, characterised by  $100 \text{ }\Omega$  surge impedance and a propagation velocity of  $0.64 c$ . An external  $50 \text{ }\Omega$  resistance in a series with a signal generator of  $50 \text{ }\Omega$  internal resistance matched the signal generator impedance of the cable. The trigger signal from the signal generator provided the time reference for comparing the test results. A schematic diagram of the first experimental setup is shown in Figure 8.2.

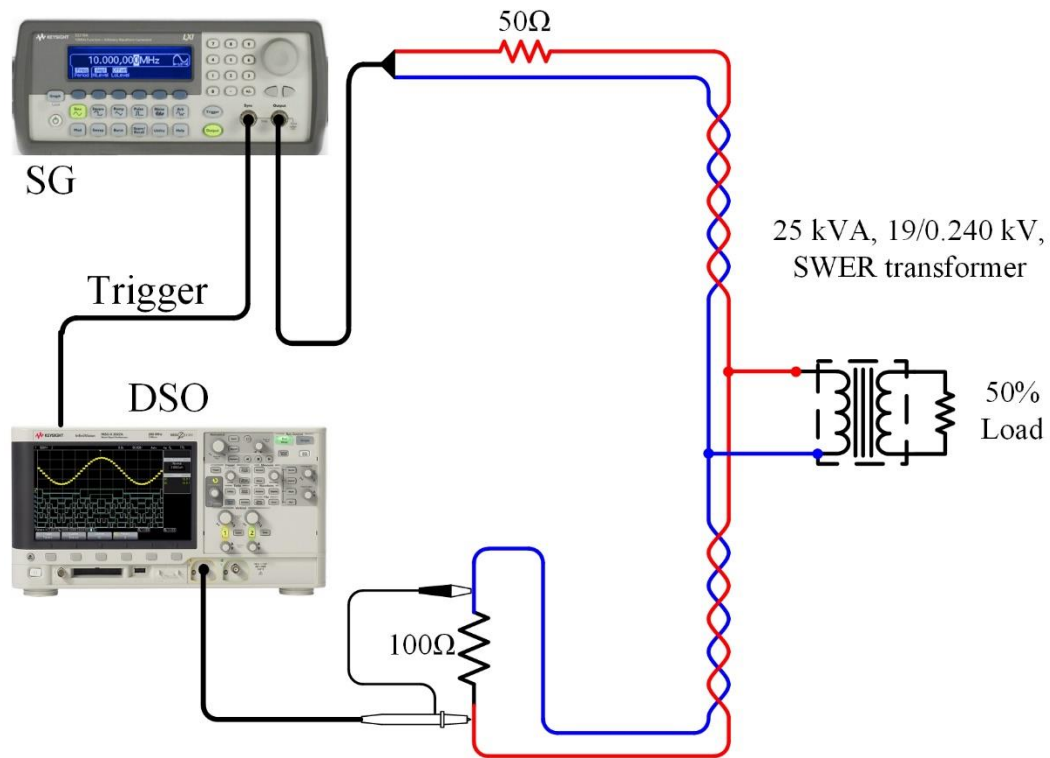


**Figure 8.2. A schematic diagram of the first experimental setup.**

A typical 25 kVA SWER transformer was used for the experiment. Figure 8.3 shows the SWER transformer and its nameplate. The two low voltage windings were used in parallel by connecting terminal a1 to a3 and terminal a2 to a4. The nominal current of the secondary winding was equal to 100 A. The 4.7 Ω resistor was connected to the secondary to simulate 50% loads on the transformer. The signal generator produced a 250 kHz triangular wave with a slope of  $\pm 2.8 \times 10^6$  V/s.

The transformer's capacitance to ground was equal to 904 pF. From Table 3.2, the junction time constant is:

$$\tau_c = Z_A C = 100 \times 904 \times 10^{-12} = 90.4 \text{ nsec}$$

This reveals that the time constant is significantly smaller than the waveform's positive or negative slope. Therefore, the transformer was expected to increase the travelling time from the signal generator to the end of the cable (see Section 8.2). The waveform at the end of the cable was recorded using a TDS 5034 digital oscilloscope at a sampling frequency of 2.5 GS/s with and without the transformer. The time difference between the two cases was equal to 46 ns, which was close to the expected time difference from the theory and equal to:

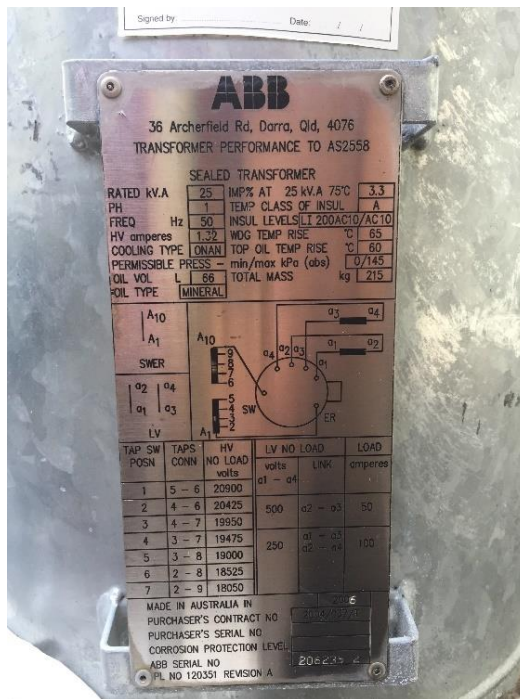
$$\frac{\tau_c}{2} = \frac{90.4 \text{ ns}}{2} = 45.2 \text{ nsec}$$

Figure 8.4 shows the recorded waveforms.





(a)



(b)

**Figure 8.3. The 25 kVA single-wire earth-return transformer that was used for the test, showing: (a) the transformer; and (b) the transformer's nameplate.**

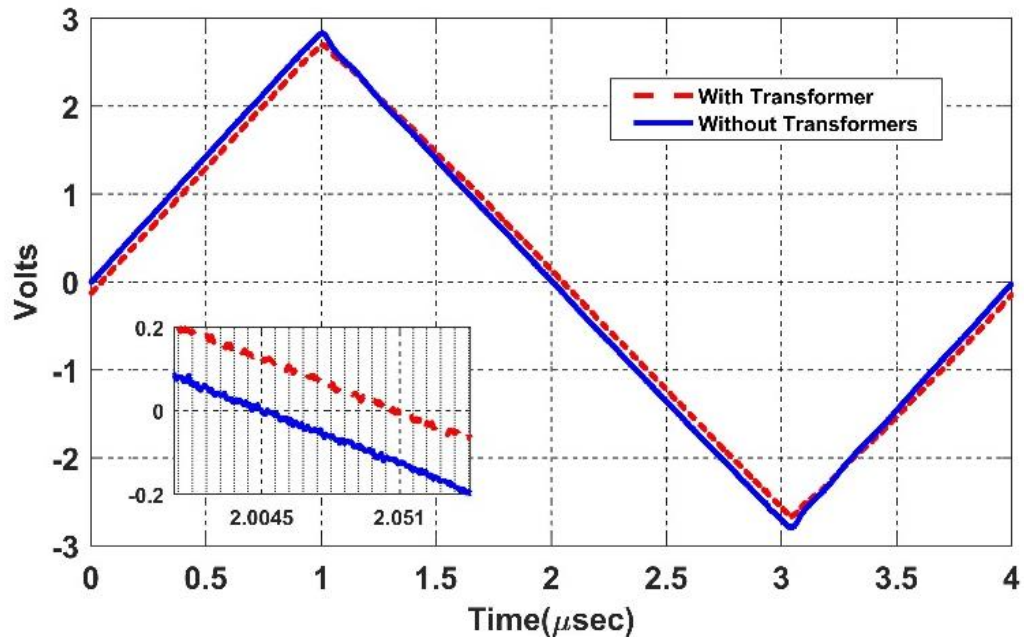


**Figure 8.4. The first recorded waveforms at the cable end.**

One end of the SWER transformer's HV winding was grounded and effectively shorted to the transformer tank. Therefore, the effective capacitance to ground of the winding was substantially different from the total capacitance of the winding to tank if the winding was left floating. The effective winding capacitance for a SWER transformer from the HV terminal and transformer tank (ground) was less than that of the same size transformer intended for a line-to-line connection. The HV bushings made a significant contribution to the effective capacitance calculation.

The second experimental setup aimed to demonstrate the multiple transformers' cumulative errors in detecting the TW arrival time (see Figure 8.5). A signal generator created the ramp function in a burst mode with a  $2\mu\text{s}$  rise time.

The voltage across the  $100\ \Omega$  termination resistor was recorded using an Agilent MSO-X 2012A digital oscilloscope operating at  $500\ \text{MS/s}$ . The multiple transformers were emulated using five capacitors of  $10\ \text{nF}$  each. The theoretical estimated error for the arrival time was  $500\ \text{ns}$ . Therefore, the total error for the experimental setup was expected to be around  $2.5\ \mu\text{s}$ . Figure 8.6 shows the voltage across the termination impedance and the signal's wavelet energy coefficient. The theoretical expectation complied with the results shown in Figure 8.6.

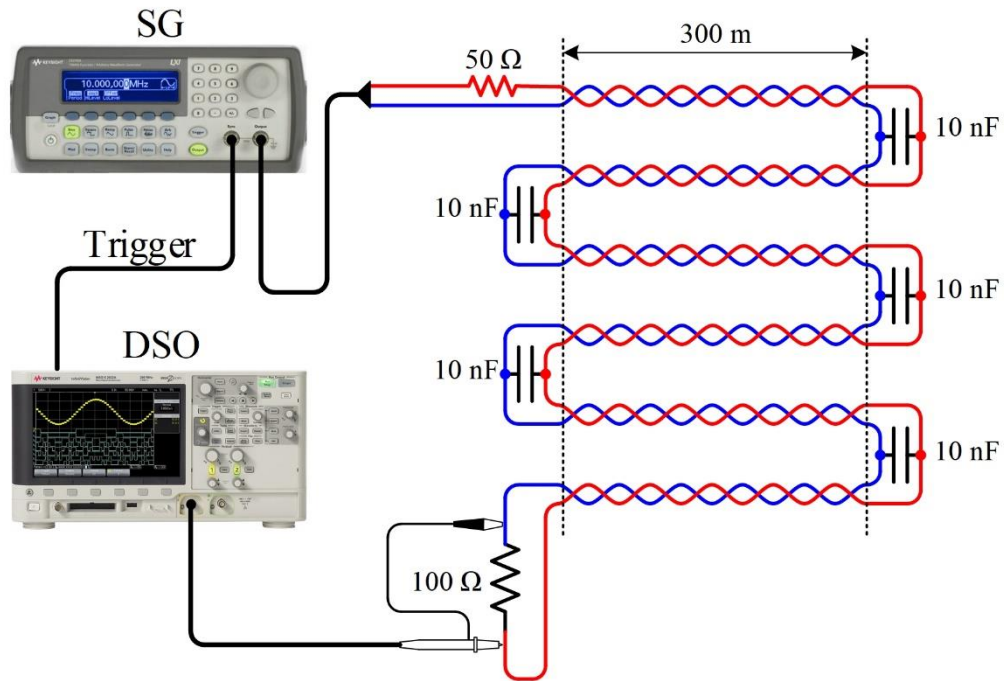


**Figure 8.5. The experimental setup, demonstrating the multiple transformers' cumulative error.**

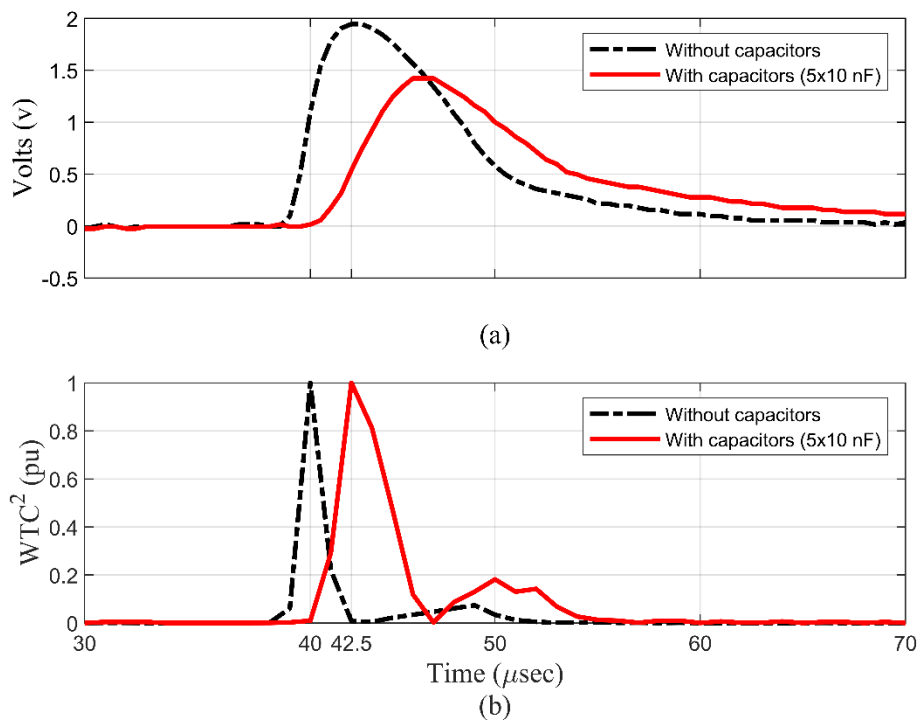


**Figure 8.6. Graphs showing: (a) the voltages measured across the termination impedance; and (b) the wavelet energy coefficient for the recorded voltage.**

### 8.5. Travelling time considering the transformer's effects

Sets of theoretical TW propagation times ( $\{T_l\}$  and  $\{T_{l,n_n}\}$ ) from the line origins to the terminus and detectors must be calculated (see Chapter 7). The  $\{T_l\}$  and  $\{T_{l,n_n}\}$  can be calculated by dividing the distances or lengths by the wave propagation velocities for each segment. The TW propagation velocity ( $v^{(l)}$ ) is calculated from:

$$v^{(l)} = \frac{1}{\sqrt{L^{(l)'}C^{(l)'}}} \quad (8.10)$$

Where  $L^{(l)'}$  and  $C^{(l)'}$  are the inductance and capacitance of the line ( $l$ ) per unit length, respectively. However, a transformer could affect the travelling time along a feeder (see Section 8.3). In rural distribution networks, a long section of feeder could include numerous transformers connected at tee-offs.

The compensation for the transformer induced delays can increase the accuracy of location TW faults. The estimated error caused by the transformers should be included in the theoretical travelling time to reduce the effect of the transformers. The time delay introduced by the transformers can be added into the calculated travelling time, as shown below:

$$T'_{l,n} = T_{l,n} + \sum_{p=1}^{q_{l,n}} \frac{\tau_p}{2} \quad (8.11)$$

Where  $q_{l,n}$  is the number of transformers between the origin of  $l$  and the detector ( $n$ ) and  $\sum_{p=1}^q \frac{\tau_p}{2}$  is the total estimated error caused by the distribution transformers. By using the  $T'_{l,n}$  instead of  $T_{l,n}$  as an input to the TW fault location algorithm proposed in Chapter 7, improved accuracy is achievable.

### 8.6. Simulation results

A simulation was conducted on a distribution network (see Figure 8.7) using EMTP-RV software to demonstrate the effectiveness of the proposed method for improving the accuracy of the fault location. The transformer models are shown in Figure 8.1. The parameters are listed in Table 8.1 with a simulation time step of 100 ns.

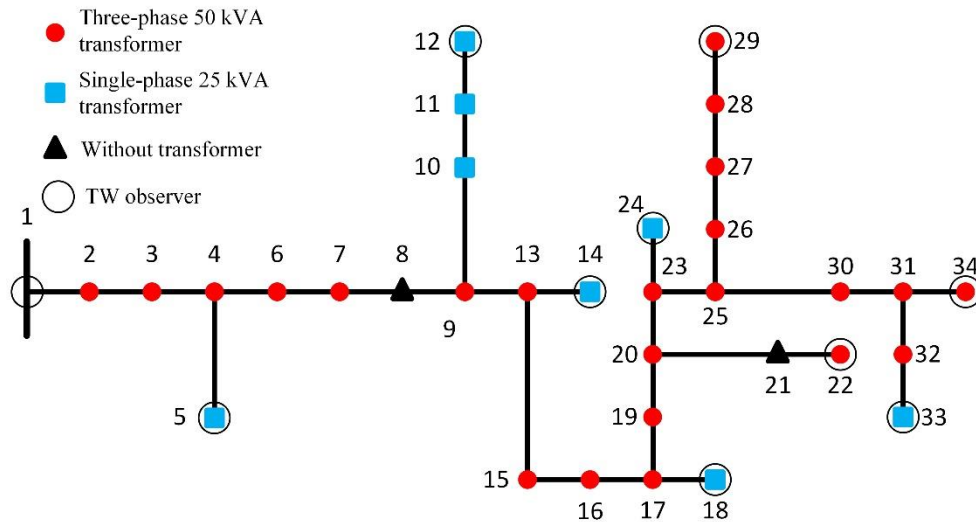


**Figure 8.7. A modified single-line diagram of the IEEE 34-bus test distribution network.**

**Table 8.1. Transformer models' parameters**

Three-phase (dy11) 100 kVA transformers with 50% load		Single-phase 25 kVA transformer with 50% load	
L	1.232 H	L	1.23 H
R	22.8 k $\Omega$	$R_1$	263.2 k $\Omega$
$C_{LL}$	1 nF	$R_2$	29.7 k $\Omega$
$C_{LT}$	2.2 nF	C	904 pF

The expected time delays were found to be 0.693  $\mu$ s and 0.149  $\mu$ s for each three-phase and single-phase transformer, respectively. The phase voltages were obtained at the end of each branch. By using MATLAB, the captured voltages were down-sampled to an equivalent sampling frequency of 2 MHz. The arrival time was detected by using the methods described in Chapter 5. A fault was simulated on line 027–028, 0.707 km away from bus 27 (i.e.,  $\alpha = 0.4$ ). The simulated fault was 56.923 km away from bus 1.

The three-phase-to-ground fault was simulated as an ideal switch in series with a fault resistance. Table 8.2 shows the arrival time at the selected buses. First,  $T_{l,n}$  was used to find the fault's location. Then,  $T_{l,n}$  was replaced with  $T'_{l,n}$  to consider the travelling time delay introduced by the transformers.

Table 8.3 shows the calculated fault location and relative error. The results demonstrate the effect of distribution transformers on the fault location algorithm. The

results also demonstrate that the accuracy of fault location can be improved significantly by considering the effects of the transformer.

**Table 8.2. Travelling wave arrival times for the fault on line 027–028**

<b>Bus No.</b>	<b>Without transformers</b>	<b>With transformers</b>
1	5.191	5.200
5	5.160	5.167
12	5.150	5.157
14	5.077	5.083
34	5.008	5.013
29	5.004	5.005

**Table 8.3. Fault location results**

<b>Simulation</b>	<b>Fault location</b>	<b>Fault location from bus 1</b>		<b>Relative error</b>	<b>Absolute error</b>
	<b>Line</b>	<b><math>\alpha</math></b>	<b>km</b>	<b>%</b>	<b>m</b>
Without compensation	028–029	0.053	57.597	1.118	+674
With compensation	027–028	0.209	56.711	0.372	–212

## 8.7. Summary

In this chapter the effect of the parasitic capacitance of distribution transformer on travelling wave propagation is discussed. Theoretical analysis and laboratory results show that the transformer parasitic capacitance introduces an error in the fault location estimation. A method is proposed to eliminate the negative impact of the parasitic capacitances. The proposed method in this chapter enhances the fault location accuracy by considering the number of distribution transformers between the voltage TW detectors and the fault location.

## Chapter 9

# Optimal deployment of synchronised voltage travelling wave sensors

*Content of this chapter is accepted for publication in the IEEE Access on April 2021.*

### 9.1. Introduction

A fault occurring in a distribution network generates transient high-frequency TWs that propagate through the entire network. The fault location can be determined by recording the instants at which the incident waves arrive at various points on the network [50]. In a transmission line, the two time-synchronised observers at the ends of the line are adequate for determining the fault location. In a distribution network with many branches, loads, switching devices and distributed transformers, two observers are insufficient for observing the entire network. A fully locatable network requires at least one observer per branch or spur. From an economic point of view, this is an unlikely solution. A reasonable number of relatively low-cost voltage TW observers with GPS time-synchronisation and radio communication can be deployed to detect and time-stamp the TW's arrival at several points.

Chapter 9 extends the fault location method based on time-synchronised voltage travelling sensors and develops a method to optimally place the given number of TW detectors to maximize the observability and locatability. Considering the topology of the distribution network and using the proposed technique for fault

location from Chapter 7, an optimal strategy for placing a given number of time-synchronised measurements is developed.

### 9.1.1. Fault observability analysis

In a transmission system, TWs propagate freely towards the ends of the line and over many kilometres. Conversely, distribution networks feature many laterals and load taps along the length of a relatively short distribution line [114], which present many points for partial reflection. The energy of fault-induced TWs will rapidly reduce when passing multiple laterals and bifurcation points. Where there are multiple bifurcations between the fault and TW observer, the energy of the TW at the observer location may be insufficient to be detected. The energy of the TW generated by HIFs is lower compared to that of low impedance faults. Therefore, the total reflection coefficient between each line and TW detector must be considered when placing the distributed TW observers.

A branch or line is regarded as an observable if a fault in the line can be detected by considering the reflection coefficient between the line ends and TW detectors. Otherwise, the branch or line segment is considered unobservable. The total reflection coefficient between the line's start or terminus must be smaller than the predetermined value. The minimum refraction coefficient can be determined from the TW detector's sensitivity. For the known locations of the TW synchronised detector, the analysis for determining the observable and unobservable branches of the radial distribution network is referred to as the fault observability analysis.

The matrix  $\mathbf{B}_{L \times N}$  was built for the given network.  $L$  is the number of lines and  $N$  is the total number of buses.

$$\mathbf{B} = \begin{bmatrix} b_{1,1} & \cdots & b_{1,N} \\ \vdots & \ddots & \vdots \\ b_{L,1} & \cdots & b_{L,N} \end{bmatrix} \quad (9.1)$$

Where  $b_{l,n}$  is a total reflection coefficient affecting the incident wave travelling from anywhere in the line ( $l$ ) to bus  $n$ . The total refraction coefficient to travel from  $l$  to bus  $n$  can be determined by multiplying the refraction coefficients of all the junctions between the start of the  $l$  or terminus and bus  $n$ .

For the  $l$  in the example network (see Figure 9.1), the total refraction coefficient when the incident wave travels between the  $l$  and bus  $n$  is equal to:

$$b_{l,n} = b_{10} \times b_{11} \times b_{12} \times b_{13} \times b_{14} \times b_{15} \quad (9.2)$$



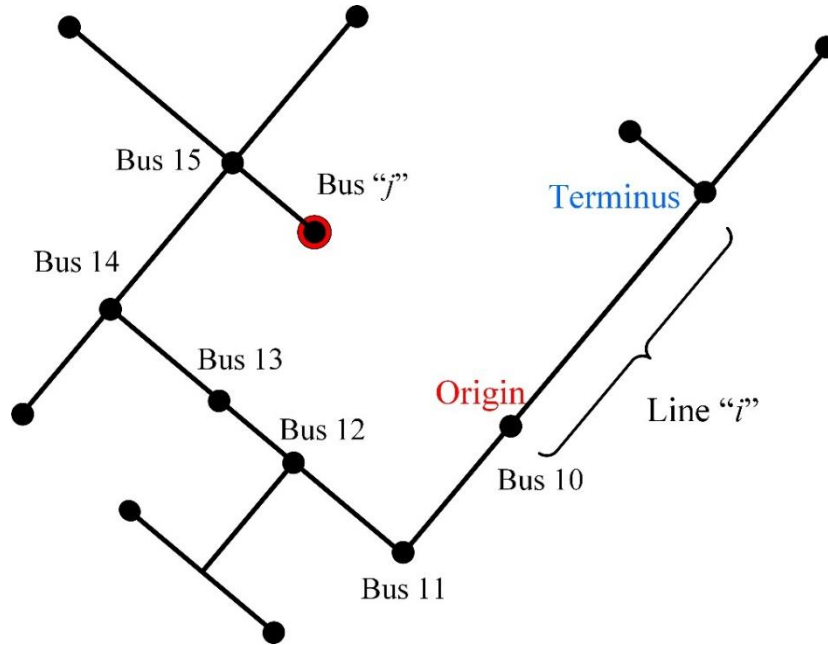


**Figure 9.1. A single-line diagram of a typical radial network.**

Where  $b_{11}$  to  $b_{15}$  are the refraction coefficients of bus 10 to bus 15. The refraction coefficients are also dependent on the direction in which the incident wave travels. The vector  $\mathbf{M}_{L \times N}$  is defined as:

$$\mathbf{M}_{N \times 1}^l = \begin{bmatrix} m_{l,1} \\ \vdots \\ m_{l,n} \\ \vdots \\ m_{l,N} \end{bmatrix} \quad (9.3)$$

Where:

$$\mathbf{M}_{N \times 1}^l = \begin{cases} 1 & \text{if } b_{l,n} > \beta \text{ for } 1 \leq n \leq N \\ 0 & \text{else } 1 \leq n \leq N \end{cases} \quad (9.4)$$

Where  $\beta$  is a threshold value that depends on the sensitivity required to detect the TW. The non-zero value of  $m_{l,n}$  indicates whether the observer installed at the node  $n$  can observe the fault that may occur on the  $l$ .

The binary variable ( $z_n$ ) represents the existence of an observer at bus  $n$  (where a non-zero value indicates existence) and  $\circ$  is the Hadamard product; therefore, the following observability vector can be calculated for the  $l$  for the known network:

$$\mathbf{Z}^l = \mathbf{M} \odot \mathbf{Z} = \begin{bmatrix} m_{l,1} \\ \vdots \\ m_{l,n} \\ \vdots \\ m_{l,N} \end{bmatrix} \circ \begin{bmatrix} z_1 \\ \vdots \\ z_n \\ \vdots \\ z_N \end{bmatrix} = \begin{bmatrix} z_1^l \\ \vdots \\ z_n^l \\ \vdots \\ z_N^l \end{bmatrix} \quad (9.5)$$

Where the non-zero value of  $z_n^l$  indicates that an observer exists at node  $n$  that can detect a fault that may occur on the  $l$ .

### 9.1.2. Fault locatability analysis

A branch or line is regarded as locatable if the fault in the branch can be uniquely located using the available set of measurements. Otherwise, the branch or line segment is said to be unlocatable. The locatability is independent of the observability. A faulty line can be observable but not locatable. Although a line may be observable, if all the observers are installed on the start or terminus side of the line, then a fault's location cannot be uniquely identified on the line (see Section 2.3). A matrix  $\mathbf{S}$  that contains  $L$  rows and  $N$  columns (where  $L$  is the total number of lines and  $N$  is the total number of buses) was built for the given network. The  $\mathbf{S}$  is a sign vector:

$$\mathbf{S} = \begin{bmatrix} s_1^1 & \cdots & s_N^1 \\ \vdots & \ddots & \vdots \\ s_1^L & \cdots & s_N^L \end{bmatrix}$$

Where  $s_n^l$  is equal to  $-1$  if the closer path to detector  $n$  includes the  $l$  terminus or  $s_n^l$  is equal to  $+1$  if it does not include the  $l$  terminus.

The  $l$  is observable if the absolute value of  $W(\mathbf{S}, \mathbf{Z})^l$  is smaller than the total number of observers ( $P$ ) and,

$$W(\mathbf{S}, \mathbf{Z})^l = [s_1^l \quad \cdots \quad s_n^l \quad \cdots \quad s_N^l] \begin{bmatrix} z_1 \\ \vdots \\ z_n \\ \vdots \\ z_N \end{bmatrix} \quad (9.6)$$

If the  $W(\mathbf{S}_{1 \times N}^l, \mathbf{Z})^l$  is equal to  $-P$ , then the shortest path to all observers includes the  $l$  terminus. If the  $W(\mathbf{S}_{1 \times N}^l, \mathbf{Z})^l$  is equal to  $+P$ , then the shortest paths to none of the observers include the  $l$  terminus. In this condition,  $K$  from equation (7.13) is equal to zero, therefore,  $\alpha^{(l)}$  cannot be determined. Vector  $\mathbf{Q}^z$  is defined as:

$$\mathbf{Q}^z = \begin{bmatrix} q_1^z \\ \vdots \\ q_l^z \\ \vdots \\ q_L^z \end{bmatrix} = \begin{bmatrix} R(W(\mathbf{S}, \mathbf{Z})^1) \\ \vdots \\ R(W(\mathbf{S}, \mathbf{Z})^l) \\ \vdots \\ R(W(\mathbf{S}, \mathbf{Z})^L) \end{bmatrix} \quad (9.7)$$

and

$$R(W(z)^l) = \begin{cases} 1 & \text{if } |W(\mathbf{S}, \mathbf{Z})^l| < P \\ 0 & \text{if } |W(\mathbf{S}, \mathbf{Z})^l| = P \end{cases} \quad (9.8)$$

For the given vector  $\mathbf{Z}$  and matrix  $\mathbf{S}$ , a value of 0 in the column vector  $\mathbf{Q}^z$  implies that the respective branch or line is unobservable; however, a value of 1 indicates that the respective branch or line is observable. Although a fault's location may not be observable, the faulted line or branch can be identified.

## 9.2. Travelling wave detector placement model

The issue of TW detector placement is a binary optimisation problem. The most popular heuristic optimisation techniques for solving binary problems are binary particle swarm optimisation (BPSO) [117, 118] and the genetic algorithm [119]. BPSO and the genetic algorithm are computational methods that search for an optimisation solution by iteratively trying to improve a candidates solution. BPSO offers significant potential for locating a near-optimal solution for highly dimensional, non-convex and non-continuous optimisation problems. All particles in BPSO and their histories contribute to the search. Conversely, in the genetic algorithm, the poor solutions are eliminated. By remembering all the particle's historical contributions, all undiscovered good neighbourhoods in the vicinity of these personal bests may be explored. A good solution may be within close vicinity of a poor particle [120]. Section 9.2 uses BPSO to solve the TW detector placement model's.

### 9.2.1. Optimisation objectives

The objective is to place a limited number of TW observers within a distribution network in a way that minimises the length of unobservable or unlocatable lines. The objective function ( $OF$ ) can be expressed as:

$$OF(\mathbf{S}, \mathbf{Z}, \mathbf{M}, \mathbf{L}_{L \times 1}) = \sum_{i=1}^L q_i^z L_i \quad (9.9)$$

Where  $L_i$  is the length of the line ( $i$ ) and the output is equal to the total line length that is observable and locatable.

### 9.2.2. Constraint handling

The placement of TW observers is a constrained optimisation problem. The optimisation algorithm tries to maximise the number of lines that are observable and locatable. If the number of observers is not constrained, the solution would not be economical to implement. There are several ways to handle the constrained BPSO problem. The most common constraint handling technique is a penalty function method, where a penalty term is added to the fitness function for any violation of the constraints [119]. The penalty function,  $PF(\mathbf{Z})$ , is defined as:

$$PF(\mathbf{Z}) = \begin{cases} 0 & P(\mathbf{Z}) = p \\ (P(\mathbf{Z}) - p)^2 & P(\mathbf{Z}) \neq p \end{cases} \quad (9.10)$$

Where  $P(\mathbf{Z})$  is equal to:

$$P(\mathbf{Z}) = [1 \dots 1] \begin{bmatrix} z_1 \\ \vdots \\ z_N \end{bmatrix} \quad (9.11)$$

Where  $p$  is the desired number of observers. The  $P(\mathbf{Z})$  is a function that returns the number of observers present on vector  $\mathbf{Z}$ . The  $PF(\mathbf{Z})$  is equal to zero when the number of observers in vector  $\mathbf{Z}$  is equal to the desired number of  $p$ .

### 9.2.3. Optimisation model

Based on the objective and the penalty function, the optimisation observer placement model for maximising the length of observable and locatable lines with a given number of observers is as follows:

$$\min CF = \left(1 - \frac{OF(S,Z,M,L_{L \times 1})}{L_t}\right) + w \times PF(\mathbf{Z}) \quad (9.12)$$

Where the  $L_t$  and  $w$  are the total length of the feeder, including the branches and weight of the penalty function, respectively.

## 9.3. Simulation results and analysis

### 9.3.1. Test network

To verify the feasibility, effectiveness, and robustness of the proposed placement of TW observers, a modified IEEE 34-bus test feeder was studied. The tested network shown in Figure 7.3 was a radial distribution network. The total length of the network was equal to 93.913 km and consisted of 34 buses. All the lines were considered to have the same characteristic impedance.

### 9.3.2. Optimisation parameter setting

For a relatively low number of observers, the best solution can be found through an exhaustive search of the feasible solutions. The number of feasible solutions is equal to the binomial coefficient (combinatorial number):

$$C_P = \binom{N}{P} \quad (9.13)$$

Where  $P$  is equal to the number of observers and  $N$  is the number of buses. To place seven observers into the 34-bus network, the number of feasible solutions is equal to:

$$C_7 = \binom{34}{7} = 5,379,616 \quad (9.14)$$

An exhaustive search for the viable solutions, and the proposed optimisation method was used for  $P = 3$  to  $P = 7$ . The results were compared to determine the best optimisation penalty function weight ( $w$ ). Based on this comparison, the  $w$  was set to 0.5 to ensure the number of observers was constrained as required. For higher numbers of observers, where an exhaustive search was not practical, BPSO was preferable. The parameters used in BPSO are summarised in Table 9.1.

**Table 9.1. Parameters of binary particle swarm optimisation**

<b>Particle size</b>		1,000
<b>Number of iterations</b>		700
<b>Threshold (<math>\beta</math>)</b>	Scenario 1	0.50
	Scenario 2	0.30
	Scenario 3	0.01
<b>Penalty function weight (<math>w</math>)</b>		0.50

The particle size was set to 1,000 to increase diversity. It was assumed that all the lines had an equal characteristic impedance. Therefore, the refraction of all the T-junctions was equal to 0.66. Figure 9.2 shows the optimum placement of the TW observers for  $P = 7$  to  $P = 12$  and the total length of lines ( $OF$ ) that were observable and locatable. More than one optimum solution may be available. For example, where nine observers are required ( $P = 9$ ), a single observer can be placed in any of the buses 31, 32 or 33 without changing the  $OF$ . The network was fully observable and locatable for  $P = 12$ . The results for  $\beta = 0.3$  and  $P = 7$  to  $P = 10$  are shown in Figure 9.3. With the same number of observers, the  $OF$  increased as the  $\beta$  decreased for the low number of observers. Total network coverage was achieved with 10 observers ( $P = 10$ ). Figure 9.4 shows the per unit cost of a fault location system versus the number of observers for different threshold values.

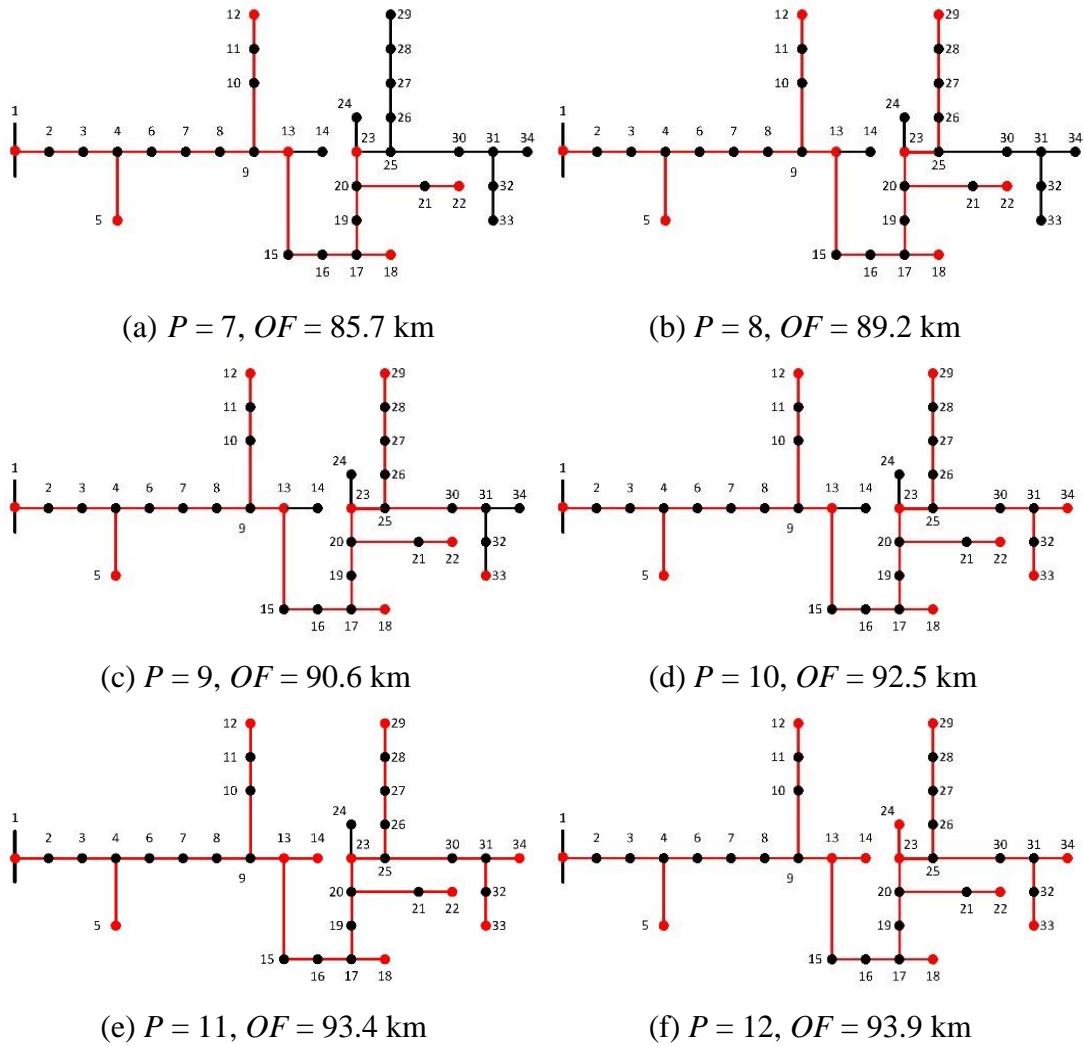


**Figure 9.2. The optimum placement of travelling wave observers for  $\beta = 0.5$ . The red lines are observable and locatable. The travelling wave observers were placed at the buses shown in red.**

As shown by Figure 9.4, the cost per unit length of observable and locatable lines increased as the number of observers increased. However, the required number of observers for fully observable and locatable networks did not decrease as  $\beta$  decreased below 0.3. The required minimum number of observers for a fully observable and locatable network will be determined by the number of branches on the network. By decreasing the  $\beta$  to 0.01, the  $OF$  was improved for the  $P = 3$  to  $P = 5$ . For a higher number of observers, the result was not different from the  $\beta = 0.3$  cases. Where  $\beta = 0.01$ , a fault's original TW can be detected by all observers in a tested network.

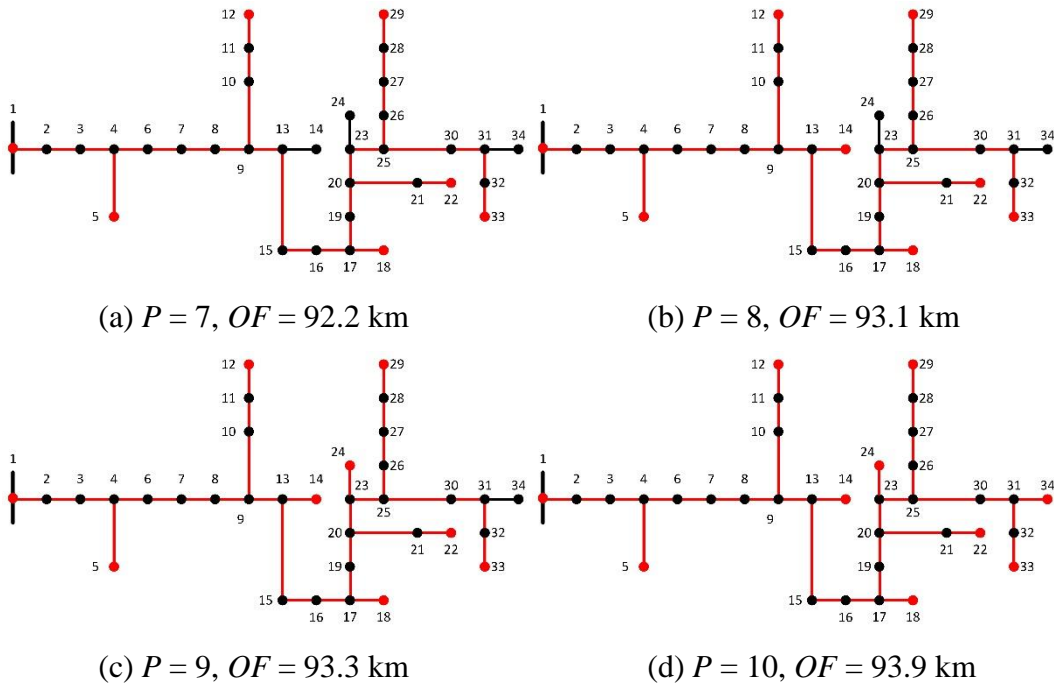


**Figure 9.3. The optimum placement of travelling wave observers for  $\beta = 0.3$ . The red lines are observable and locatable. The travelling wave observers were placed at the buses shown in red.**

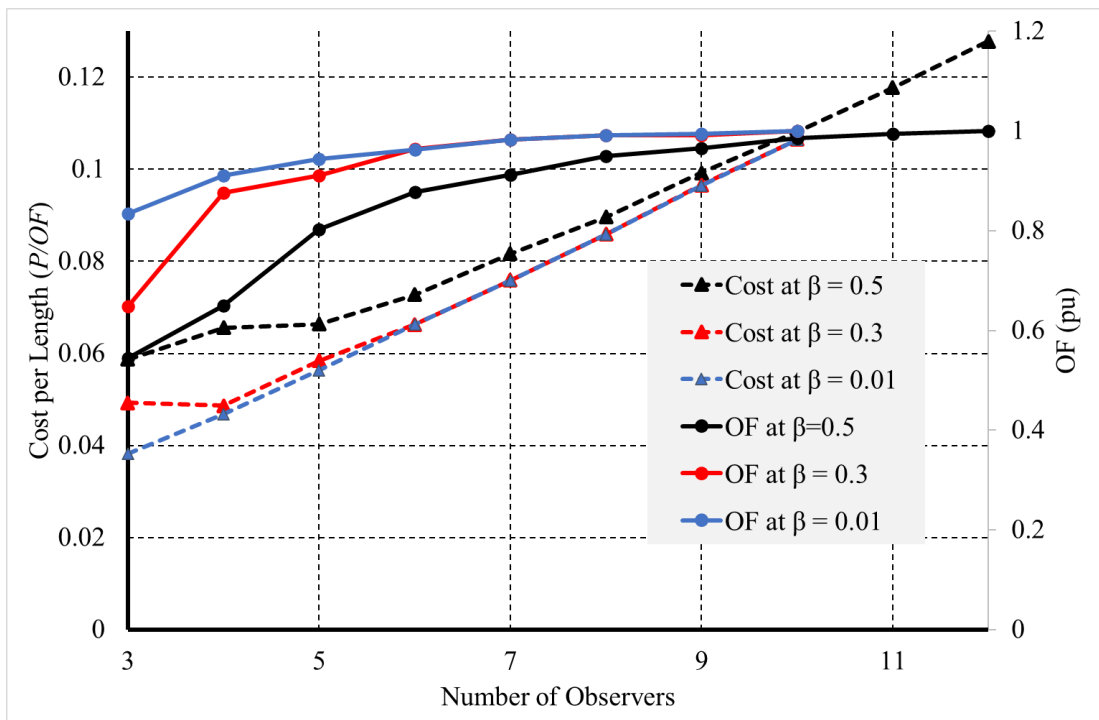


**Figure 9.4. The cost per length of fault-detectable and observable lines versus the number of observers.**

#### **9.4. Summary**

This chapter presents a new strategy to place a given number of travelling wave observers in a radial distribution network to maximize the observable and locatable lines in the network. The proposed method can be used for a cost-effective design of voltage TW based fault location schemes in radial distribution networks. Results show that the cost per length of fault location system is a function of TW observer sensitivity ( $\beta$ ), the number of observers and number of laterals.



# Chapter 10

## Travelling wave detector hardware

*Contents of this chapter is published in the 2016 Australasian Universities Power Engineering Conference (AUPEC),*

### **10.1. Introduction**

With the ever-reducing cost of high-speed microprocessors, digital signal processors and GPS chipsets, it is possible to develop a relatively small and low-cost voltage TW detector. Previous work has demonstrated that HIF location using distributed voltage TW detection and time sampling is feasible [121]. TWs propagate at close to the speed of light or 300 m/ $\mu$ s. A resolution of a few hundred meters is desirable to localise distribution faults sufficiently. A high-speed data acquisition (capable of a few mega samples per second) is required to study TW-based fault detection and location in real distribution networks. The recent feeder protection relays can capture transient events. However, their sampling rate is limited to a few kilo-samples per second.

Moreover, commercial electromagnetic or wound voltage transformers have very limited bandwidths and are not suitable for capturing high-speed front TWs. The main problem is the high number (more than 1,000) of HV winding turns required given the relatively small transformer core area available in a practically sized voltage transformer. The winding leakage inductances and capacitances become enough to form an effective low-pass filter.

Current transformers have far fewer turns, and their bandwidths can often extend into the higher frequency ranges. The improved bandwidth of current transformers has spurred some interest in the study of current rather than voltage TWs [29]. Voltage and current TWs are identical but scaled by the line's characteristic impedance. In the case of HIF, this fundamental principle for wave propagation on transmission lines still holds true. There is no major difference between using current or voltage TWs for locating faults. Instead, the issue is the availability of a high bandwidth transducer.

Other important types of transducers include the Rogowski coil, which is a current transducer capable of extreme bandwidth (often tens of megahertz), and the capacitive voltage transformer (CVT). CVTs are widely applied in power systems above 50 kV, and the number of turns required in a wound voltage transformer is uneconomical. A HV CVT will generally have a capacitive voltage divider stage that reduces the HV input to a few kilovolts or tens of kilovolts, followed by a wound voltage transformer to step the output voltage down to, typically, 110 VAC. The capacitive divider stage has an extremely high bandwidth. The principal requirement is the availability of a high-quality HV capacitor to form the first element of the divider. In a power system, CVT uses a physical lumped capacitor. It is also possible to use a parasitic capacitance between a line and an antenna to form the first capacitor. This approach is adopted in this thesis.

Chapter 10 describes the hardware that was developed to record voltage TWs in distribution networks. The hardware was designed at the Central Queensland University by Professor Peter Wolfs and is outside the scope of this thesis. The hardware specifications, detection algorithm and voltage sensors were designed and tested on a real distribution network as part of this research project at Curtin University, West Australia.

## **10.2. Prototype hardware**

The hardware block diagram is shown in Figure 10.1. The hardware consisted of three subsystems: an external antenna and front-end filters, a data acquisition, and a TW detector. The antenna signals were processed by an analogue receiver and supplied to the detector and an independent data system that captured the raw data as an aid to the system's development and evaluation.

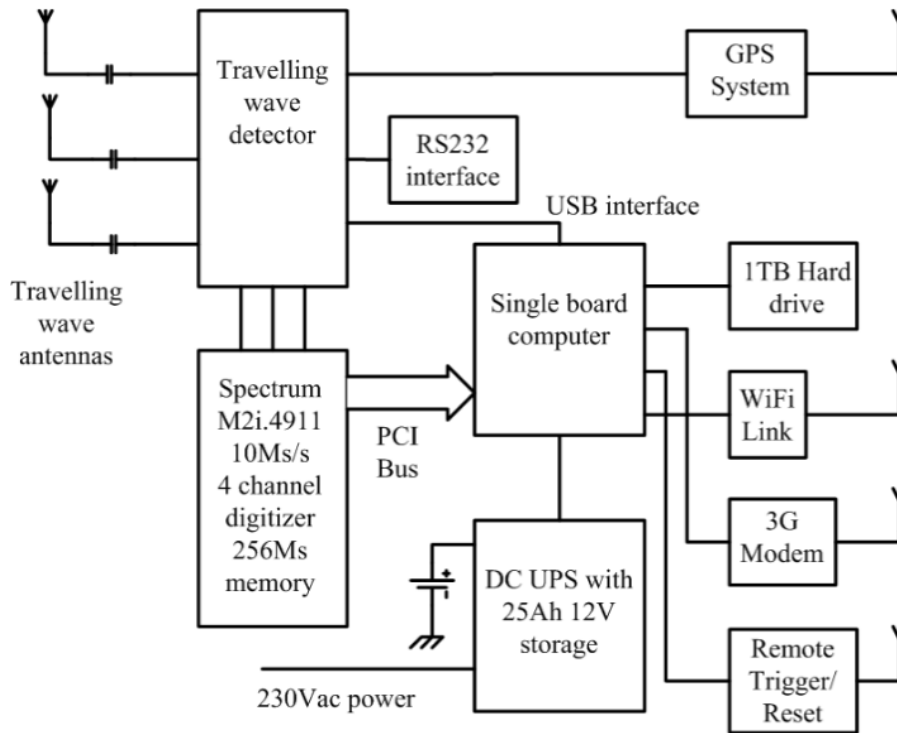


**Figure 10.1. A diagram of the hardware block.**

The detector was based on the Texas Instruments Delfino 28377 processor. The detector had access to GPS signals for timing purposes and was connected via a USB port to a single-board computer system. This allowed data transfer and control. The power supply required a 230 VAC input and was based on a DC uninterruptable power supply with a 12 V sealed lead-acid battery.

The single-board computer used an Advantech AIMB-213 motherboard with a LINUX operating system. It had a 250 GB hard drive for the operating system and a 1 TB external hard drive for data storage. The high-speed data acquisition system was a PCI-based four-channel acquisition card with a sample rate of 10 Ms/s on each channel. The card had 256 Ms of storage onboard. The data system could be remotely triggered and the data downloaded using a local Wi-Fi or 3G network connection.

The antennas were mounted 1.5 m below the line conductors. The antennas voltage was applied to two independent wide bandwidth amplifiers and antialiasing filters. The TW system was capable of samples at 1.5 Ms/s and the high-speed data system sampled at 10 Ms/s.

### ***10.2.1. External antenna and front-end filters***

The TW detector used three external capacitively-coupled antennas to detect the electrical fields of TWs. This facilitated the installation and reduced the cost. The

Australian overhead line construction standards for a 22 kV network allowed equipment that was not related to the power system, such as cable television network equipment, to be installed 1.5 m below the conductors.

Overhead distribution lines can be constructed as single-phase or multiphase. The main or backbone feeder is commonly three-phase. Figure 10.2 shows the placement of the three-phase conductors A, B, and C above the earth. The short 500 mm conductive antennas, D, E, and F, were placed at a distance ( $h_2$ ) under the phase conductors.

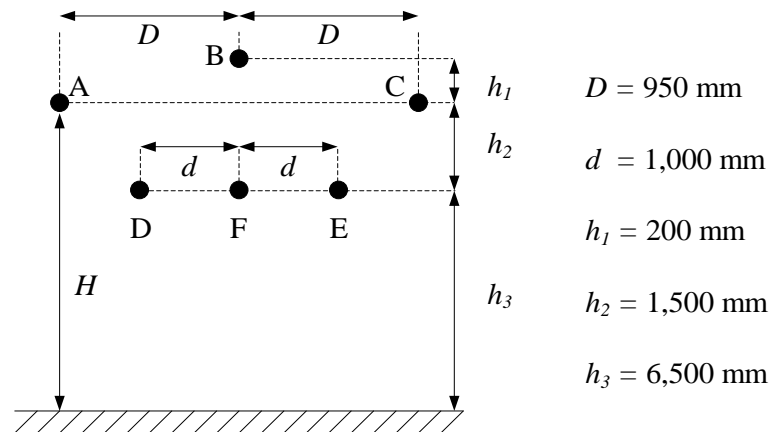


**Figure 10.2. The placement of antennas and the phase conductor configurations on a typical 22 kV distribution pole.**

There was a capacitive impedance between the conductors and between the conductors and the ground. The equivalent capacitors formed between the overhead conductors, antennas and ground are shown in Figure 10.3. The capacitance between two conductors with a length of  $l$  is given by:

$$C = \frac{2\pi\epsilon_0\epsilon_r l}{\ln\left(\frac{D}{r_1 r_2}\right)} \quad (10.1)$$

The capacitance to ground of conductors with a length of  $l$  is given by:

$$C = \frac{2\pi\epsilon_0\epsilon_r l}{\ln\left(\frac{2D}{r_1}\right)} \quad (10.2)$$

Where:

- $D$  is the distance between the conductor centres.
- $r_1$  and  $r_2$  are the conductor's radii.
- $\epsilon_0$  is the free space permittivity.
- $\epsilon_r$  is the dielectric relevant permittivity.

Consider the antenna connected to the instrument input with an impedance to ground of  $Z_{IN}$ .

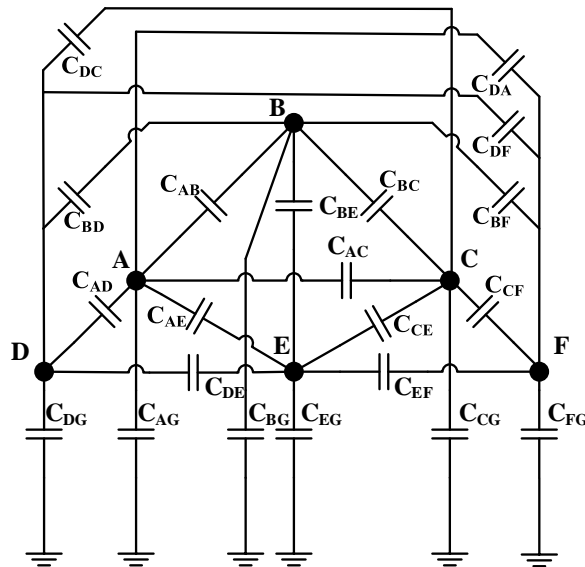


**Figure 10.3.** The lumped capacitors between the overhead conductors, antennas, and ground (A, B and C are the phase conductors, and D, E and F are the antennas).

The instrument measures the antenna's voltage to the ground. Figure 10.4 illustrates the equivalent circuit of the equipment input channel.

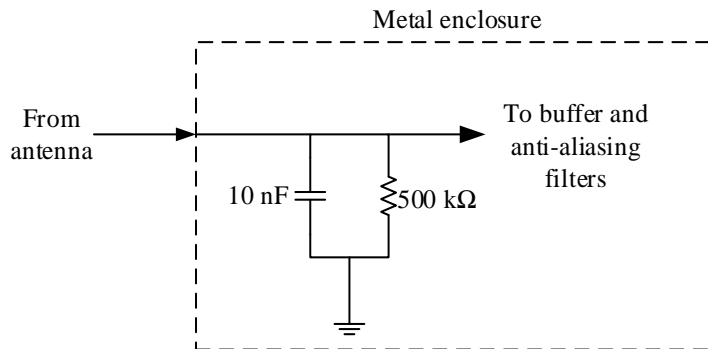


**Figure 10.4.** An input channel equivalent circuit.

The voltage to ground at the instrument input can be determined as the sum of the responses to each phase voltage by using the superposition theorem. Figure 10.5 illustrates the equivalent circuit model between phase A and the antennas, where all the other phases are connected to the ground.

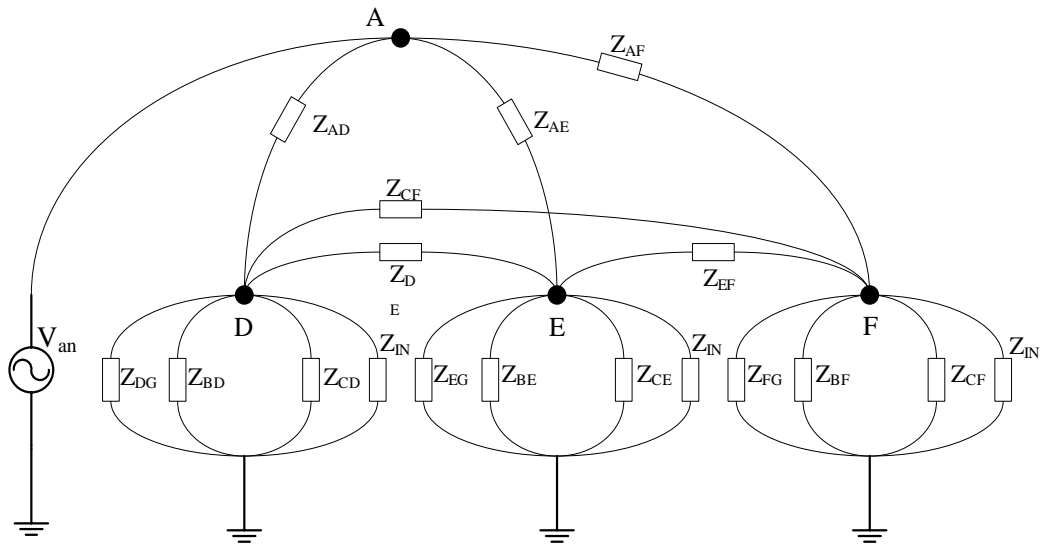


**Figure 10.5. An equivalent electrical circuit model between phase A and the antennas.**

The  $Z_{ij}$  is the capacitive impedance between phase/antenna  $i$  and phase/antenna  $j$ . The capacitive couplings from the phases to the antennas were calculated to be approximately 1 pF. A divider of 10,000:1 was formed in conjunction with the 10 nF capacitor at the instrument input. The capacitive coupling impedance between the antenna and ground was ignored, and the impedance to the ground was dominated by  $Z_{IN}$ . The circuit was then simplified (see Figure 10.6).

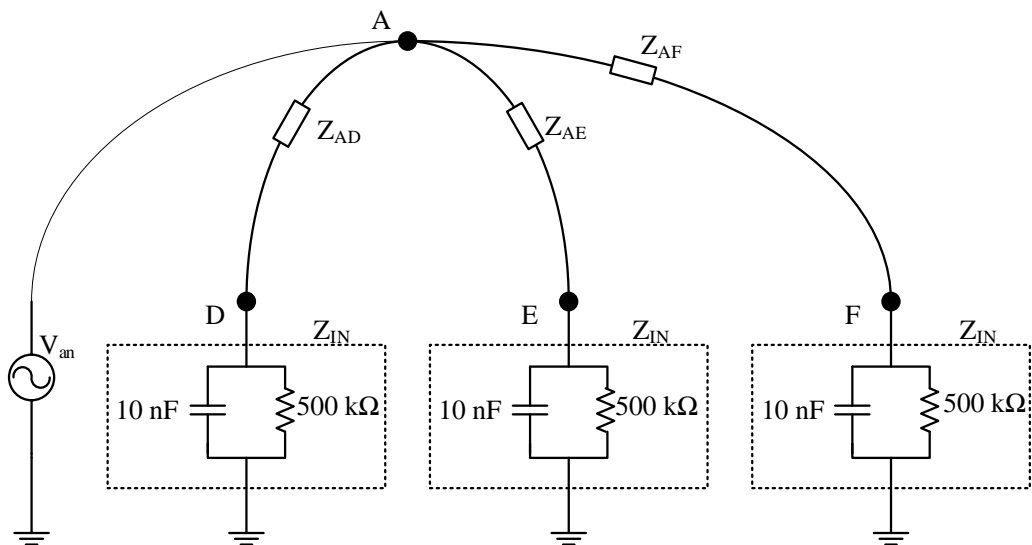


**Figure 10.6. A simplified equivalent circuit between phase A and the antennas.**

From Figure 10.6, the antennas' voltage to ground ( $V_{DG}, V_{EG}, V_{FG}$ ) due to the capacitive coupling to the A conductor was described with a simple voltage divider. The CVTs were linear and superposition applied. The total CVT outputs were super-positioned to the responses of the three-phase voltages on the three overhead lines. Because of the parallel  $500\text{ k}\Omega$  resistor, the voltage divider ratio varied with frequency. The  $10\text{ nF}$  capacitor and the  $500\text{ k}\Omega$  resistor had a time constant of  $5\text{ ms}$ . The CVT had a first-order high-pass characteristic of  $200\text{ rad/s}$  or  $31.8\text{ Hz}$ . This affected the CVT ratios at the power frequency; however, this was not the intended range of operation. For frequencies much higher than the power frequency, the CVT ratios determined by the capacitors as only  $10\text{ nF}$  capacitive reactance were significantly lower than the  $500\text{ k}\Omega$  resistor.

The coupling capacitive impedance was estimated to be around  $1\text{ pF}$ . The transfer function of the applied phase A voltage to D antenna's voltage was defined by:

$$H_{AD}(j\omega) = \frac{v_{DG}(j\omega)}{v_{an}(j\omega)} \quad (10.3)$$

Figure 10.7 shows the bode diagram of the transfer function,  $H_{AD}(j\omega)$ .

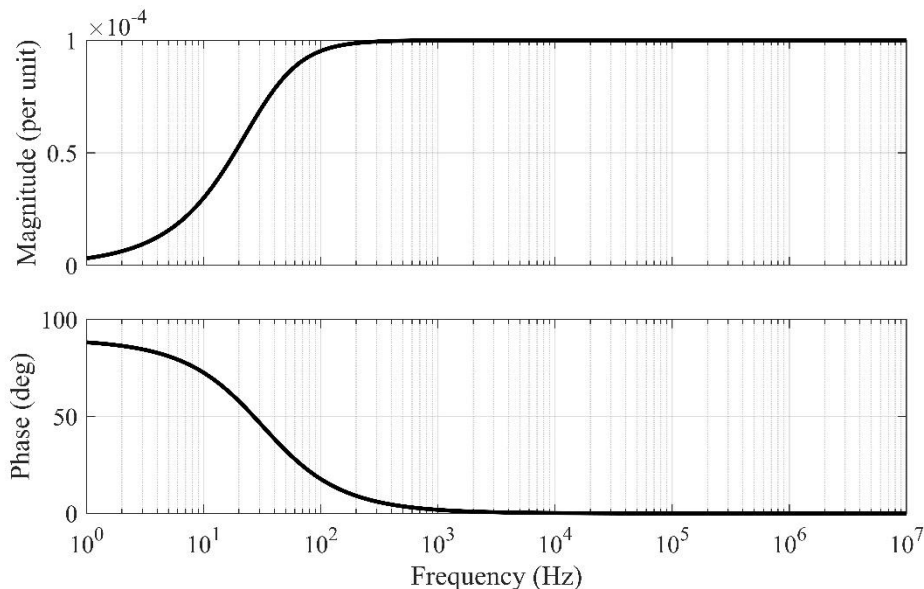


**Figure 10.7. The bode diagram of  $H_{AD}(j\omega)$  ( $Z_{AD} = 1\text{ pF}$ ).**

As expected, the equivalent circuit behaved like a high-pass filter and a voltage divider. The transfer function magnitude was the voltage divider ratio. The voltage divider ratio for the high-frequency, flat area in the bode plot was equal to  $1 \times 10^{-4}$ . This ratio was estimated and was significantly affected by the antennas' end effects

(because they were short) and the construction of the antennas; the antennas had a spiral element on a plastic tube former rather than a solid cylinder. Similarly, the equivalent circuit between the phase B and C can be drawn. The following equation describes the relation of the antennas and overhead conductors' voltage to the ground:

$$\begin{bmatrix} V_{DG}(j\omega) \\ V_{EG}(j\omega) \\ V_{FG}(j\omega) \end{bmatrix} = \begin{bmatrix} H_{AD}(j\omega) & H_{BD}(j\omega) & H_{CD}(j\omega) \\ H_{AE}(j\omega) & H_{AE}(j\omega) & H_{AE}(j\omega) \\ H_{AF}(j\omega) & H_{AF}(j\omega) & H_{AF}(j\omega) \end{bmatrix} \times \begin{bmatrix} V_{AG}(j\omega) \\ V_{BG}(j\omega) \\ V_{CG}(j\omega) \end{bmatrix} \quad (10.4)$$

$$= H(j\omega) \cdot V(j\omega)$$

The signal frequency was significantly higher than the power frequency, the element of  $H(j\omega)$  was constant, and the phase angle was negligible. Therefore, equation (10.4) can be written as:

$$\begin{bmatrix} V_{DG} \\ V_{EG} \\ V_{FG} \end{bmatrix} = \begin{bmatrix} H_{AD} & H_{BD} & H_{CD} \\ H_{AE} & H_{AE} & H_{AE} \\ H_{AF} & H_{AF} & H_{AF} \end{bmatrix} \times \begin{bmatrix} V_{AG} \\ V_{BG} \\ V_{CG} \end{bmatrix} = \mathbf{H} \cdot \mathbf{V}_{ABC} \quad (10.5)$$

The voltage of the overhead lines can be related to the antenna voltage as:

$$\begin{bmatrix} V_{AG} \\ V_{BG} \\ V_{CG} \end{bmatrix} = H^{-1} \times \begin{bmatrix} V_{DG} \\ V_{EG} \\ V_{FG} \end{bmatrix} = \mathbf{H}^{-1} \cdot \mathbf{V}_{DEF} \quad (10.6)$$

For the dimensions given in Figure 10.2, the  $H^{-1}$  is equal to:

$$\mathbf{H}^{-1} = \begin{bmatrix} 0.8908 & -1.0218 & 0.1862 \\ -1.1336 & 2.5033 & -1.1336 \\ 0.1862 & -1.0218 & 0.8908 \end{bmatrix} \times 10^4 \quad (10.7)$$

The magnitude of the higher-frequency components of the voltage transient can be estimated using the  $\mathbf{H}^{-1}$  and measuring the antennas voltage to the ground. The dividers outputs were applied to two independent wide bandwidth amplifiers and antialiasing filters (see Figure 10.8).

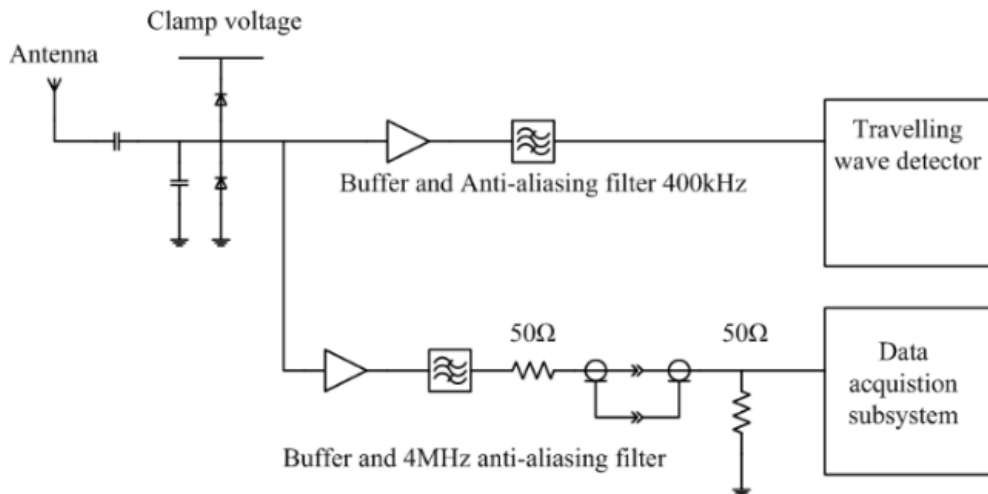


**Figure 10.8. An overview of the overall system.**



### 10.3. High voltage laboratory testing

The developed TW detector tested in the HV laboratories was owned by Western Power (a West Australian network operator). This testing was undertaken to confirm the operation of the CVT and data acquisition system at power frequency. Figure 10.9 shows the equipment under test at the Western Power HV test facility. The three-phase 22 kV was generated using the three 22 kV/0.110 kV voltage transformer. The effects of each conductor were tested by energising one overhead conductor at a time.



**Figure 10.9. The equipment under test at the Western Power high voltage laboratory.**

The CVT voltage measurement method is designed to detect higher frequency waveforms. The line frequency components were below the designed frequency range. Consequently, the power frequency scaling factors were affected by the impedances of the measuring channels. The accuracy of 50 Hz is low. The transducers have higher gains for the harmonic frequencies. The third and fifth harmonic gains are roughly three and five times higher. This accentuated any harmonic distortion, and the voltage waveforms appeared more distorted than they actually were. The laboratory results are shown in Figure 10.10.

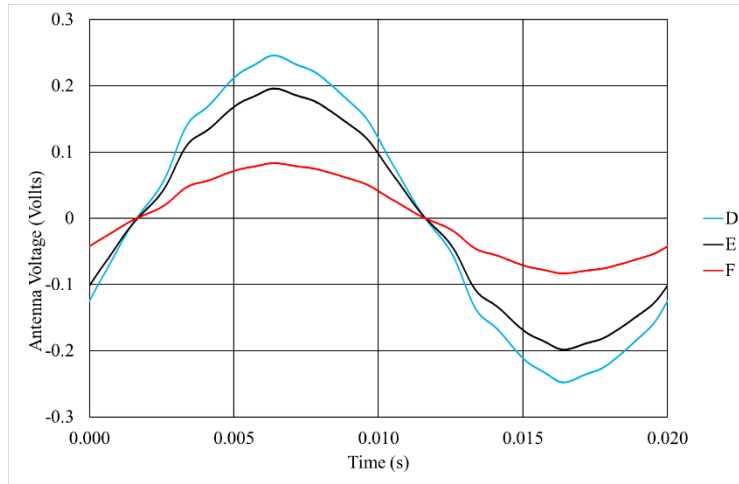
The 22 kV voltage transformer source had a high source impedance and moderate underlying harmonic distortion. The test waveforms were not harmonically pure, and the CVT measurement system accentuated the harmonics. As expected, the antenna voltage magnitude was higher for the antennas that were closer to the energised conductor. The voltage magnitude noticeably reduced for the antennas, which were further from the energised overhead conductor. The voltage magnitude of antenna D (see Figure 10.10 (a)) was expected to be equal to the voltage magnitude of antenna F (see Figure 10.10 (c)). However, there was a significant difference between them. The largest sources of error may be related to:

- the use of the CVT system below its designed frequency range
- the positioning of the antennas below the overhead conductors
- possible differences in parasitic capacitances from the antennas to ground.

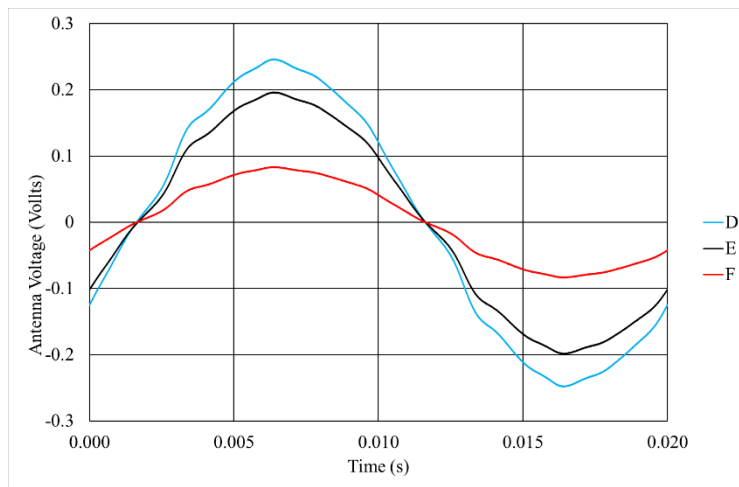
The antenna to ground capacitances were affected by equipment in the workspace. Figure 10.11 shows the antennas' voltage when the three-phase was connected to the overhead conductor. In this case, the antenna voltages were the superimposition of the effects of each of the three phases. There was substantial cancellation at the centre antenna, which was strongly coupled to all three phases.

#### **10.4. Field trial**

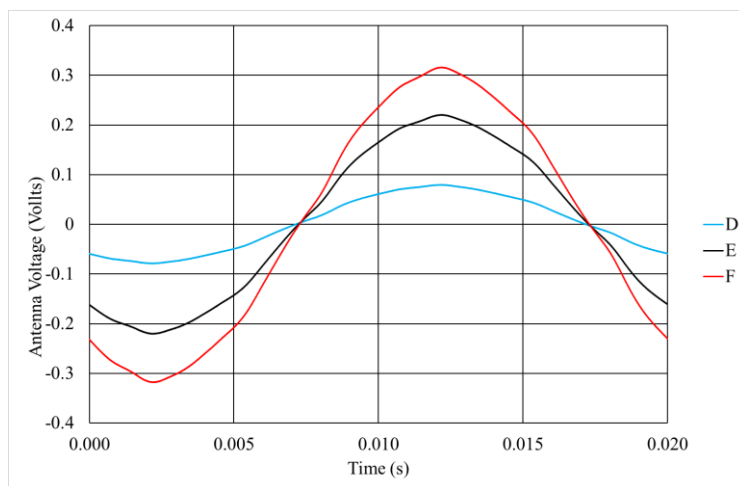
The developed TW detector was subsequently installed in the MV distribution network owned by Western Power. Figure 10.12 shows the TW prototype installed at the 22 kV rural distribution network. There was a limited possibility to do some field testing for a brief period with one system. The focus of this testing was to demonstrate that the detector could capture high-frequency power line transients. There were physical constraints placed upon the testing program.



(a)



(b)



(c)

**Figure 10.10. The recorded voltages when: (a) the A conductor was energised; (b) the B conductor was energised; and (c) the C conductor was energised.**

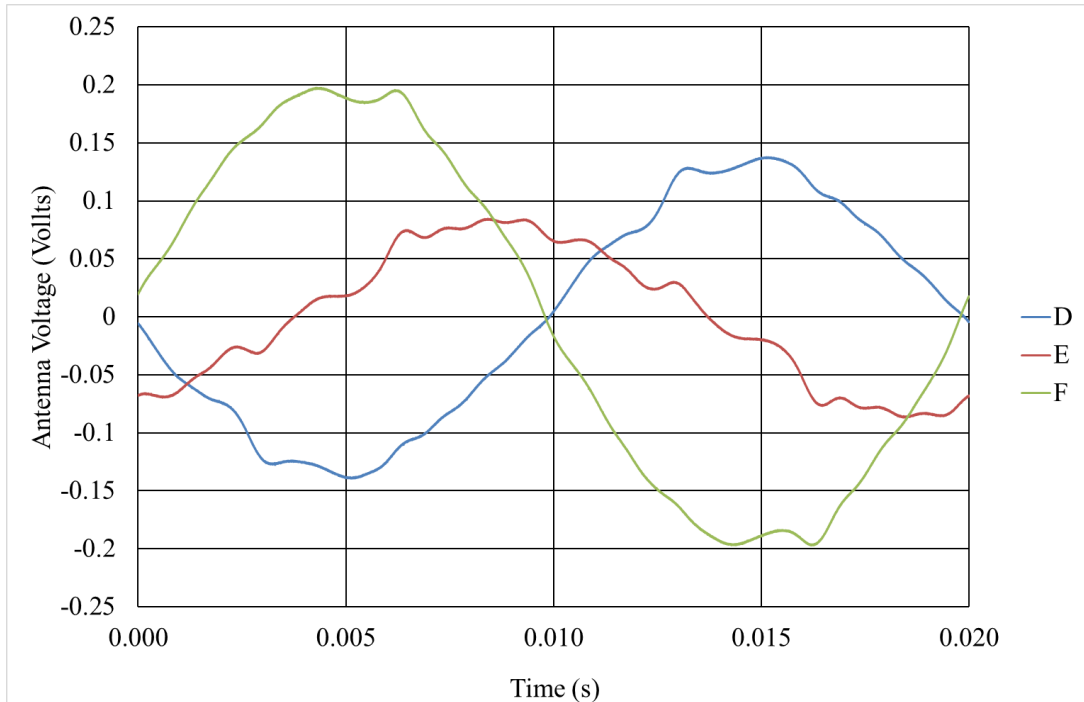


**Figure 10.11. The antenna voltages when the 22 kV three-phase was connected to the overhead conductors.**



**Figure 10.12. The travelling wave detector prototype installed on the medium voltage distribution network.**

Western Power did not create a controlled simulated fault during these tests. Although it may have been possible, considerable resources and planning would be required to address any potential safety and operational issues. Additionally, the

detector had to be removed from the network before the fire season and could only be installed for a few months. Therefore, the test relied on naturally occurring phenomena and some transients induced through normal network switching operations.

The test program progressed as follows. The TW wave detector was disabled. However, the data acquisition system was programmed to function as the TW detector and event recorder to test the TW detector algorithm. It constantly sampled the antenna's voltage at a 1.5 MHz sampling rate and reconstructed the phase voltages. The phase voltages fed into the TW detection algorithm (see Section 6.6). The recorded data also included one cycle before the event and the event's precise time information.

Naturally occurring faults were not captured during the three-month field trial by the reclosers, which were relatively close to the observer. The field test attempted to find a correlation between the faults detected by conventional protection relays or reclosers and events recorded by the observer. The recorded waveforms demonstrate the ability of the detector to detect TWs and record event waveforms at the desired sampling rate.

Figure 10.13 provides examples of the recorded waveforms. It is not possible to confidently classify the events shown in Figure 10.13. The waveforms shown in Figure 10.13(a) may have occurred during the phase-to-phase faults. The high-frequency components appearing in Figure 10.13(b) signal the existence of high impedance arcs. Similarly, Ghaderi et al. also reported a high-frequency component at the phase currents [54]. A single-phase capacitor, cable switching or switching a two-phase load could have caused the transient in Figure 10.13(c).

The observer input high-pass filter exaggerated the ratio of the transient to power the frequency magnitude. As the recorded waveforms suggest, faults and sudden changes in power systems can create TWs. Therefore, the classification algorithm was required to distinguish faults from the other disturbances. However, the focus of this research was on the location of faults, and classification was not part of the algorithm.

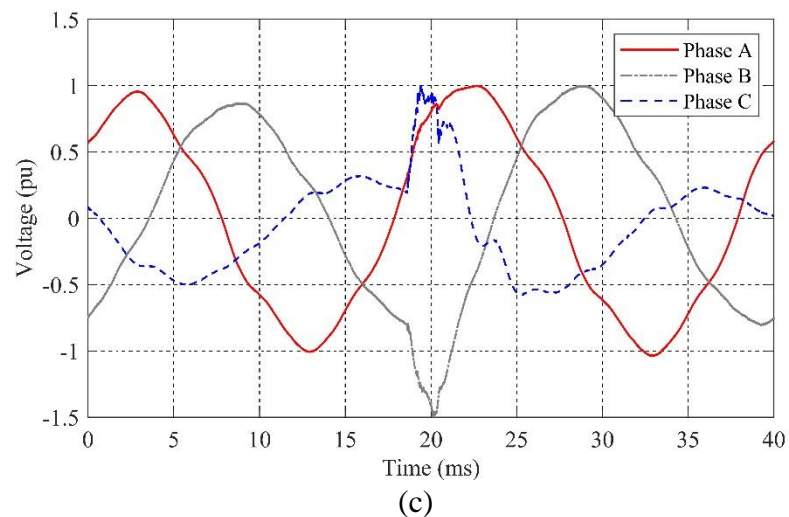
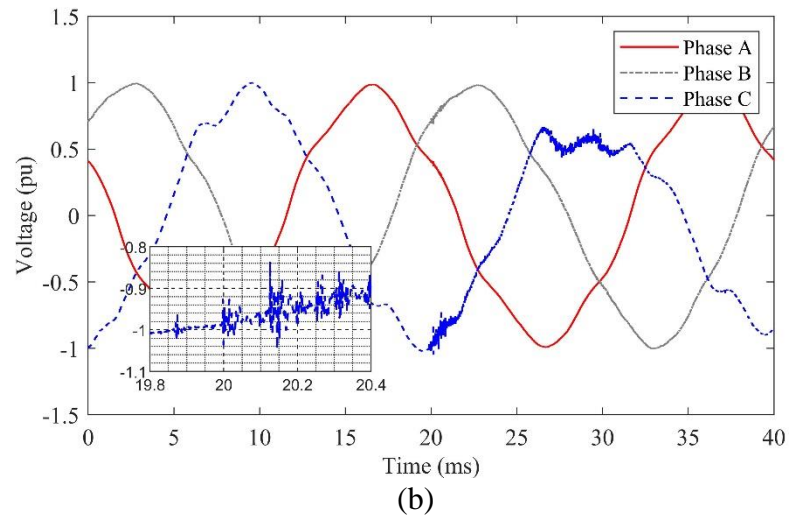
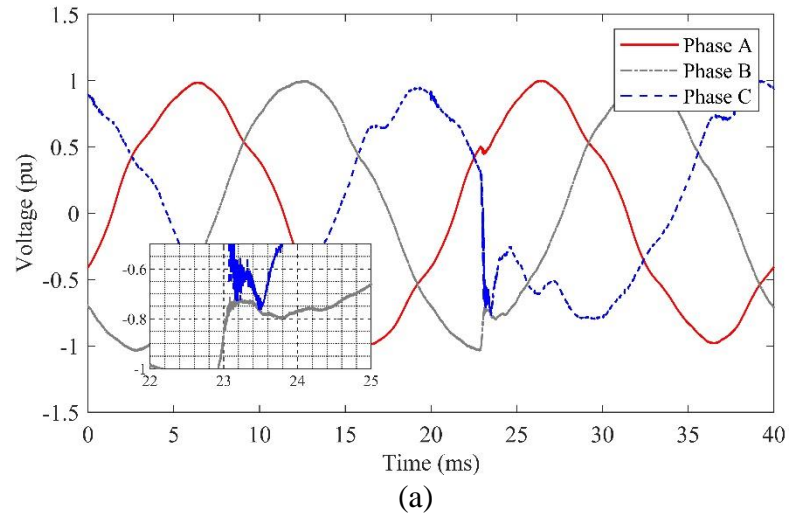


**Figure 10.13. The captured waveforms during the field trial, showing: (a) a possible line-to-line fault; (b) a high-frequency component that might have been caused by an arc; and (c) a lower-frequency transient caused by the two-phase load or capacitor switching.**

## **10.5. Summary**

This chapter presents a hardware prototype capable of acting as a travelling wave detector and data recording system. The system is pole mounted and utilizes capacitive coupling between the phase conductors and three antennas to capture the travelling wave signals. Moreover, field trial results are also presented in this chapter.



# Chapter 11

## Concluding remarks and further study

This thesis has discussed the development of a TW-based solution to the fault location problem in radial distribution networks. The work is applicable for HIFs and temporary faults, such as conductor clashing. The optimal placement of TW observers for fault observability and locatability was examined. The effect of distributing transformers upon the accuracy of fault location was studied, and compensation methods were proposed.

### **11.1. Concluding remarks**

This thesis considered the problem of rapidly and accurately identifying temporary faults and HIFs using synchronised voltage TW observers that were optimally placed across a distribution network. The developed method relies on time-stamping TWs at nodes, which are equipped with time-synchronised sensors. The thesis presented an optimal placement procedure that ensured the unique localisation of faults appearing in distribution networks. Further, the adverse effects of distribution transformers for estimating travelling times and inaccuracies of the developed fault location technique were eliminated by considering the effects of transformers on the travelling time along the feeder.

#### ***11.1.1. Travelling wave-based high impedance fault location in radial distribution networks***



The salient contribution of this study was to develop a novel computational approach to high impedance and temporary fault location in distribution networks. An optimally distributed time-synchronised sensor in a power network was deployed to time-stamp the incident wave arrival times at the sensor's location after the occurrence of a fault. The fault's location was then estimated using the recorded arrival times of the incident waves at the observer.

The time-synchronised voltage TW observers were optimally placed. For a given number of observers, fault detection and location was achieved over the longest possible length of the protected feeder.

#### ***11.1.2. Enhancement of the proposed fault location algorithm's accuracy***

This thesis extensively studied the modelling of transformers and concluded that the parasitic capacitances within a transformer contribute to propagation delays of TWs. It has been demonstrated, using a simulation and laboratory testing, that the parasitic capacitance increases the incident wave's travel time on the feeders. A procedure was developed to compensate for the transformer's delay effect when estimating the fault's location.

#### ***11.1.3. Optimal development of synchronised voltage travelling wave sensors***

This study provided a strategy for rendering the distribution observable and locatable (from a HIF location point of view) utilising optimally placed TW observers in distribution networks. Consequently, the length of the observable and locatable lines was maximised for the given number of observers.

### **11.2. Further study**

Section 11.2 recommends future studies that intend to provide practical applications for TW fault location in distribution networks.

#### ***11.2.1. Investigate novel online travelling wave arrival detection methods***

Although various technologies have been developed to detect fault-induced transients in power systems, more appropriate methods for online application are worth further investigation. Distributed observers are required to be low-cost; therefore, the developed algorithm should be efficient and capable of handling the computational burden and memory allocation.

### ***11.2.2. Investigate novel transient classification algorithms***

Any sudden changes in the state of power systems will induce TWs that could trigger transient detectors. The transient's classification technique allows discrimination between distinct types of faults. This information can reduce the time to repair faults and can ensure more appropriate repairs are made. For example, conductor clashing should excite aerial mode waves with no ground mode waves, but a HIF will produce both aerial and ground modes.

### ***11.2.3. Field trial and simulation of various fault types***

There were limited field-testing opportunities during the term of the thesis. Only one observer was available, and it was not possible to stage tests with known faults. The developed observer captured many high-frequency transient waveforms during the field trial. However, given the restrictions imposed, it was difficult to confidently classify the events based on the simulation and theories due to several variables and the complexity of distribution networks. Therefore, a specifically designed field trial is required to train the classification algorithm and test the transient detection method.

### ***11.2.4. Hardware improvements***

Hardware design was outside the scope of this thesis. However, access to the hardware provided an opportunity to demonstrate the workability of some aspects of the solution, such as using CVTs to capture high-frequency events. The key issue to resolve for commercialising the TW HIF location technology is the power supply and design of the small footprint hardware, which has the required computational power, storage, and communication capabilities.

### ***11.2.5. Fault location on medium direct current distribution network***

With the large expansion of renewable distributed generation and rapid development of power electronic technologies. The idea of DC distribution networks attracts more attention. DC fault detection, location and protection is one of the major challenges. The travelling wave arrival time could be detected by a high-speed current differential approach in the DC system. The application of fault location algorithm proposed in this thesis could be investigated for fault location in medium voltage radial distribution networks.

#### ***11.2.6. Fault location using re-closure generated travelling wave***

Circuit breakers generate a TW during switching operations. When permanent faults occur, the circuit breaker re-closure also generates a TW. The TW generated by the circuit breaker operation reflects from the fault location and contains the information of fault position. The time difference between the reclosing instant and the arrival instant of the reflected TW from the fault location can be employed to calculate the distance to the fault. The faulted lateral could be identified by comparing the high frequency components of recorded waveforms with a database that contain the high frequency components induced by faults and re-closure operation. This databased could be develop by simulation or from historical fault information.

#### ***11.2.7. Compensating for line length error due to ambient temperature changes***

Variations in the ambient temperature cause changes to the parameters of distribution lines. High temperature increases the actual length of the overhead lines. The line length expansion results in deeper sag between two power poles. The accuracy of TW method can be improved by compensating the line length variation due to temperature. The line catenary model that considers parameters of the tower and the actual temperature can be used to derive the actual line length.

## References

- [1] M. Tremblay, B. Fazio, and D. Valiquette, "Using voltage sag measurements for advanced fault location and condition-based maintenance," *CIREC - Open Access Proceedings Journal*, vol. 2017, no. 1, pp. 893-896, 2017, doi: 10.1049/oap-cired.2017.0066.
- [2] M. Abad, M. García-Gracia, N. E. Halabi, and D. L. Andía, "Network impulse response based-on fault location method for fault location in power distribution systems," *IET Generation, Transmission & Distribution*, vol. 10, no. 15, pp. 3962-3970, 2016, doi: 10.1049/iet-gtd.2016.0765.
- [3] A. Robertson. "Investigators confirm that PG&E power lines started the deadly Camp Fire." The Verge. <https://www.theverge.com/2019/5/15/18626819/cal-fire-pacific-gas-and-electric-camp-fire-power-lines-cause> (accessed 26/05/2020, 2020).
- [4] "REFCL Trial: Ignition Tests," marxsen consulting, Beaumaris VIC 3193, 2014.
- [5] S. Pascoe, "The 2009 Victorian Bushfires Royal Commission: Lessons for the Conduct of Inquiries in Australia," *Australian Journal of Public Administration*, vol. 69, no. 4, pp. 392-400, 2010, doi: 10.1111/j.1467-8500.2010.00702.x.

- [6] R. Niven. "Melbourne: Black Saturday's fires could be all too easily forgotten." The Guardian. <https://www.theguardian.com/cities/2014/feb/06/melbourne-black-saturday-fires-bushfires-2009-anniversary> (accessed 2020).
- [7] "Final Electrical Incident Report – Bushfire near River and Folewood Roads, Toodyay, Western Australia 29 December 2009," EnergySafety WA. [Online]. Available: [https://www.commerce.wa.gov.au/sites/default/files/atoms/files/toodyay\\_fire\\_dec\\_2009\\_iss\\_aug\\_2010.pdf](https://www.commerce.wa.gov.au/sites/default/files/atoms/files/toodyay_fire_dec_2009_iss_aug_2010.pdf)
- [8] "Final Electrical Incident Report – Power Line Fault and Bushfire near Brindle Road, Parkerville, Western Australia 3 January 2008," Energy Safety WA, 11 January 2008 2008.
- [9] S. Robson, A. Haddad, and H. Griffiths, "Fault Location on Branched Networks Using a Multiended Approach," *IEEE Transactions on Power Delivery*, vol. 29, no. 4, pp. 1955-1963, 2014, doi: 10.1109/TPWRD.2014.2302137.
- [10] M. Korkali and A. Abur, "Optimal Deployment of Wide-Area Synchronized Measurements for Fault-Location Observability," *Power Systems, IEEE Transactions on*, vol. 28, no. 1, pp. 482-489, 2013, doi: 10.1109/TPWRS.2012.2197228.
- [11] Y. Dong, C. Zheng, and M. Kezunovic, "Enhancing Accuracy While Reducing Computation Complexity for Voltage-Sag-Based Distribution Fault Location," *Power Delivery, IEEE Transactions on*, vol. 28, no. 2, pp. 1202-1212, 2013, doi: 10.1109/TPWRD.2013.2247639.
- [12] K. Sridharan and N. N. Schulz, "Outage management through AMR systems using an intelligent data filter," *Power Delivery, IEEE Transactions on*, vol. 16, no. 4, pp. 669-675, 2001, doi: 10.1109/61.956755.

- [13] "IEEE Guide for Determining Fault Location on AC Transmission and Distribution Lines," *IEEE Std C37.114-2014 (Revision of IEEE Std C37.114-2004)*, pp. 1-76, 2015, doi: 10.1109/IEEESTD.2015.7024095.
- [14] A. A. Girgis, C. M. Fallon, and D. L. Lubkeman, "A fault location technique for rural distribution feeders," *Industry Applications, IEEE Transactions on*, vol. 29, no. 6, pp. 1170-1175, 1993, doi: 10.1109/28.259729.
- [15] Z. Jun, D. L. Lubkeman, and A. A. Girgis, "Automated fault location and diagnosis on electric power distribution feeders," *IEEE Transactions on Power Delivery*, vol. 12, no. 2, pp. 801-809, 1997, doi: 10.1109/61.584379.
- [16] R. H. Salim, M. Resener, A. D. Filomena, K. R. C. d. Oliveira, and A. S. Bretas, "Extended Fault-Location Formulation for Power Distribution Systems," *IEEE Transactions on Power Delivery*, vol. 24, no. 2, pp. 508-516, 2009, doi: 10.1109/TPWRD.2008.2002977.
- [17] S. M. Brahma, "Fault Location in Power Distribution System With Penetration of Distributed Generation," *IEEE Transactions on Power Delivery*, vol. 26, no. 3, pp. 1545-1553, 2011, doi: 10.1109/TPWRD.2011.2106146.
- [18] R. H. Salim, K. C. O. Salim, and A. S. Bretas, "Further improvements on impedance-based fault location for power distribution systems," *IET Generation, Transmission & Distribution*, vol. 5, no. 4, pp. 467-478, 2011, doi: 10.1049/iet-gtd.2010.0446.
- [19] L. Yuan, "Generalized Fault-Location Methods for Overhead Electric Distribution Systems," *Power Delivery, IEEE Transactions on*, vol. 26, no. 1, pp. 53-64, 2011, doi: 10.1109/TPWRD.2010.2057454.
- [20] G. Yanfeng and A. Guzmán, "Integrated fault location system for power distribution feeders," in *2012 Rural Electric Power Conference*, 15-17 April 2012 2012, pp. B6-1-B6-9, doi: 10.1109/REPCon.2012.6194570.

- [21] R. Dashti and J. Sadeh, "Applying Dynamic Load Estimation and Distributed-parameter Line Model to Enhance the Accuracy of Impedance-based Fault-location Methods for Power Distribution Networks," *Electric Power Components and Systems*, vol. 41, no. 14, pp. 1334-1362, 2013, doi: 10.1080/15325008.2013.819950.
- [22] R. Dashti and J. Sadeh, "Fault section estimation in power distribution network using impedance-based fault distance calculation and frequency spectrum analysis," *Generation, Transmission & Distribution, IET*, vol. 8, no. 8, pp. 1406-1417, 2014, doi: 10.1049/iet-gtd.2013.0633.
- [23] R. Dashti and J. Sadeh, "Accuracy improvement of impedance-based fault location method for power distribution network using distributed-parameter line model," *International Transactions on Electrical Energy Systems*, vol. 24, no. 3, pp. 318-334, 2014, doi: 10.1002/etep.1690.
- [24] J. U. N. d. Nunes and A. S. Bretas, "Extended impedance-based fault location formulation for active distribution systems," in *2016 IEEE Power and Energy Society General Meeting (PESGM)*, 17-21 July 2016 2016, pp. 1-5, doi: 10.1109/PESGM.2016.7741433.
- [25] K. R. C. De Oliveira, R. H. Salim, A. D. Filomena, M. Resener, and A. S. Bretas, "Unbalanced underground distribution systems fault detection and section estimation," vol. 4682, ed, 2007, pp. 1054-1065.
- [26] B. K. Stephen Marx, "Traveling Wave Fault Location in Protective Relays: Design, Testing, and Results," Schweitzer Engineering Laboratories, Idaho, 2013.
- [27] L. J. Lewis, "Traveling Wave Relations Applicable to Power-System Fault Locators," *American Institute of Electrical Engineers, Transactions of the*, vol. 70, no. 2, pp. 1671-1680, 1951, doi: 10.1109/T-AIEE.1951.5060615.

- [28] C. Zhang, G. Song, T. Wang, and L. Yang, "Single-Ended Traveling Wave Fault Location Method in DC Transmission Line Based on Wave Front Information," *IEEE Transactions on Power Delivery*, vol. 34, no. 5, pp. 2028-2038, 2019, doi: 10.1109/TPWRD.2019.2922654.
- [29] "POWER TRANSMISSION LINE FAULT LOCATION BASED ON CURRENT TRAVELING WAVES," Doctoral, Department of Electrical Engineering, Helsinki University of Technology (2008).
- [30] S. Shi, X. Dong, and S. Wang, "Traveling waves based protection relaying of power lines," in *Advanced Power System Automation and Protection (APAP), 2011 International Conference on*, 16-20 Oct. 2011 2011, vol. 3, pp. 2467-2471, doi: 10.1109/APAP.2011.6180658.
- [31] E. O. Schweitzer, A. Guzman, M. V. Mynam, V. Skendzic, B. Kasztenny, and S. Marx, "Locating faults by the traveling waves they launch," in *Protective Relay Engineers, 2014 67th Annual Conference for*, March 31 2014-April 3 2014 2014, pp. 95-110, doi: 10.1109/CPRE.2014.6798997.
- [32] K. J. Ferreira and A. E. Emanuel, "A Noninvasive Technique for Fault Detection and Location," *Power Delivery, IEEE Transactions on*, vol. 25, no. 4, pp. 3024-3034, 2010, doi: 10.1109/TPWRD.2010.2057455.
- [33] J. R. Leslie and K. H. Kidd, "The "linascope"-an echo-ranging type fault locator for high-voltage lines," *Transactions of the American Institute of Electrical Engineers*, vol. 67, no. 2, pp. 1162-1167, 1948, doi: 10.1109/T-AIEE.1948.5059796.
- [34] J. R. Leslie and K. H. Kidd, "The "Linscope" fault locator," *Electrical Engineering*, vol. 67, no. 10, pp. 987-987, 1948, doi: 10.1109/EE.1948.6444390.



- [35] K. H. Kidd, "The Linascope Transmission Line Fault Locator," *Transactions of the American Institute of Electrical Engineers*, vol. 70, no. 1, pp. 1008-1013, 1951, doi: 10.1109/T-AIEE.1951.5060516.
- [36] S. Shi, A. Lei, X. He, S. Mirsaeidi, and X. Dong, "Travelling waves-based fault location scheme for feeders in power distribution network," *The Journal of Engineering*, vol. 2018, no. 15, pp. 1326-1329, 2018, doi: 10.1049/joe.2018.0161.
- [37] W. Lin-Yong, H. Zheng-You, and Q. Qing-Quan, "A New Single Ended Fault Location Technique Using Travelling Wave Natural Frequencies," in *Power and Energy Engineering Conference, 2009. APPEEC 2009. Asia-Pacific*, 27-31 March 2009 2009, pp. 1-5, doi: 10.1109/APPEEC.2009.4918078.
- [38] A. Borghetti, M. Bosetti, M. Di Silvestro, C. A. Nucci, and M. Paolone, "Continuous-Wavelet Transform for Fault Location in Distribution Power Networks: Definition of Mother Wavelets Inferred From Fault Originated Transients," *Power Systems, IEEE Transactions on*, vol. 23, no. 2, pp. 380-388, 2008, doi: 10.1109/TPWRS.2008.919249.
- [39] A. Borghetti, M. Bosetti, C. A. Nucci, M. Paolone, and A. Abur, "Integrated Use of Time-Frequency Wavelet Decompositions for Fault Location in Distribution Networks: Theory and Experimental Validation," *Power Delivery, IEEE Transactions on*, vol. 25, no. 4, pp. 3139-3146, 2010, doi: 10.1109/TPWRD.2010.2046655.
- [40] Z. Q. Bo, G. Weller, and M. A. Redfern, "Accurate fault location technique for distribution system using fault-generated high-frequency transient voltage signals," *IEE Proceedings - Generation, Transmission and Distribution*, vol. 146, no. 1, pp. 73-79, 1999, doi: 10.1049/ip-gtd:19990074.
- [41] D. Thukaram, H. P. Khincha, and H. P. Vijaynarasimha, "Artificial neural network and support vector Machine approach for locating faults in radial

- distribution systems," *IEEE Transactions on Power Delivery*, vol. 20, no. 2, pp. 710-721, 2005, doi: 10.1109/TPWRD.2005.844307.
- [42] J. Coser, D. T. d. Vale, and J. G. Rolim, "Design and Training of Artificial Neural Networks for Locating Low Current Faults in Distribution Systems," in *2007 International Conference on Intelligent Systems Applications to Power Systems*, 5-8 Nov. 2007 2007, pp. 1-6, doi: 10.1109/ISAP.2007.4441599.
- [43] S. A. M. Javadian, A. M. Nasrabadi, M. Haghifam, and J. Rezvantalab, "Determining fault's type and accurate location in distribution systems with DG using MLP Neural networks," in *2009 International Conference on Clean Electrical Power*, 9-11 June 2009 2009, pp. 284-289, doi: 10.1109/ICCEP.2009.5212044.
- [44] F. Dehghani, F. Khodnia, and E. Dehghan, "Fault location of unbalanced power distribution feeder with distributed generation using neural networks," *CIREDA - Open Access Proceedings Journal*, vol. 2017, no. 1, pp. 1134-1137, 2017, doi: 10.1049/oap-cired.2017.0007.
- [45] M. Pourahmadi-Nakhli and A. A. Safavi, "Path Characteristic Frequency-Based Fault Locating in Radial Distribution Systems Using Wavelets and Neural Networks," *IEEE Transactions on Power Delivery*, vol. 26, no. 2, pp. 772-781, 2011, doi: 10.1109/TPWRD.2010.2050218.
- [46] S. Navaneethan, J. J. Soraghan, W. H. Siew, F. McPherson, and P. F. Gale, "Automatic fault location for underground low voltage distribution networks," *IEEE Transactions on Power Delivery*, vol. 16, no. 2, pp. 346-351, 2001, doi: 10.1109/61.915506.
- [47] M. M. Saha, *Fault Location on Power Networks / by Murari Mohan Saha, Jan Izykowski, Eugeniusz Rosolowski*. London: London : Springer London, 2010.

- [48] R. J. Hamidi and H. Livani, "Traveling-Wave-Based Fault-Location Algorithm for Hybrid Multiterminal Circuits," *IEEE Transactions on Power Delivery*, vol. 32, no. 1, pp. 135-144, 2017, doi: 10.1109/TPWRD.2016.2589265.
- [49] M. Korkali and A. Abur, "Fault location in meshed power networks using synchronized measurements," in *North American Power Symposium (NAPS), 2010*, 26-28 Sept. 2010 2010, pp. 1-6, doi: 10.1109/NAPS.2010.5618983.
- [50] M. Korkali, H. Lev-Ari, and A. Abur, "Traveling-Wave-Based Fault-Location Technique for Transmission Grids Via Wide-Area Synchronized Voltage Measurements," *IEEE Transactions on Power Systems*, vol. 27, no. 2, pp. 1003-1011, 2012, doi: 10.1109/TPWRS.2011.2176351.
- [51] K. Mert, "Robust and systemwide fault location in large-scale power networks via optimal deployment of synchronized measurements," 2013.
- [52] M. Salehi and F. Namdari, "Fault location on branched networks using mathematical morphology," *IET Generation, Transmission & Distribution*, vol. 12, no. 1, pp. 207-216, 2018, doi: 10.1049/iet-gtd.2017.0598.
- [53] A. Abur and F. H. Magnago, "Use of time delays between modal components in wavelet based fault location," *International Journal of Electrical Power and Energy Systems*, vol. 22, no. 6, pp. 397-403, 2000, doi: 10.1016/S0142-0615(00)00010-7.
- [54] A. Ghaderi, H. A. Mohammadpour, H. L. Ginn, and Y. J. Shin, "High-Impedance Fault Detection in the Distribution Network Using the Time-Frequency-Based Algorithm," *IEEE Transactions on Power Delivery*, vol. 30, no. 3, pp. 1260-1268, 2015, doi: 10.1109/TPWRD.2014.2361207.
- [55] J. Ding, L. Li, Y. Zheng, C. Zhao, H. Chen, and X. Wang, "Distributed travelling-wave-based fault location without time synchronisation and wave

velocity error," *IET Generation, Transmission & Distribution*, vol. 11, no. 8, pp. 2085-2093, 2017, doi: 10.1049/iet-gtd.2016.1778.

- [56] M. D. Borr, J. C. Bravo, J. C. Monta, and J. C. Monta, "Disturbance Ratio for Optimal Multi-Event Classification in Power Distribution Networks," *IEEE Transactions on Industrial Electronics*, vol. 63, no. 5, pp. 3117-3124, 2016, doi: 10.1109/TIE.2016.2521615.
  
- [57] G. International Conference on Large High Voltage Electric Systems. Study Committee 33. Working, *Guidelines for representation of networks: elements when calculating transients / Working Group 02 (Internal overvoltages) of Study Committee 33 (Overvoltages and Insulation Coordination)*. Paris: Paris : CIGRE, 1990.
  
- [58] A. Greenwood, *Electrical transients in power systems / Allan Greenwood*, 2nd ed.. ed. New York: New York : Wiley Interscience, 1991.
  
- [59] L. Al-Dabbagh, "DIGITAL SIMULATION OF FAULT LOCATION ALGORITHMS FOR EHV TRANSMISSION LINES," Doctor of Philosophy, Department of Electrical and Electronic Engineering, The Victoria University of Technology, Victoria, 1994.
  
- [60] *Guidelines for representation of networks: elements when calculating transients / Working Group 02 (Internal overvoltages) of Study Committee 33 (Overvoltages and Insulation Coordination)*. Paris: Paris : CIGRE, 1990.
  
- [61] A. Holdyk, B. Gustavsen, I. Arana, and J. Holboell, "Wideband Modeling of Power Transformers Using Commercial sFRA Equipment," *Power Delivery, IEEE Transactions on*, vol. 29, no. 3, pp. 1446-1453, 2014, doi: 10.1109/TPWRD.2014.2303174.

- [62] A. Morched, L. Marti, and J. Ottevangers, "A high frequency transformer model for the EMTP," *Power Delivery, IEEE Transactions on*, vol. 8, no. 3, pp. 1615-1626, 1993, doi: 10.1109/61.252688.
- [63] J. C. S. Silva, A. De Conti, D. G. Silveira, and J. L. Silvino, "Power transformer modeling based on wide band impedance and admittance measurements," in *Lightning Protection (XII SIPDA), 2013 International Symposium on*, 7-11 Oct. 2013 2013, pp. 291-296, doi: 10.1109/SIPDA.2013.6729224.
- [64] *FDBFIT device*. (2003). EMTP-EMTPWorks.
- [65] B. Gustavsen, "Computer code for rational approximation of frequency dependent admittance matrices," *IEEE Transactions on Power Delivery*, vol. 17, no. 4, pp. 1093-1098, 2002, doi: 10.1109/TPWRD.2002.803829.
- [66] B. Gustavsen, "Removing Insertion Impedance Effects From Transformer Admittance Measurements," *Power Delivery, IEEE Transactions on*, vol. 27, no. 2, pp. 1027-1029, 2012, doi: 10.1109/TPWRD.2011.2175818.
- [67] V. C. Nikolaidis, A. D. Patsidis, and A. M. Tsimtsios, "High impedance fault modelling and application of detection techniques with EMTP-RV," *The Journal of Engineering*, vol. 2018, no. 15, pp. 1120-1124, 2018, doi: 10.1049/joe.2018.0217.
- [68] J. A. Wischkaemper, C. L. Benner, B. Don Russell, and K. Muthu Manivannan, "Application of advanced electrical waveform monitoring and analytics for reduction of wildfire risk," in *Innovative Smart Grid Technologies Conference (ISGT), 2014 IEEE PES*, 19-22 Feb. 2014 2014, pp. 1-5, doi: 10.1109/ISGT.2014.6816487.
- [69] N. Bahador, F. Namdari, and H. R. Matinfar, "Modelling and detection of live tree-related high impedance fault in distribution systems," *IET Generation*,

*Transmission & Distribution*, vol. 12, no. 3, pp. 756-766, 2018, doi: 10.1049/iet-gtd.2017.0211.

- [70] A. E. Emanuel, D. Cyganski, J. A. Orr, S. Shiller, and E. M. Gulachenski, "High impedance fault arcing on sandy soil in 15 kV distribution feeders: contributions to the evaluation of the low frequency spectrum," *Power Delivery, IEEE Transactions on*, vol. 5, no. 2, pp. 676-686, 1990, doi: 10.1109/61.53070.
- [71] A. V. Masa, "High Impedance Fault Detection Method in Multi-Grounded Distribution Networks," 2013.
- [72] W. Santos, B. Souza, N. Brito, F. Costa, and M. Paes, "High Impedance Faults: From Field Tests to Modeling," *formerly CONTROLE & AUTOMAÇÃO*, vol. 24, no. 6, pp. 885-896, 2013, doi: 10.1007/s40313-013-0072-8.
- [73] C. Tao, D. Xinzhou, B. Zhiqian, A. Klimek, and A. Edwards, "Modeling study for high impedance fault detection in MV distribution system," in *Universities Power Engineering Conference, 2008. UPEC 2008. 43rd International*, 1-4 Sept. 2008 2008, pp. 1-5, doi: 10.1109/UPEC.2008.4651507.
- [74] V. Torres, J. L. Guardado, H. F. Ruiz, and S. Maximov, "Modeling and detection of high impedance faults," *International Journal of Electrical Power & Energy Systems*, vol. 61, no. 0, pp. 163-172, 10// 2014, doi: <http://dx.doi.org/10.1016/j.ijepes.2014.03.046>.
- [75] A. M. Sharat, L. A. Snider, and K. Debnath, "A neural network based back error propagation relay algorithm for distribution system high impedance fault detection," in *1993 2nd International Conference on Advances in Power System Control, Operation and Management, APSCOM-93.*, 7-10 Dec. 1993 1993, pp. 613-620 vol.2.

- [76] A. R. Sedighi and M. R. Haghifam, "Simulation of high impedance ground fault In electrical power distribution systems," in *Power System Technology (POWERCON), 2010 International Conference on*, 24-28 Oct. 2010 2010, pp. 1-7, doi: 10.1109/POWERCON.2010.5666061.
- [77] W. David Chan Tat and Y. Xia, "A novel technique for high impedance fault identification," *Power Delivery, IEEE Transactions on*, vol. 13, no. 3, pp. 738-744, 1998, doi: 10.1109/61.686968.
- [78] N. Zamanan and J. Sykulski, "The evolution of high impedance fault modeling," in *2014 16th International Conference on Harmonics and Quality of Power (ICHQP)*, 25-28 May 2014 2014, pp. 77-81, doi: 10.1109/ICHQP.2014.6842852.
- [79] M. Kizilcay and T. Pniok, "Digital simulation of fault arcs in power systems," *European Transactions on Electrical Power*, vol. 1, no. 1, pp. 55-60, 1991, doi: 10.1002/etep.4450010111.
- [80] M. Michalik, W. Rebizant, M. Lukowicz, L. Seung-Jae, and K. Sang-Hee, "Wavelet transform approach to high impedance fault detection in MV networks," in *2005 IEEE Russia Power Tech*, 27-30 June 2005 2005, pp. 1-7, doi: 10.1109/PTC.2005.4524815.
- [81] N. Elkalashy, M. Lehtonen, H. Darwish, M. Izzularab, and A.-m. Taalab, "Modeling and experimental verification of high impedance arcing fault in medium voltage networks," *IEEE Transactions on Dielectrics and Electrical Insulation*, vol. 14, no. 2, pp. 375-383, 2007, doi: 10.1109/tdei.2007.344617.
- [82] S. Bindu *et al.*, "Modelling of a spark gap switch," in *2012 IEEE 10th International Conference on the Properties and Applications of Dielectric Materials*, 24-28 July 2012 2012, pp. 1-4, doi: 10.1109/ICPADM.2012.6318933.

- [83] J. Ryu, "Electromagnetic Transient Simulation of Spark-Gap Switched Pulse Generators for Predicting Pulse Waveforms," *IEEE Transactions on Plasma Science*, vol. 42, no. 9, pp. 2193-2197, 2014, doi: 10.1109/TPS.2014.2341743.
- [84] F. E. Nathanson, *Radar Design Principles: Signal Processing and the Environment*. McGraw-Hill Book Co., 1969.
- [85] M. Ando, E. O. Schweitzer, and R. A. Baker, "Development and Field-Data Evaluation of Single-End Fault Locator for Two-Terminal HVDC Transmission Lines-Part 2 : Algorithm and Evaluation," *IEEE Transactions on Power Apparatus and Systems*, vol. PAS-104, no. 12, pp. 3531-3537, 1985, doi: 10.1109/TPAS.1985.318906.
- [86] R. L. a. Allen, *Signal analysis : time, frequency, scale, and structure / Ronald L. Allen, Duncan W. Mills*. Piscataway, New Jersey : IEEE Press [Piscataway, New Jersey] : IEEE Xplore, 2004.
- [87] K. Chul Hwan and A. Raj, "Wavelet transforms in power systems. I. General introduction to the wavelet transforms," *Power Engineering Journal*, vol. 14, no. 2, pp. 81-87, 2000, doi: 10.1049/pe:20000210.
- [88] P. Imriš, "TRANSIENT BASED EARTH FAULT LOCATION IN 110 KV SUBTRANSMISSION NETWORKS," Doctoral, Department of Electrical and Communications Engineering, Helsinki University of Technology, 2008.
- [89] Y. J. Shin, "Theory and Application of Time-Frequency Analysis to Transient Phenomena in Electric Power and Other Physical Systems," DOCTOR OF PHILOSOPHY, The University of Texas at Austin, 2004.
- [90] I. Daubechies, *Ten lectures on wavelets / Ingrid Daubechies* (10 lectures on wavelets). Philadelphia, Pa.: Philadelphia, Pa. : Society for Industrial and Applied Mathematics (SIAM, 3600 Market Street, Floor 6, Philadelphia, PA 19104), 1992.



- [91] S. G. Mallat, "A theory for multiresolution signal decomposition: the wavelet representation," *IEEE Transactions on Pattern Analysis and Machine Intelligence*, vol. 11, no. 7, pp. 674-693, 1989, doi: 10.1109/34.192463.
- [92] D. C. Robertson, O. I. Camps, J. S. Mayer, and W. B. Gish, "Wavelets and electromagnetic power system transients," *IEEE Transactions on Power Delivery*, vol. 11, no. 2, pp. 1050-1058, 1996, doi: 10.1109/61.489367.
- [93] O. Rioul and M. Vetterli, "Wavelets and signal processing," *IEEE Signal Processing Magazine*, vol. 8, no. 4, pp. 14-38, 1991, doi: 10.1109/79.91217.
- [94] F. B. Costa, "Fault-Induced Transient Detection Based on Real-Time Analysis of the Wavelet Coefficient Energy," *IEEE Transactions on Power Delivery*, vol. 29, no. 1, pp. 140-153, 2014, doi: 10.1109/TPWRD.2013.2278272.
- [95] D. B. Percival, *Wavelet methods for time series analysis / Donald B. Percival and Andrew T. Walden*. Cambridge: Cambridge : Cambridge University Press, 2000.
- [96] F. B. Costa and J. Driesen, "Assessment of Voltage Sag Indices Based on Scaling and Wavelet Coefficient Energy Analysis," *IEEE Transactions on Power Delivery*, vol. 28, no. 1, pp. 336-346, 2013, doi: 10.1109/TPWRD.2012.2218626.
- [97] F. B. Costa, B. A. Souza, N. S. D. Brito, J. A. C. B. Silva, and W. C. Santos, "Real-Time Detection of Transients Induced by High-Impedance Faults Based on the Boundary Wavelet Transform," *IEEE Transactions on Industry Applications*, vol. 51, no. 6, pp. 5312-5323, 2015, doi: 10.1109/TIA.2015.2434993.
- [98] F. B. Costa, "Boundary Wavelet Coefficients for Real-Time Detection of Transients Induced by Faults and Power-Quality Disturbances," *IEEE*

*Transactions on Power Delivery*, vol. 29, no. 6, pp. 2674-2687, 2014, doi: 10.1109/TPWRD.2014.2321178.

- [99] F. H. Magnago and A. Abur, "Fault location using wavelets," *IEEE Transactions on Power Delivery*, vol. 13, no. 4, pp. 1475-1480, 1998, doi: 10.1109/61.714808.
- [100] R. H. Park, "Two-reaction theory of synchronous machines generalized method of analysis-part I," *Transactions of the American Institute of Electrical Engineers*, vol. 48, no. 3, pp. 716-727, 1929, doi: 10.1109/T-AIEE.1929.5055275.
- [101] D. F. J. F. V. Lopes, W. L. A. Neves, "Fault Location on Transmission Lines Based on Travelling Waves," presented at the International Conference on Power Systems Transients, Delft, The Netherlands, 2011.
- [102] F. V. Lopes, D. Fernandes, and W. L. A. Neves, "Transients detection in EHV transmission lines using park's transformation," in *PES T&D 2012*, 7-10 May 2012 2012, pp. 1-6, doi: 10.1109/TDC.2012.6281528.
- [103] F. V. Lopes, D. Fernandes, and W. L. A. Neves, "A Traveling-Wave Detection Method Based on Park's Transformation for Fault Locators," *Power Delivery, IEEE Transactions on*, vol. 28, no. 3, pp. 1626-1634, 2013, doi: 10.1109/TPWRD.2013.2260182.
- [104] X. Ma, C. Zhou, and I. J. Kemp, "Automated wavelet selection and thresholding for PD detection," *IEEE Electrical Insulation Magazine*, vol. 18, no. 2, pp. 37-45, 2002, doi: 10.1109/57.995398.
- [105] H. Zhengyou, F. Ling, L. Sheng, and B. Zhiqian, "Fault Detection and Classification in EHV Transmission Line Based on Wavelet Singular Entropy," *Power Delivery, IEEE Transactions on*, vol. 25, no. 4, pp. 2156-2163, 2010, doi: 10.1109/TPWRD.2010.2042624.

- [106] A. A. Yusuff, A. A. Jimoh, and J. L. Munda, "Determinant-based feature extraction for fault detection and classification for power transmission lines," *Generation, Transmission & Distribution, IET*, vol. 5, no. 12, pp. 1259-1267, 2011, doi: 10.1049/iet-gtd.2011.0110.
- [107] L. Weilin, A. Monti, and F. Ponci, "Fault Detection and Classification in Medium Voltage DC Shipboard Power Systems With Wavelets and Artificial Neural Networks," *Instrumentation and Measurement, IEEE Transactions on*, vol. 63, no. 11, pp. 2651-2665, 2014, doi: 10.1109/TIM.2014.2313035.
- [108] S. P. Valsan and K. S. Swarup, "High-Speed Fault Classification in Power Lines: Theory and FPGA-Based Implementation," *Industrial Electronics, IEEE Transactions on*, vol. 56, no. 5, pp. 1793-1800, 2009, doi: 10.1109/TIE.2008.2011055.
- [109] S. M. Torabi, "Fault location and classification in distribution systems using clark transformation and neural network," in *Electrical Power Distribution Networks (EPDC), 2011 16th Conference on*, 19-20 April 2011 2011, pp. 1-8.
- [110] B. Tacer and P. J. Loughlin, "NON-STATIONARY SIGNAL CLASSIFICATION USING THE JOINT MOMENTS OF TIME-FREQUENCY DISTRIBUTIONS," *Pattern Recognition*, vol. 31, no. 11, pp. 1635-1641, 1998, doi: 10.1016/S0031-3203(98)00031-4.
- [111] M. M. Mansour and G. W. Swift, "A Multi-Microprocessor Based Travelling Wave Relay - Theory and Realization," *Power Delivery, IEEE Transactions on*, vol. 1, no. 1, pp. 272-279, 1986, doi: 10.1109/TPWRD.1986.4307919.
- [112] M. M. Mansour and G. W. Swift, "Design and Testing of a Multi-Microprocessor Travelling Wave Relay," *Power Delivery, IEEE Transactions on*, vol. 1, no. 4, pp. 74-82, 1986, doi: 10.1109/TPWRD.1986.4308032.

- [113] J. Joe-Air, C. Ching-Shan, and L. Chih-Wen, "A new protection scheme for fault detection, direction discrimination, classification, and location in transmission lines," *Power Delivery, IEEE Transactions on*, vol. 18, no. 1, pp. 34-42, 2003, doi: 10.1109/TPWRD.2002.803726.
- [114] D. P. Coggins, D. W. P. Thomas, B. R. Hayes-Gill, Y. Zhu, E. T. Pereira, and S. H. L. Cabral, "A New High Speed FPGA based Travelling Wave Fault Recorder for MV Distribution Systems," in *Developments in Power System Protection, 2008. DPSP 2008. IET 9th International Conference on*, 17-20 March 2008 2008, pp. 579-583.
- [115] A. T. Jahromi, P. Wolfs, and S. Islam, "A travelling wave detector based fault location device and data recorder for medium voltage distribution systems," in *2016 Australasian Universities Power Engineering Conference (AUPEC)*, 25-28 Sept. 2016 2016, pp. 1-5, doi: 10.1109/AUPEC.2016.7749307.
- [116] W. K. V. Chan, Ed. *Theory and Applications of Monte Carlo Simulations*. Rensselaer Polytechnic Institute, United States of America: InTechOpen, 2013.
- [117] X. Su, M. A. S. Masoum, and P. J. Wolfs, "PSO and Improved BSFS Based Sequential Comprehensive Placement and Real-Time Multi-Objective Control of Delta-Connected Switched Capacitors in Unbalanced Radial MV Distribution Networks," *IEEE Transactions on Power Systems*, vol. 31, no. 1, pp. 612-622, 2016, doi: 10.1109/TPWRS.2015.2398361.
- [118] N. Jin and Y. Rahmat-Samii, "Advances in Particle Swarm Optimization for Antenna Designs: Real-Number, Binary, Single-Objective and Multiobjective Implementations," *IEEE Transactions on Antennas and Propagation*, vol. 55, no. 3, pp. 556-567, 2007, doi: 10.1109/TAP.2007.891552.
- [119] A. Homaifar, C. X. Qi, and S. H. Lai, "Constrained Optimization Via Genetic Algorithms," vol. 62, ed, 1994, pp. 242-253.

- [120] M. A. A. Pedrasa, T. D. Spooner, and I. F. MacGill, "Scheduling of Demand Side Resources Using Binary Particle Swarm Optimization," *IEEE Transactions on Power Systems*, vol. 24, no. 3, pp. 1173-1181, 2009, doi: 10.1109/TPWRS.2009.2021219.
- [121] A. T. Jahromi, P. Wolfs, and S. Islam, "Travelling wave fault location in rural radial distribution networks to reduce wild fire risk," in *Power Engineering Conference (AUPEC), 2015 Australasian Universities, 27-30 Sept. 2015*, pp. 1-6, doi: 10.1109/AUPEC.2015.7324833.

## Appendix A

### Frequency-dependent branch device

The EMTP frequency-dependent device model consisted of several parallel RLC branches (see Figure 4.7). The model data file required by this device can be automatically produced using FDBFIT transient analysis of control system tools. The first two data lines are given the number of phases and where the model is balanced. A 1 indicates a balance network, and 0 indicates an unbalanced case. The third line indicates the number of RLC branches. The fourth line indicates the number of branches. The branch information providers are in the following order for one branch:

- $R_n$ , which is expressed in ohms
- $L_n$ , which is expressed in henries
- $R_{Ln}$ , which is expressed in ohms
- $C_n$ , which is expressed in farads
- $R_{Cn}$ , which is expressed in ohms.

The next branches field data are provided in the same pattern after each other. The branch information data for the tested transformer is provided below.

```

C Approximation of branch [1, 1], Fitting by elements
C BUS = H , ,
n_phase = 1
balanced = 1
25
0.3209606839139275E+04 -.6453870206631106E-01 0.0000000000000000E+00
-.1966581275455072E-09 -.1783475732485064E+05
0.5329474458707018E+03 0.1550438613839554E-02 0.0000000000000000E+00
0.2869430732694902E-09 0.4284523463613366E+04
-.1679876735842136E+04 0.1963773911600615E-02 0.0000000000000000E+00
0.2740485322508067E-10 0.2438617026849027E+05
-.1368174719984919E+04 -.1385754215730403E-02 0.0000000000000000E+00
-.4146703415868084E-09 -.7727219757465845E+04
0.4497765259733760E+04 -.2410959560991299E-02 0.0000000000000000E+00
-.1200295479905846E-10 -.2848093016985224E+05
0.1378465188566943E+03 0.0000000000000000E+00 0.0000000000000000E+00
0.6252352995081614E-09 0.0000000000000000E+00
0.2317897246181579E+07 0.7356709780082275E+02 0.0000000000000000E+00
0.1364720259027823E-10 -.2398592326150046E+07
0.6044515484913929E+06 0.2658848309907542E+02 0.0000000000000000E+00
0.7649426650211961E-10 -.6969825618161598E+06
0.2265616337976047E+04 -.1441358593652282E+01 0.0000000000000000E+00
-.3171732001840494E-08 -.1637691369638392E+05
-.8013110056635489E+05 -.4464188094608683E+01 0.0000000000000000E+00
-.4617371655819059E-09 0.4590230903723467E+06
-.8135251963355365E+05 -.2653974786490144E+01 0.0000000000000000E+00
-.3140978388178981E-09 0.1072940150998634E+07
-.1943764269987858E+06 -.3052506948682961E+01 0.0000000000000000E+00
-.6532606095520163E-10 0.6312493383846653E+06
-.6729696560311932E+05 0.2312049572490858E+01 0.0000000000000000E+00
0.8146149041049054E-10 0.2351930848088395E+06
0.5159269230786242E+07 0.1264409042533593E+02 0.0000000000000000E+00
0.4889699494806371E-12 -.5297136592965811E+07
0.4820109288689431E+06 0.4140400095800436E+01 0.0000000000000000E+00
0.1451493479080720E-10 -.7370480854788909E+06
-.1907628553173176E+04 -.1390546193645342E+00 0.0000000000000000E+00
-.9550408612596730E-09 -.2506648035837357E+05
-.3735919201300962E+04 0.9585251403263863E-01 0.0000000000000000E+00
0.7096815681744514E-09 0.1328603311670243E+05
0.3035546664353530E+06 0.5017147080647198E+00 0.0000000000000000E+00
0.5901134395747267E-11 -.3189890468948129E+06
-.6042683568540615E+04 -.7797545105930730E-02 0.0000000000000000E+00
-.8000153053767010E-09 -.3761129625613109E+05
-.1361666645159421E+05 0.7814684576149057E-01 0.0000000000000000E+00
0.7945270575987824E-10 0.4514582164098774E+05
-.4307877809155781E+05 -.1666771487624169E-01 0.0000000000000000E+00
-.7440361647242073E-11 0.6059098037300668E+05
0.2697494944662187E+05 -.5217014864879490E-02 0.0000000000000000E+00
-.4548236135782829E-11 -.3666106870525942E+05
-.1284408083948585E+04 -.8232413930192234E-03 0.0000000000000000E+00
-.6441784854485286E-10 0.2628819057984036E+05
0.1175229576278473E+04 0.6398817658351176E-03 0.0000000000000000E+00
0.3182285218253662E-10 -.2732760438920651E+05
0.2893897671797425E+02 0.0000000000000000E+00
0.0000000000000000E+00
0.5520609757927596E-10 0.0000000000000000E+00

```

```

C Approximation of branch [1, 2], Fitting by elements
C BUS = H , a1 ,
n_phase = 1
balanced = 1
19
-.2317897246181579E+07 -.7356709780082275E+02 0.0000000000000000E+00
-.1364720259027823E-10 0.2398592326150046E+07
-.6044515484913929E+06 -.2658848309907542E+02 0.0000000000000000E+00
-.7649426650211961E-10 0.6969825618161598E+06
-.2265616337976047E+04 0.1441358593652282E+01 0.0000000000000000E+00
0.3171732001840494E-08 0.1637691369638392E+05
0.8013110056635489E+05 0.4464188094608683E+01 0.0000000000000000E+00
0.4617371655819059E-09 -.4590230903723467E+06
0.8135251963355365E+05 0.2653974786490144E+01 0.0000000000000000E+00
0.3140978388178981E-09 -.1072940150998634E+07
0.1943764269987858E+06 0.3052506948682961E+01 0.0000000000000000E+00
0.6532606095520163E-10 -.6312493383846653E+06
0.6729696560311932E+05 -.2312049572490858E+01 0.0000000000000000E+00
-.8146149041049054E-10 -.2351930848088395E+06
-.5159269230786242E+07 -.1264409042533593E+02 0.0000000000000000E+00
-.4889699494806371E-12 0.5297136592965811E+07
-.4820109288689431E+06 -.4140400095800436E+01 0.0000000000000000E+00
-.1451493479080720E-10 0.7370480854788909E+06
0.1907628553173176E+04 0.1390546193645342E+00 0.0000000000000000E+00
0.9550408612596730E-09 0.2506648035837357E+05
0.3735919201300962E+04 -.9585251403263863E-01 0.0000000000000000E+00
-.7096815681744514E-09 -.1328603311670243E+05
-.3035546664353530E+06 -.5017147080647198E+00 0.0000000000000000E+00
-.5901134395747267E-11 0.3189890468948129E+06
0.6042683568540615E+04 0.7797545105930730E-02 0.0000000000000000E+00
0.8000153053767010E-09 0.3761129625613109E+05
0.1361666645159421E+05 -.7814684576149057E-01 0.0000000000000000E+00
-.7945270575987824E-10 -.4514582164098774E+05
0.4307877809155781E+05 0.1666771487624169E-01 0.0000000000000000E+00
0.7440361647242073E-11 -.6059098037300668E+05
-.2697494944662187E+05 0.5217014864879490E-02 0.0000000000000000E+00
0.4548236135782829E-11 0.3666106870525942E+05
0.1284408083948585E+04 0.8232413930192234E-03 0.0000000000000000E+00
0.6441784854485286E-10 -.2628819057984036E+05
-.1175229576278473E+04 -.6398817658351176E-03 0.0000000000000000E+00
-.3182285218253662E-10 0.2732760438920651E+05
-.2893897671797425E+02 0.0000000000000000E+00 0.0000000000000000E+00
-.5520609757927596E-10 0.0000000000000000E+00

```

```

C Approximation of branch [2, 2], Fitting by elements
C BUS = a1 , ,
n_phase = 1
balanced = 1
37
0.2317897246181579E+07 0.7356709780082275E+02 0.0000000000000000E+00
0.1364720259027823E-10 -.2398592326150046E+07
0.6044515484913929E+06 0.2658848309907542E+02 0.0000000000000000E+00
0.7649426650211961E-10 -.6969825618161598E+06
0.2265616337976047E+04 -.1441358593652282E+01 0.0000000000000000E+00
-.3171732001840494E-08 -.1637691369638392E+05
-.8013110056635489E+05 -.4464188094608683E+01 0.0000000000000000E+00
-.4617371655819059E-09 0.4590230903723467E+06
-.8135251963355365E+05 -.2653974786490144E+01 0.0000000000000000E+00
-.3140978388178981E-09 0.1072940150998634E+07
-.1943764269987858E+06 -.3052506948682961E+01 0.0000000000000000E+00

```



-.6532606095520163E-10 0.6312493383846653E+06  
-.6729696560311932E+05 0.2312049572490858E+01 0.0000000000000000E+00  
0.8146149041049054E-10 0.2351930848088395E+06  
0.5159269230786242E+07 0.1264409042533593E+02 0.0000000000000000E+00  
0.4889699494806371E-12 -.5297136592965811E+07  
0.4820109288689431E+06 0.4140400095800436E+01 0.0000000000000000E+00  
0.1451493479080720E-10 -.7370480854788909E+06  
-.1907628553173176E+04 -.1390546193645342E+00 0.0000000000000000E+00  
-.9550408612596730E-09 -.2506648035837357E+05  
-.3735919201300962E+04 0.9585251403263863E-01 0.0000000000000000E+00  
0.7096815681744514E-09 0.1328603311670243E+05  
0.3035546664353530E+06 0.5017147080647198E+00 0.0000000000000000E+00  
0.5901134395747267E-11 -.3189890468948129E+06  
-.6042683568540615E+04 -.7797545105930730E-02 0.0000000000000000E+00  
-.8000153053767010E-09 -.3761129625613109E+05  
-.1361666645159421E+05 0.7814684576149057E-01 0.0000000000000000E+00  
0.7945270575987824E-10 0.4514582164098774E+05  
-.4307877809155781E+05 -.1666771487624169E-01 0.0000000000000000E+00  
-.7440361647242073E-11 0.6059098037300668E+05  
0.2697494944662187E+05 -.5217014864879490E-02 0.0000000000000000E+00  
-.4548236135782829E-11 -.3666106870525942E+05  
-.1284408083948585E+04 -.8232413930192234E-03 0.0000000000000000E+00  
-.6441784854485286E-10 0.2628819057984036E+05  
0.1175229576278473E+04 0.6398817658351176E-03 0.0000000000000000E+00  
0.3182285218253662E-10 -.2732760438920651E+05  
0.2893897671797425E+02 0.0000000000000000E+00 0.0000000000000000E+00  
0.5520609757927596E-10 0.0000000000000000E+00  
0.1873741364617455E+07 0.5458858151534740E+02 0.0000000000000000E+00  
0.1532138379180391E-10 -.1945792874163939E+07  
0.4862788283575633E+06 -.2874558700956259E+02 0.0000000000000000E+00  
-.9950036653664925E-10 -.5705224870869642E+06  
0.5352326039218766E+06 -.2858770940150572E+02 0.0000000000000000E+00  
-.8279062297975407E-10 -.6230759704291533E+06  
0.2212009014216760E+06 -.1980538476991013E+02 0.0000000000000000E+00  
-.2540586026102404E-09 -.3331289680874100E+06  
-.1427161869050596E+05 -.4746531045766049E+01 0.0000000000000000E+00  
-.2688567666542163E-08 0.2181204445062139E+06  
0.6368222550716425E+05 0.3373793114337661E+01 0.0000000000000000E+00  
0.6905050931903639E-09 -.9308168976172614E+05  
0.3786506142872734E+04 0.6006277256519558E+00 0.0000000000000000E+00  
0.7533688210844913E-08 -.7822052654761207E+05  
0.8486048764396086E+05 0.7777957113172380E+00 0.0000000000000000E+00  
0.1138117826150419E-09 -.8699492439980771E+05  
-.5880596435633763E+01 -.1707880534500026E-02 0.0000000000000000E+00  
-.1143761777523229E-05 -.4618623946257685E+02  
-.1683432399463635E+04 0.1657435772311645E-01 0.0000000000000000E+00  
0.4699600278045372E-08 0.1770516683790213E+04  
-.1371967472828184E+02 0.3169550528857303E-02 0.0000000000000000E+00  
0.3232759838992700E-06 0.1048894662927001E+03  
0.2308181351882688E+00 0.2174042721141041E-04 0.0000000000000000E+00  
0.1847184568090130E-04 0.5861939848841422E+00  
0.4619446601874878E+01 -.5482807644700115E-04 0.0000000000000000E+00  
-.9058514832892737E-06 -.5740474897490252E+01  
-.2457626356467877E+01 -.4184206197129416E-04 0.0000000000000000E+00  
-.1211418667626343E-04 -.7194830877237033E+00  
0.1220488725014893E+04 0.8724616251849725E-03 0.0000000000000000E+00  
0.9426168705532510E-09 -.1318174003177692E+04  
0.4236509764593691E+02 0.2112811061286092E-04 0.0000000000000000E+00  
0.1698103090098121E-06 0.6165164399216010E+01  
-.5495556915790598E+02 -.1929652763088994E-04 0.0000000000000000E+00  
-.1466197427012706E-08 -.4627660362216204E+02

0.1207170803982248E+03	0.0000000000000000E+00
0.0000000000000000E+00	
0.1359321388708347E-07	0.0000000000000000E+00

# Appendix B

## List of Publications

The following list includes all the papers published by the author during his research studies. Papers are directly linked with research presented in this thesis.

### **Journal Paper**

[J1] A. Tashakkori, P. J. Wolfs, S. Islam and A. Abu-Siada, "Fault Location on Radial Distribution Networks via Distributed Synchronized Traveling Wave Detectors," in IEEE Transactions on Power Delivery, vol. 35, no. 3, pp. 1553-1562, June 2020, doi: 10.1109/TPWRD.2019.2948174.

### **Journal Paper – Submitted for approval**

[J2] A. Tashakkori, P. J. Wolfs, S. Islam and A. Abu-Siada, " Optimal Placement of Synchronized Voltage Travelling Wave Sensors in a Radial Distribution Network", submitted to IEEE Access on December 2020.

### **Conference Papers**

[C1] A. T. Jahromi, P. Wolfs and S. Islam, "Travelling wave fault location in rural radial distribution networks to reduce wild fire risk," 2015 Australasian Universities Power Engineering Conference (AUPEC), Wollongong, NSW, 2015, pp. 1-6, doi: 10.1109/AUPEC.2015.7324833.

[C2] A. T. Jahromi, P. Wolfs and S. Islam, "A travelling wave detector based fault location device and data recorder for medium voltage distribution systems," 2016 Australasian Universities Power Engineering Conference (AUPEC), Brisbane, QLD, 2016, pp. 1-5, doi: 10.1109/AUPEC.2016.7749307.

